DISTRIBUTED CONTROL OF MULTI-AGENT SYSTEMS: PERFORMANCE SCALING WITH NETWORK SIZE

By

HE HAO

A DISSERTATION PRESENTED TO THE GRADUATE SCHOOL
OF THE UNIVERSITY OF FLORIDA IN PARTIAL FULFILLMENT
OF THE REQUIREMENTS FOR THE DEGREE OF
DOCTOR OF PHILOSOPHY

UNIVERSITY OF FLORIDA

2012

To my mother and my wife

ACKNOWLEDGMENTS

I would like to express my sincere gratitude to my advisor Dr. Prabir Barooah for leading me through this effort. Without his guidance, encouragement and support, this dissertation would have not been possible. I am very grateful for his supervision, advice, and guidance from the initial stage of this research to the final completion of this work. From him, not only did I learn how to be a rigorous and self-motivated researcher, but also how to develop collaborative relationships with other scientists. He provided me unflinching encouragement and support in various ways and I am indebted to him more than he knows. I feel very fortunate to have had the opportunity to work with him and I would like to thank him for all the knowledge he has imparted to me.

I also want to extend my special gratitude to Dr. Prashant G. Mehta, who is always supportive and helpful to me. I am grateful for his constructive advice and inspiring discussions as well as his crucial contributions to my research. I am indebted to him for providing me the opportunity to work with him for two summers at UIUC. His insightfullness and spirit of adventure in research have triggered and nourished my intellectual development.

It is a pleasure to thank Professors Pramod Khargonekar, Warren Dixon and Richard Lind for being in my committee and using their precious times to read this dissertation and gave constructive comments to improve the quality and presentation of this work.

I also offer my regards and gratitude to all of those who supported me in any respect during the completion of the work.

Last but not the least, I would like to thank two of the most important women in my life: my mother and my wife. I am heartily thankful for their love, care, support and encouragement. Without them, my life would have been much less meaningful.

TABLE OF CONTENTS

LIST OF FIGURES

Abstract of Dissertation Presented to the Graduate School
of the University of Florida in Partial Fulfillment of the
Requirements for the Degree of Doctor of Philosophy

DISTRIBUTED CONTROL OF MULTI-AGENT SYSTEMS: PERFORMANCE SCALING WITH NETWORK SIZE

By

He Hao

December 2012

Chair: Prabir Barooah
Major: Mechanical Engineering

The goal of distributed control of multi-agent systems (MASs) is to achieve a global control objective while using only locally available information. Each agent computes its own control action by using only information that can be obtained by either communication with its nearby neighbors or by on-board sensors. Recent years have witnessed a burgeoning interest in MASs due to their wide range of applications, such as automated highway system, surveillance and rescue by coordination of aerial and ground vehicles, spacecraft formation control for science missions. Most of these applications involve a large number of agents that are distributed over a broad geographical domain, in which a centralized control solution that requires all-to-all or all-to-one communication is impractical due to overwhelming communication demands. This motivates study of distributed control architectures, in which each agent makes control decisions based on only locally available information. Although it is more appealing than centralized control in this regard, distributed control suffers from a few limitations. In particular, its performance usually degrades as the number of agents in the collection increases.

In this work, we examine two classes of distributed control problems: vehicular formation control and distributed consensus. Despite difference in their agent dynamics, the two problems are similar. In the vehicular formation control problem, each agent is modeled as a double-integrator. In contrast, the dynamics of each agent in distributed consensus is usually given by a single-integrator or its discrete counterpart. The goal of

formation control is to make the vehicle team track a desired trajectory while keeping a rigid formation geometry, while the control objective of distributed consensus is to make all the agents' states converge to a common value. We study the scaling laws of certain performance metrics as a function of the number of agents in the system. We show that the performances for both vehicular formation and distributed consensus degrade when the number of agents in the system increases for symmetric control. Here symmetric control refers to, between each pair of neighboring agents (i, j), the weight agent i put on the information received from j is the same as the weight agent j put on the information received from i. Besides analysis, we also study how to design distributed control algorithms to improve performance scaling.

For the vehicular formation control problem, we describe a novel methodology for modelling, analysis and distributed control design. The method relies on a partial differential equation (PDE) approximation that describes the spatio-temporal evolution of each vehicle's position tracking error. The analysis and control design is based on this PDE model. We deduce scaling laws of the closed-loop stability margin (absolute value of the real part of the least stable eigenvalue) and robustness to external disturbances (certain H_∞ norm of the system) of the controlled formation as a function of the number of vehicles in the formation. We show that the exponents in the scaling laws for both the stability margin and robustness to external disturbances are influenced by the dimension and the structure of the information graph, which describes the information exchange among neighboring vehicles. Moreover, the scaling laws can be improved by employing a higher dimensional information graph and/or using a beneficial aspect ratio for the information graph.

Apart from analysis, the PDE model is used for an *asymmetric* design of control gains to improve the stability margin and robustness to external disturbances. Asymmetric design means the information received from different neighbors are weighted prejudicially, instead of equally in symmetric design. We show that with asymmetric design, the system

has a significantly better stability margin and robustness even with a small amount of asymmetry in the control gains. The results of the analysis with the PDE model are corroborated with numerical computation with the state-space model of the formation.

Besides distributed control of vehicular formations, the progressive loss of performance has also been observed in distributed consensus, which has a wide range of applications such as distributed computing, sensor fusion and vehicle rendezvous. In distributed consensus, each agent in a network updates its state by using a weighted summation of its own state and the states of its neighbors. Prior works showed that with symmetric weights, the consensus rate became progressively smaller when the number of agents in the network increased, even when the weights were chosen to maximize the consensus rate. We show that with proper choice of *asymmetric* weights which are motivated by asymmetric control design for vehicular formations, the consensus rate can be improved significantly over symmetric design. In particular, we prove that the consensus rate in a lattice graph can be made independent of the size of the graph with asymmetric weights. We also propose a weight design method for more general graphs than lattices. Numerical computations show that the resulting consensus rate with asymmetric weight design is improved considerably over that with symmetric optimal weights.

CHAPTER 1
INTRODUCTION

1.1 Motivation and Problem Statement

Distributed control has spurred a great interest in the control community due to its broad applications such as cooperative control of vehicular formations [1–5], synchronization of power networks and coupled oscillators [6–8], distributed consensus of networked systems [9–11], study of collective behavior of bird flocks and animal swarms [12–14], and formation flying of unmanned aerial and ground vehicles for surveillance, reconnaissance and rescue [15–19]. Most of these applications are large-scale networked multi-agent systems that are distributed over large geographical domains. A centralized control solution that requires all-to-all or all-to-one communication is impractical due to overwhelming communication demands. This motivates investigation of distributed control architectures where an individual agent exchanges information only with a small set of agents (neighbors) to make control decisions. The goal of distributed control is to achieve a global objective by using only locally available information.

In a multi-agent system, the interaction between neighboring agents is often described by an information graph. It is well known that the graph Laplacian and its spectral properties play an important role in studying the performance of the system [3, 10, 20–22]. Therefore, to achieve good closed-loop performance, the key is to design the control gains to optimize certain eigenvalues of the graph Laplacian. The optimization of graph eigenvalues has always been a topic of interest in engineering and science [23–27]. However, most works assume that the information graph is undirected, which means the information exchange between neighboring agents are symmetric, i.e. between two agents i and j that exchange information, the weight placed by i on the information received from j is the same as the weight placed by j on that received from i. The symmetry assumption facilitates analysis and design. In particular, it makes the problem of optimization of graph Laplacian eigenvalues convex. Several distributed control design method have been

proposed by taking advantage of the convexity property [23, 28–30]. However, a typical issue in distributed control of large-scale MASs is that the performance of the closed-loop with symmetric information graph degrades as the number of agents increases. Several recent papers have studied the scaling of performance as a function of the number of agents [3, 31–37].

In this work, we break the symmetry and study how to design a distributed controller to achieve reliable and scalable stability and robustness by using of *asymmetric* information graph. Direct optimization is in general not feasible in this case since the problem is not convex. So we start from symmetric design and examine the effect of introducing small asymmetry in the control gains. We show that the resulting design yields significant improvement of performance metrics (such as convergence rate and robustness to external disturbances) over symmetric design.

In this dissertation, we first consider the problem of controlling a large group of vehicles so that they maintain a rigid formation geometry while following a desired trajectory. The desired formation geometry is specified by constant inter-vehicle spacings. The desired trajectory of the formation is given in terms of a fictitious reference vehicle, whose trajectory can be accessed by only a small subset of the vehicles. One typical application of this problem is distributed control of vehicular platoons, which aims to maximize traffic throughput and increase driving safety. This topic has gained much attention in this past few decades [38, 38, 39, 39–48]. In the platoon problem, each vehicle in the formation makes its own control decision based on the relative information sensed from its immediate front and back neighbors. Although the dynamics of individual vehicle is independent of the others, the whole closed-loop becomes a coupled system.

Each vehicle in the formation is modeled as a double integrator. The double integrator is a commonly used model for vehicles dynamics, which results from feedback linearization of non-linear vehicle models [39, 49–51]. In fact, it was pointed out in [52, 53] that in the formation control problem, for any plant model $P(s)$ and local control law

$K(s)$, the key is to have two integrators in the loop gain $P(s)K(s)$. The single integrator dynamics will yield steady state tracking error while with three or more integrators the closed-loop becomes unstable for sufficient large number of vehicles. In addition to vehicle dynamics, the double integrator also has other applications such as spacecraft attitude control [54] and studying the motion of a free-floating particle [55]. Control of double-integrator agents has also been extensively studied for research and educational purposes [56–59].

We study how the stability margin and robustness to external disturbances scale with the number of vehicles, structure of information graph, and the choice of the control gains. The stability margin is defined as the absolute value of the real part of the least stable eigenvalue of the closed-loop. It quantifies the system's decay rate of initial errors. The robustness to external disturbance is measured by certain H_∞ norm of the system, which quantifies the system's disturbance rejection ability. In this work, we restrict ourselves to information graphs that belong to the class of D-dimensional (finite) lattices. Lattices arise naturally as information graphs when the vehicles in the group are arranged in a regular pattern in space and the exchange of information occurs between pairs of vehicles that are physically close. In addition, lattices also allow for a flexibility to model much more general information exchange architectures.

Besides vehicular formation control, we also study the problem of distributed consensus on a large network, in which each agent is modeled as a single integrator or its discrete counterpart. In distributed consensus, each agent updates its state by using a weighted summation of its own state and those from its neighbors in the network. The goal is to make all the agents' states asymptotically agree on a common value. Distributed consensus has been widely studied in the past decade due to its wide range of applications such as multi-agent rendezvous, information fusion in sensor network, coordinated control of multi-agent system, random walk on graphs [9–11]. The convergence rate of distributed consensus is very important, since it determines practical applicability of the protocol. If

the convergence rate is small, it will take many iterations before the states of all agents are sufficiently close. Similar to the formation control problem, distributed consensus also has a limitation. Its convergence rate on symmetric graphs degrades as the number of agents in the network increases [36]. The convergence rate is characterized by certain eigenvalue of its graph Laplacian. We examine how does the convergence rate scale with the number of agents in the network and how to design the graph weights to improve the convergence rate of distributed consensus.

1.2 Related Literature

Analysis of the stability margin and robustness to external disturbance is important to understand the scalability of control solutions as the number of vehicles in the formation, N, increases. In the formation control literature, the scalability question has been investigated primarily for a one-dimensional vehicle formation, which is usually referred to as a *platoon*. It's a special case of vehicular formation whose information graph is a 1-D lattice. An extensive literature exists on the platoon control problem; see [38, 43, 51, 60, 61] and references therein. The most widely studied information exchange architectures for distributed control of platoons are *predecessor following* architecture, *predecessor-leader following* architecture and *bidirectional* architecture. In the predecessor following architecture, every vehicle only uses information from its predecessor, i.e. the vehicle immediately ahead. In the predecessor-leader following architecture, besides the information from its immediate predecessor, the information of the leader is also used to compute the control action. In the bidirectional architecture, each vehicle uses the relative information from its immediate predecessor and follower. Scenarios in which information exchange occurs with vehicles beyond those physically closest, are studied in [53, 62]. Within the bidirectional architecture, the focus of much of the research in this area has been on the so-called *symmetric* bidirectional architecture, in which every vehicle put equal weight on the information received from its predecessor and follower. The symmetry assumption is used to simplify analysis and design.

In the platoon problem, it has been known for quite some time (see [31, 45, 46] and references therein) that the predecessor-following architecture suffers from extremely poor robustness to external disturbances. This is typically referred to as string instability or slinky-type effect [39, 44]. Seiler *et.al.* showed that string instability with the predecessor-following architecture is independent of the design of the controller on each vehicle, but a fundamental artifact of the architecture [31]. String instability can be ameliorated by non-identical controllers at the vehicles but at the expense of the control gains growing without bound as the number of the vehicles increases [39, 63]. In addition, it was shown in [31, 39] that if the predecessor-leader following architecture is used, the platoon is string stable. However, the requirement to transmit the leader's information to all the other vehicles makes this architecture unattractive. In addition, even a small time delay, which is inevitable in transmitting the leader's information to the following vehicles, is enough to cause string instability for large platoons [64, 65]. It should be mentioned that although string stability can also be achieved by constant headway control strategy [39], the constant headway policy by itself is not enough. The headway has to be *large enough* to avoid the problems associated with constant spacing policy [66]. Since one of the main motivations for automated platooning is to achieve higher highway capacity by making cars move with a small inter-vehicle separation, there is a need to study the constant spacing policy.

The poor robustness to disturbance of predecessor-following architecture led to the examination of the symmetric bidirectional architecture for its perceived advantage in rejecting disturbances, especially with absolute velocity feedback [46]. However, the distributed control architectures with symmetric control are latter shown to scale poorly in terms of closed-loop stability margin. Recall the stability margin is defined as the absolute value of the real part of the least stable eigenvalue. In a symmetric bidirectional architecture, the stability margin approaches zero as N increases [48]. Small stability margin will cause the system to take a long time to smooth out the initial

errors. Although it is superior over predecessor-following architecture in robustness to external disturbances (quantified by certain H_∞ norm), it was shown that the robustness performance of symmetric bidirectional architecture cannot be uniformly bounded with the size of the platoon either [31, 52]. Indeed, the poor robustness to disturbances persists even for more general architectures, when every vehicle uses information from more than two neighbors [62].

As mentioned before, most of the work on formation control and distributed consensus assume the information graph is symmetric. This symmetry assumption is crucial to make the analysis and control design tractable. It was also shown above that, the formation control problem with symmetric information graph suffers from fundamental limitation in the scalability of closed-loop performance. In addition, it was shown in [3, 62, 67] that with symmetric information graph, allowing heterogeneity in vehicle masses and on the weights of the information graph does not significantly alter the system's robustness to external disturbances. However, when the information is asymmetric, the situation becomes totally different, as we will show in this work. With asymmetric information graph, the analysis becomes extremely difficult, as there are few supporting techniques for asymmetric design. Two notable works with asymmetric design include [48, 68]. In [48], Barooah *et.al.* proposed a mistuning (asymmetric) design method to improve the closed-loop stability margin of vehicular platoon with relative position and absolute velocity feedback. Mistuning design refers to allowing small perturbation around the nominal control gains. It was shown that the resulting stability margin with mistuning design yields a order of magnitude improvement over symmetric design. In [68], Tangerman and Veerman considered the case of relative position and relative velocity feedback, and they put equal asymmetry on the position and velocity gains. It was concluded that the considered asymmetric control made the system's robustness to external disturbance much worse than symmetric control. More specifically, it was shown in [68] that a disturbance amplification

metric grows linearly in N for the symmetric bidirectional case but grows exponentially in N with the asymmetric control. The stability margin was not examined in their works.

In addition to the scaling of performance for the 1-D vehicular platoons, there are also a few other notable works on the vehicular formation in higher-dimensional space. Bamieh *et. al.* studied controlled vehicle formations with a D-dimensional torus as the information graph [32]. Scaling laws with symmetric control are obtained for certain performance measures that quantify the robustness of the closed-loop to stochastic noises. It was shown in [32] that the scaling of these performance measures with N was strongly dependent on the dimension D of the information graph. Darbha and Yadlapalli *et. al.* examined the limitation of employing symmetric information graph for arbitrary formation from the perspective system's robustness to sinusoidal disturbances [3, 53]. They concluded that with symmetric information graph, the H_∞ norm of the system cannot be uniformly bounded with the size of the formation. In [69], Pant *et. al.* introduced the notion of mesh-stability for two-dimensional formations with a "look-ahead" information exchange structure, which refers to a particular kind of directed information flow.

The degeneration of closed-loop performance with symmetry does not only exist in the formation control literature, it was also pointed out in [36] that the convergence rate of distributed consensus on lattices and geometric graphs with symmetric weights decayed to zero as the number of agents in the system increased, even with optimal symmetric weights obtained from convex optimization. In the formation control literature, the dynamics of each agent are usually described by a double integrator, while in the consensus research, the dynamics are in general given by a single integrator or its discrete counterpart. Although different in the dynamics models, they have the same limitation, i.e. the performance of the closed-loop degrades as the number of agents in the system increases. The loss of performance can be attributed to the degeneration of certain eigenvalues of the symmetric graph Laplacian when the size of the graph increases.

The literature on convergence rate of distributed consensus is not rich. A few works can be found in [70–72]. The related problem of mixing time of Markov chains is studied in [73]. In [36], convergence rate for a specific class of graphs, that we call L-Z geometric graphs, was established as a function of the number of agents. In general, the convergence rates of distributed consensus algorithms tend to be slow, and decrease as the number of agents increases. It was shown in [74] that the convergence rate could be arbitrarily fast in small-world networks. However, networks in which communication is only possible between agents that are close enough are not likely to be small-world.

One of the seminal works on improving convergence rates of distributed consensus protocols is convex optimization of weights on edges of the graph to maximize the consensus rate [27, 29]. Convex optimization imposes the constraint that the weights of the graph must be symmetric, which means any two neighboring agents put equal weight on the information received from each other. However, the convergence rates of distributed consensus protocols on graphs with symmetric weights degrade considerably as the number of agents in the network increases. In a D-dimensional lattice, for instance, the convergence rate is $O(1/N^{2/D})$ if the weights are symmetric, where N is the number of agents. This result follows as a special case of the results in [36]. Thus, the convergence rate becomes arbitrarily small if the size of the network grows without bound.

In [75, 76], finite-time distributed consensus protocols were proposed to improve the performance over asymptotic consensus. However, in general, the finite time needed to achieve consensus depends on the number of agents in the network. Thus, for large size of networks, although consensus can be reached in finite time, the time needed is very large [75, 76].

1.3 Contributions

In this dissertation, we study the performance scaling of distributed control of large-scale multi-agent systems with respect to its network size. We investigate two classes of distributed control problems: vehicular formation control and distributed consensus.

For the formation control problem, we describe a methodology for modeling, analysis, and distributed control design for large-scale vehicular teams whose information graphs belong to the class of D-dimensional lattices. The 1-D vehicular platoon is a special case, its information graph is a 1-D lattice. The approach is to use a partial differential equation (PDE) based continuous approximation of the (spatially) discrete platoon dynamics. Our PDE model yields the original set of ordinary differential equations upon discretization. This approach is motivated by earlier work on PDE modeling of one-dimensional platoons [48]. The PDE model is used for analysis of stability margin and robustness to disturbances as well as for asymmetric design of distributed control laws.

For the distributed consensus problem, we propose an asymmetric weight design method to improve its convergence rate. The asymmetric weight design idea is motivated by asymmetric design of distributed control laws for vehicular formations. Besides networks with D-dimensional lattice graphs, we also develop a weight design algorithm for more general graphs than lattices. The weight design method is based on a continuous approximation, in which the graph Laplacian of the network is approximated by a Sturm-Liouville operator [77]. We show that with the developed design method, the convergence rate of distributed consensus with asymmetric weights is improved significantly over that with symmetric weights.

There are five contributions of this work that are summarized below.

First, for formation with symmetric information graph, we obtain exact quantitative scaling laws of the closed-loop stability margin and robustness to external disturbances of the vehicular formation with respect to the number of vehicles in the system. We assume that only the vehicles on one boundary of the lattice have access to the desired trajectory of the reference vehicle. We show that the stability margin and robustness to external disturbance only depend on N_1, where N_1 is the number of vehicles along the axis that is perpendicular to the boundary where the reference vehicles are located. By choosing the structure of the information graph in such a way that N_1 increases slowly in relation to

N, the reduction of the stability margin and disturbance amplification as a function of N can be slowed down. In fact, by holding N_1 to be a constant independent of the number of vehicles N, the stability margin and disturbance amplification can be bounded away from zero even as the number of vehicles increase without bound. It turns out, however, that keeping N_1 fixed while N increases causes long range communication and/or the number of vehicles that have access to the desired trajectory of the reference vehicle to increase. In addition, when the information graph is square, which means there are equal number of vehicles in each axis of the information graph, we show that the exponents of the scaling laws of the stability margin and disturbance amplification depend on D, the dimension of the information graph. The stability margin and disturbance amplification can be improved considerably by applying a higher-dimensional information graph.

The second contribution of this work is a procedure to design *asymmetric* control gains so that the stability margin and disturbance amplification scaling laws are significantly improved over those with symmetric control. For the 1-D vehicular platoon, we show that with *asymmetric velocity feedback*, which allows an arbitrarily small asymmetry in the velocity gains from their nominal symmetric values, results in stability margin scaling as $O(\frac{1}{N})$, where N is the number of vehicles in the platoon. In contrast to the $O(\frac{1}{N^2})$ scaling seen in the symmetric case, this is an order of magnitude improvement. In addition, when there is equal amount of asymmetry in both the position and velocity feedback, the stability margin can be improved even better to $O(1)$, which is independent of the size of the network. This asymmetric design thus eliminates the problem of decay to stability margin with increasing N, as seen with symmetric design. In terms of disturbance amplification, it was shown by Veerman that asymmetric design with equal asymmetry in the position and velocity feedback had worse robustness to external disturbances compared to symmetric case [33]. However, if asymmetry is only introduced into the relative velocity feedback (*asymmetric velocity feedback*), numerical simulations show that the disturbance amplification can be improved significantly over symmetric design. Therefore, to achieve

better stability margin and robustness to external disturbance simultaneously, *asymmetric velocity feedback* is the best design choice. The asymmetric design method can also be extended to vehicular formations with higher-dimensional lattice information graphs.

The third contribution of the work is we show that heterogeneity in vehicle mass and control gains has little effect on the stability margin of a vehicular platoon. In particular, we show that the allowing heterogeneity only changes the coefficient of the scaling law of the stability margin but not its asymptotic trend with N, where N is the number of vehicles in the platoon. As long as the control is symmetric, the scaling law of the stability margin with and without heterogeneity are both $O(1/N^2)$. In connection to optimizing the eigenvalues of graph Laplacian, our results show that for symmetric graphs, even by convex optimization, which allows heterogeneity on the weights of the graph to optimize its eigenvalues, the degeneration of certain eigenvalues is inevitable when the size of the graph increases. Similar results were obtained independently in [36].

The fourth contribution of the work is the approach used in deriving the results mentioned above. We derive a partial differential equation (PDE) based continuous approximation of the (spatially) discrete formation dynamics. Partial differential equations have been gaining attention in studying large-scale distributed systems such as power networks, coupled-oscillators and extremely large telescopes [6, 78–81]. A PDE approximation is also frequently used in the analysis of many-particle systems in statistical physics and traffic-dynamics; see [82] and the references therein. Due to the large scale feature of the studied system, the classical coupled-ODE (ordinary differential equation) model seems unapt and inefficient, and it provides no insight on analysis and design. The PDE model provides a single compact model for the whole system, regardless of how many agents are in the system. The advantage of using a PDE-based analysis is that the PDE reveals, better than the state-space model does, the mechanism of loss of stability and suggests the asymmetric design approach to ameliorate it. In addition, the PDE model gives more insight on the system's frequency response, which aids to derive the scaling law of the

robustness to external disturbance (quantified by certain H_∞ norm). Numerical computations of the stability margin and H_∞ norm of the state-space model of the formation are used to confirm the PDE predictions. Although the PDE model approximates the (spatially) discrete formation dynamics in the limit $N \to \infty$, numerical calculations show that the conclusions drawn from the PDE-based analysis holds even for small number of vehicles. Almost of all the scaling laws derived in the work can be established by analyzing the state-space model with the control gains suggested by the PDE model. In fact, the publications resulting from this work contains such analysis. We don't present the analysis in this work to avoid repetition.

The last but not the least contribution is a method to improve the convergence rate of distributed consensus protocols through *asymmetric* weights. We first consider lattice graphs, and show that with proper choice of asymmetric weights, the convergence rate of distributed consensus can be bounded away from zero uniformly in N. Thus, the proposed asymmetric design makes distributed consensus highly scalable. We next propose a weight design algorithm for 2-dimensional geometric graphs, i.e., graphs consisting of nodes in $\mathbb{R}^2$. Numerical simulations show that the convergence rate with asymmetric designed weights in large graphs is an order of magnitude higher than that with (i) optimal symmetric weights, which are obtained by convex optimization, and (ii) asymmetric weights obtained by Metropolis-Hastings method, which assigns weights uniformly to each edge connecting itself to its neighbor. The proposed weight design method is decentralized; every node can obtain its own weight based on the angular position measurements with its neighbors. In addition, it is computationally much cheaper than obtaining the optimal symmetric weights using convex optimization method. The proposed weight design method can be extended to geometric graphs in $\mathbb{R}^D$, but in this work we limit ourselves to $\mathbb{R}^2$.

The remainder of this dissertation is organized as follows. For ease of description, we first present the problem and results on 1-D vehicular platoon. Chapter 2 presents scaling laws of stability margin of the 1-D vehicular platoon with symmetric control as well as

the effect of asymmetric design on the closed-loop stability margin. Chapter 3 describes the scaling laws of robustness to external disturbances of the 1-D vehicular platoon and asymmetric design to improve the disturbance amplification. Distributed control of vehicular formation in higher-dimensional space and the effect of network structure on the scaling laws of stability margin and robustness are presented in Chapter 4. The method of improving convergence rate of distributed consensus through asymmetric weights design is described in Chapter 5. The dissertation ends with conclusions and future works in Chapter 6.

CHAPTER 2
STABILITY MARGIN OF 1-D VEHICULAR PLATOON

In this chapter we examine the closed-loop stability margin of a vehicular platoon consisting of N vehicles, in which each vehicle is modeled as a double-integrator and interacts with its two nearest neighbors (one on either side) through its local control action. This is a problem that is of primary interest to automated platoon in smart highway systems. In the vehicular platoon problem, the formation aims to track a desired trajectory while maintaining a rigid formation geometry. The desired trajectory of the entire vehicular platoon is given in terms of trajectory of a fictitious reference vehicle, and the desired formation geometry is specified in terms of constant inter-vehicle spacings.

Although significant amount of research has been conducted on robustness-to-disturbance and stability issues of double integrator networks with decentralized control, most investigations consider the homogeneous case in which each vehicle has the same mass and employs the same controller (exceptions include [15, 62, 63]). In addition, only symmetric control laws are considered in which the information from both the neighboring vehicles are weighted equally, with [33, 48] being exceptions. Khatir *et. al.* proposed heterogeneous control gains to improve string stability (sensitivity to disturbance) at the expense of control gains increasing without bound as N increases [63]. Middleton *et. al.* considered both unidirectional and bidirectional control, and concluded heterogeneity had little effect on the string stability under certain conditions on the high frequency behavior and integral absolute error [62]. On the other hand, [33] examined the effect of equal asymmetry in position and velocity gains (but not heterogeneity) on the response of the platoon as a result of sinusoidal disturbance in the lead vehicle, and concluded that this asymmetry made sensitivity to such disturbances worse.

In this chapter we analyze the case when the vehicles are *heterogeneous* in their masses and control laws used, and also allow asymmetry in the use of front and back

information. A decentralized *bidirectional* control law not necessarily symmetric is considered that uses only relative position and relative velocity information from the nearest neighbors. We examine the effect of heterogeneity and asymmetry on the stability margin of the closed loop, which is measured by the absolute value of the real part of the least stable pole. The stability margin determines the decay rate of initial formation keeping errors. Such errors arise from poor initial arrangement of the vehicles. The main result of the chapter is that in a decentralized bidirectional control strategy, heterogeneity has little effect on the stability margin of the overall closed loop, while even small asymmetry can have a significant impact. In particular, we show that in the symmetric case, the stability margin decays to 0 as $O(1/N^2)$, where N is the number of vehicles. We also show that the asymptotic scaling trend of stability margin is not changed by vehicle-to-vehicle heterogeneity. On the other hand, arbitrary small amount of asymmetry in the way the local controllers use front and back information can improve the stability margin by a considerable amount. When each vehicle weighs the relative velocity information from its front neighbor more heavily than the one behind it, the stability margin scaling trend can be improved from $O(1/N^2)$ to $O(1/N)$. In contrast, if more weight is given to the relative velocity information with the neighbor behind it, the closed loop becomes unstable if N is sufficiently large. In addition, when there is equal amount of asymmetry in position and velocity feedback gains, the closed-loop is exponentially stable for arbitrary finite N, and the stability margin can be uniformly bounded with the size of the network. This result makes it possible to design the control gains so that the stability margin of the system satisfies a pre-specified value irrespective of how many vehicles are in the formation.

The results are established by using a PDE model. The PDE model approximates the coupled system of ODEs that govern the closed loop dynamics of the network. This is inspired by the work [48] that examined stability margin of 1-D vehicular platoons in a similar framework. Compared to [48], this work makes two novel contributions. First, we consider heterogeneous vehicles (the mass and control gains vary from vehicle to vehicle),

whereas [48] consider only homogeneous vehicles. Secondly, [48] considered the scenario in which every vehicle knew the desired velocity of the platoon. In contrast, the control law we consider requires vehicles to know only the desired inter-vehicle separation; the overall trajectory information is made available only to vehicle 1. This makes the model more applicable to practical formation control applications. It was shown in [48] for the homogeneous formation that asymmetry in the position feedback can improve the stability margin from $O(1/N^2)$ to $O(1/N)$ while the absolute velocity feedback gain did not affect the asymptotic trend. In contrast, we show in this chapter that with relative position and relative velocity feedback, asymmetry in the velocity feedback gain alone and in both position and velocity feedback gains are both important. The stability margin can be improved considerably by a judicious choice of asymmetry.

The PDE model provides insights into loss of stability margin with symmetric control and suggests an asymmetric design method to improve the stability margin. Although the PDE approximation is valid only in the limit $N \to \infty$, numerical comparisons with the original state-space model shows that the PDE model provides accurate results even for small N (5 to 10). The PDE approximation is often used in studying many-particle systems and in analyzing multi-vehicle coordination problems [48, 79, 80, 82]. A similar but distinct framework based on partial *difference* equations has been developed by Ferrari-Trecate *et. al.* [83].

The rest of this chapter is organized as follows. Section 2.1 presents the problem statement and the main results. Section 2.2 describes the PDE model of closed-loop dynamics. Analysis and control design results together with their numerical corroboration appear in Section 2.3-Section 2.5, respectively. This section ends with summary in Section 2.6.

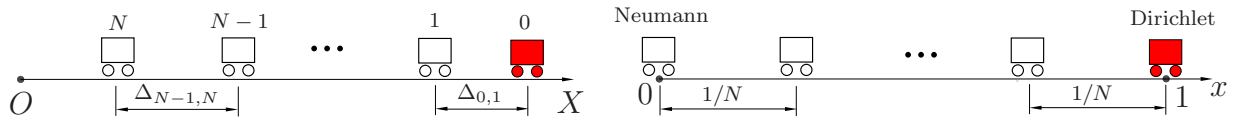

(a) A pictorial representation of a platoon.

(b) A Redrawn graph of the same platoon.

Figure 2-1. Desired geometry of a platoon with N vehicles and 1 reference vehicle.

2.1 Problem Formulation and Main Results

2.1.1 Problem Formulation

We consider the formation control of N heterogeneous vehicles which are moving in 1-D Euclidean space, as shown in Figure 2-1 (a). The position and mass of each vehicle are denoted by p_i and m_i respectively. The mass of each vehicle is bounded, $|m_i - m_0|/m_0 \leq \delta$ for all i, where $m_0 > 0$ and $\delta \in [0, 1)$ are constants. The dynamics of each vehicle are modeled as a double integrator:

$$m_i \ddot{p}_i = u_i, \tag{2–1}$$

where u_i is the control input (acceleration or deceleration command). This is a commonly used model for vehicle dynamics in studying vehicular formations, which results from feedback linearization of non-linear vehicle dynamics [39, 49].

The desired trajectory of the formation is given in terms of a *fictitious* reference vehicle with index 0 whose trajectory is denoted by $p_0^*(t)$. Since we are interested in translational maneuvers of the formation, we assume the desired trajectory is a constant-velocity type, i.e. $p_0^*(t) = v_0 t + c_0$ for some constants v_0 and c_0. The information on the desired trajectory of the network is provided only to vehicle 1. The desired geometry of the formation is specified by the *desired gaps* $\Delta_{i-1,i}$ for $i = 1, \ldots, N$, where $\Delta_{i-1,i}$ is the desired value of $p_{i-1}(t) - p_i(t)$. The control objective is to maintain a rigid formation, i.e., to make neighboring vehicles maintain their pre-specified desired gaps and to make vehicle 1 follow its desired trajectory $p_0^*(t) - \Delta_{0,1}$. Since we are only interested in maintaining rigid formations that do not change shape over time, $\Delta_{i-1,i}$'s are positive constants.

In this chapter, we consider the following *decentralized* control law, whereby the control action at the i-th vehicle depends on i) the *relative position measurements* ii) the *relative velocity measurements* with its immediate neighbors in the formation:

$$u_i = -k_i^f(p_i - p_{i-1} + \Delta_{i-1,i}) - k_i^b(p_i - p_{i+1} - \Delta_{i,i+1}) - b_i^f(\dot{p}_i - \dot{p}_{i-1}) - b_i^b(\dot{p}_i - \dot{p}_{i+1}), \quad (2\text{–}2)$$

where $i = \{1, \ldots, N-1\}$, k_i^f, k_i^b are the front and back position gains and b_i^f, b_i^b are the front and back velocity gains of the i-th vehicle respectively. For the vehicle with index N which does not have a vehicle behind it, the control law is slightly different:

$$u_N = -k_N^f(p_N - p_{N-1} + \Delta_{N-1,N}) - b_N^f(\dot{p}_N - \dot{p}_{N-1}). \quad (2\text{–}3)$$

Each vehicle i knows the desired gaps $\Delta_{i-1,i}$ and $\Delta_{i,i+1}$, while only vehicle 1 knows the desired trajectory $p_0^*(t)$ of the fictitious reference vehicle.

Combining the open loop dynamics (2–1) with the control law (2–2), we get

$$m_i\ddot{p}_i = -k_i^f(p_i - p_{i-1} + \Delta_{i-1,i}) - k_i^b(p_i - p_{i+1} - \Delta_{i,i+1}) - b_i^f(\dot{p}_i - \dot{p}_{i-1}) - b_i^b(\dot{p}_i - \dot{p}_{i+1}), \quad (2\text{–}4)$$

where $i \in \{1, \ldots, N-1\}$. The dynamics of the N-th vehicle are obtained by combining (2–1) and (2–3), which are slightly different from (2–4). The desired trajectory of the i-th vehicle is $p_i^*(t) := p_0^*(t) - \Delta_{0,i} = p_0^*(t) - \sum_{j=1}^{i} \Delta_{j-1,j}$. To facilitate analysis, we define the following tracking error:

$$\tilde{p}_i := p_i - p_i^* \qquad \Rightarrow \qquad \dot{\tilde{p}}_i = \dot{p}_i - \dot{p}_i^*. \quad (2\text{–}5)$$

Substituting (2–5) into (2–4), and using $p_{i-1}^*(t) - p_i^*(t) = \Delta_{i-1,i}$, we get

$$m_i\ddot{\tilde{p}}_i = -k_i^f(\tilde{p}_i - \tilde{p}_{i-1}) - k_i^b(\tilde{p}_i - \tilde{p}_{i+1}) - b_i^f(\dot{\tilde{p}}_i - \dot{\tilde{p}}_{i-1}) - b_i^b(\dot{\tilde{p}}_i - \dot{\tilde{p}}_{i+1}). \quad (2\text{–}6)$$

By defining the state $X := [\tilde{p}_1, \dot{\tilde{p}}_1, \tilde{p}_2, \dot{\tilde{p}}_2, \cdots, \tilde{p}_N, \dot{\tilde{p}}_N]^T$, the closed loop dynamics of the network can now be written compactly from (2–6) as:

$$\dot{X} = AX \tag{2–7}$$

where A is the closed-loop state matrix and we have used the fact that $\tilde{p}_0(t) = \dot{\tilde{p}}_0(t) \equiv 0$ since the trajectory of the reference vehicle is equal to its desired trajectory.

2.1.2 Main Results

The main results of this chapter rely on the analysis of the following PDE (partial differential equation) model of the network, which is seen as a continuum approximation of the closed-loop dynamics (2–6). The details of derivation of the PDE model are given in Section 2.2. The PDE is given by

$$m(x)\frac{\partial^2 \tilde{p}(x,t)}{\partial t^2} = \Big(\frac{k^{f-b}(x)}{N}\frac{\partial}{\partial x} + \frac{k^{f+b}(x)}{2N^2}\frac{\partial^2}{\partial x^2} + \frac{b^{f-b}(x)}{N}\frac{\partial^2}{\partial x \partial t} + \frac{b^{f+b}(x)}{2N^2}\frac{\partial^3}{\partial x^2 \partial t}\Big)\tilde{p}(x,t), \tag{2–8}$$

with boundary conditions:

$$\tilde{p}(1,t) = 0, \qquad \frac{\partial \tilde{p}}{\partial x}(0,t) = 0, \tag{2–9}$$

where $k^{f-b}(x), k^{f+b}(x), b^{f-b}(x)$ and $b^{f+b}(x)$ are defined as follows:

$$k^{f+b}(x) := k^f(x) + k^b(x), \qquad k^{f-b}(x) := k^f(x) - k^b(x),$$
$$b^{f+b}(x) := b^f(x) + b^b(x), \qquad b^{f-b}(x) := b^f(x) - b^b(x),$$

and $m(x), k^f(x), k^b(x), b^f(x), b^b(x)$ are respectively the continuum approximations of $m_i, k_i^f, k_i^b, b_i^f, b_i^b$ of each vehicle with the following stipulation:

$$k_i^{f \text{ or } b} = k^{f \text{ or } b}(x)|_{x=\frac{N-i}{N}}, \qquad b_i^{f \text{ or } b} = b^{f \text{ or } b}(x)|_{x=\frac{N-i}{N}}, \qquad m_i = m(x)|_{x=\frac{N-i}{N}}. \tag{2–10}$$

We formally define symmetric control, homogeneity and stability margin before stating the first main result, i.e. the role of heterogeneity on the stability margin of the network.

Definition 2.1. *The control law (2–2) is* symmetric *if each vehicle uses the same front and back control gains: $k_i^f = k_i^b$, $b_i^f = b_i^b$, for all $i \in \{1, 2, \cdots, N-1\}$, and is called* homogeneous *if $k_i^f = k_j^f$, $k_i^b = k_j^b$ and $b_i^f = b_j^f$, $b_i^b = b_j^b$ for each pair of neighboring vehicles (i, j).* □

Definition 2.2. *The stability margin of a closed-loop system, which is denoted by S, is the absolute value of the real part of the least stable pole of the closed-loop dynamics.* □

Theorem 2.1. *Consider the PDE model (2–8) of the network with boundary condition (2–9), where the mass and the control gain profiles satisfy $|m(x) - m_0|/m_0 \leq \delta$, $|k^{(\cdot)}(x) - k_0|/k_0 \leq \delta$ and $|b^{(\cdot)}(x) - b_0|/b_0 \leq \delta$ for all $x \in [0, 1]$ where m_0, k_0 and b_0 are positive constants, and $\delta \in [0, 1)$ denotes the percent of heterogeneity. With symmetric control, the stability margin S of the network satisfies the following:*

$$(1 - 2\delta)\frac{\pi^2 b_0}{8m_0}\frac{1}{N^2} \leq S \leq (1 + 2\delta)\frac{\pi^2 b_0}{8m_0}\frac{1}{N^2}, \tag{2–11}$$

when $\delta \ll 1$. □

The result above is also provable for an arbitrary $\delta < 1$ (not necessarily small) when the position gain is proportional to the velocity gain using standard results of Sturm-Liouville theory [77, Chapter 5]. For that case, the result is given in the following lemma and its proof is given in the end of Section 2.7.

Theorem 2.2. *Consider the PDE model (2–8) of the network with boundary condition (2–9). Let the mass and the control gains satisfy $0 < m_{min} \leq m(x) \leq m_{max}$, $0 < b_{min} \leq b^f(x) = b^b(x) = b(x) \leq b_{max}$ and $k^f(x) = k^b(x) = k(x) = \rho b(x)$ for all $x \in [0, 1]$, where $m_{min}, m_{max}, b_{min}, b_{max}$ and ρ are positive constants. The stability margin S of the*

network satisfies the following:

$$\frac{\pi^2 b_{min}}{8m_{max}}\frac{1}{N^2} \leq S \leq \frac{\pi^2 b_{max}}{8m_{min}}\frac{1}{N^2}. \qquad \square$$

The main implication of the result above is that *heterogeneity of masses and control gains plays no role in the asymptotic trend of the stability margin with N as long as the control gains are symmetric*. Note that the $O(1/N^2)$ decay of the stability margin described above has been shown for homogeneous platoons (all vehicles have the same mass and use the same control gains) independently in [35], although the dynamics of the last vehicle are slightly different from ours. A similar result for homogeneous platoons with relative position and absolute velocity feedback was also established in [48].

The second main result of this work is that the stability margin can be greatly improved by introducing front-back asymmetry in the *velocity*-feedback gains. We call the resulting design *mistuning*-based design because it relies on small changes from the nominal symmetric gain b_0. In addition, a poor choice of such asymmetry can also make the closed loop unstable. In general, heterogeneity in mass has little effect on the scaling trends of eigenvalues of PDE [77, Chapter 5]. For ease of analysis, we let $m_i = m_0$ in the sequel.

Theorem 2.3. *For an N-vehicle network with PDE model (2–8) and boundary condition (2–9). Let $m(x) = m_0$ for all $x \in [0,1]$, consider the problem of maximizing the stability margin by choosing the control gains with the constraint $|b^{(\cdot)}(x) - b_0|/b_0 \leq \varepsilon$, where ε is a positive constant, and $k^{(f)}(x) = k^{(b)}(x) = k_0$. If $\varepsilon \ll 1$, the optimal velocity gains are*

$$b^f(x) = (1+\varepsilon)b_0, \qquad\qquad b^b(x) = (1-\varepsilon)b_0, \tag{2–12}$$

which result in the stability margin

$$S = \frac{\varepsilon b_0}{m_0}\frac{1}{N} + O(\frac{1}{N^2}) = O(\frac{1}{N}). \tag{2–13}$$

The formula is asymptotic in the sense that it holds for large N and small ε. In contrast, for the following choice of asymmetry

$$b^f(x) = (1-\varepsilon)b_0 \qquad b^b(x) = (1+\varepsilon)b_0, \tag{2–14}$$

where $0 < \varepsilon \ll 1$ is a small positive constant, the closed loop becomes unstable for sufficiently large N. □

The theorem says that with arbitrarily small change in the front-back asymmetry, so that velocity information from the front is weighted more heavily than the one from the back, the stability margin can be improved significantly over symmetric control. On the other hand, if velocity information from the back is weighted more heavily than that from the front, the closed loop will become unstable if the network is large enough. It is interesting to note that the optimal gains turn out to be homogeneous, which again indicates that heterogeneity has little effect on the stability margin.

The astute reader may inquire at this point what are the effects of introducing asymmetry in the position-feedback gains while keeping velocity gains symmetric, or introducing asymmetry in both position and velocity feedback gains. It turns out when equal asymmetry in both position and velocity feedback gains are introduced, the closed loop is exponentially stable for arbitrary N. Moreover, the stability margin scaling trend can be uniformly bounded below in N when more weights are given to the information from its front neighbor. We state the result in the next theorem.

Theorem 2.4. *For an N-vehicle network with PDE model (2–8) and boundary condition (2–9). Let $m(x) = m_0$ for all $x \in [0,1]$. With the following asymmetry in control $k^f(x) = (1+\varepsilon)k_0$, $k^b(x) = (1-\varepsilon)k_0$, $b^f(x) = (1+\varepsilon)b_0$, $b^b(x) = (1-\varepsilon)b_0$, where ε is the amount of asymmetry satisfying $\varepsilon \in (0,1)$, the stability margin of the network can be uniformly bounded below as follows:*

$$S \geq \min\left\{\frac{b_0\varepsilon^2}{2m_0}, \frac{k_0}{b_0}\right\} = O(1).$$ □

This asymmetric design therefore makes the resulting control law highly scalable; it eliminates the degradation of closed-loop stability margin with increasing N. It is now possible to design the control gains so that the stability margin of the system satisfies a pre-specified value irrespective of how many vehicles are in the formation. The result above is for equal amount of asymmetry in the position feedback and velocity feedback gains. This constraint of equal asymmetry in position and velocity feedback is imposed in order to make the analysis tractable.

As we see from the previous results, heterogeneity has little effect on the scaling law of stability margin, while asymmetry has a huge effect. One may wonder how does the stability margin scale when there is both heterogeneity and asymmetry in the system? The following theorem answers the question for this scenario. In particular, we consider two cases. One case is asymmetric velocity feedback with small heterogeneity, the other case is when there is equal asymmetry in both position and velocity feedbacks as well as small heterogeneity.

Theorem 2.5. *Consider an N-vehicle network with PDE model (2–8) and boundary condition (2–9).*

1) When there is small asymmetry only in the velocity feedback and small heterogeneity in the control gain functions, i.e. $m(x) = m_0$, $k^{(f)}(x) = k^{(b)}(x)$, $|k^{(\cdot)}(x) - k_0|/k_0 \leq \varepsilon$, $b^{(f)}(x) - b^{(b)}(x) = 2\varepsilon b_0$, $|b^{(\cdot)}(x) - b_0|/b_0 \leq \varepsilon$, where ε is a small positive constant. If $\varepsilon \ll 1$, the stability margin of the network satisfies

$$S = O(\frac{1}{N}).$$

2) Where is equal amount of asymmetry in both position and velocity feedback as well as small heterogeneity in the control gains, i.e. $m(x) = m_0$, $k^{(f)}(x) - k^{(b)}(x) = 2\varepsilon k_0$, $|k^{(\cdot)}(x) - k_0|/k_0 \leq \varepsilon$, $b^{(f)}(x) - b^{(b)}(x) = 2\varepsilon b_0$, $|b^{(\cdot)}(x) - b_0|/b_0 \leq \varepsilon$. If $\varepsilon \ll 1$, the stability margin of the network satisfies

$$S = O(1).$$ □

Comparing the above theorem to Theorem 2.1 and Theorem 2.4, we show that no matter the control is symmetric or asymmetric, introducing heterogeneity in control gains does not change the scaling law of stability margin with respect to the number of vehicles in the platoon. The scaling law is only determined by asymmetry (and its type).

2.2 PDE Model of the Closed-Loop Dynamics

In this chapter, all the analysis and design is performed using a PDE model, whose results are validated by numerical computations using the state-space model (2–7). We now derive a continuum approximation of the coupled-ODEs (2–6) in the limit of large N, by following the steps involved in a finite-difference discretization in reverse. We define

$$k_i^{f+b} := k_i^f + k_i^b, \qquad k_i^{f-b} := k_i^f - k_i^b,$$
$$b_i^{f+b} := b_i^f + b_i^f, \qquad b_i^{f-b} := b_i^f - b_i^b.$$

Substituting these into (2–6), we have

$$\begin{aligned} m_i \ddot{\tilde{p}}_i = &- \frac{k_i^{f+b} + k_i^{f-b}}{2}(\tilde{p}_i - \tilde{p}_{i-1}) - \frac{k_i^{f+b} - k_i^{f-b}}{2}(\tilde{p}_i - \tilde{p}_{i+1}) \\ &- \frac{b_i^{f+b} + b_i^{f-b}}{2}(\dot{\tilde{p}}_i - \dot{\tilde{p}}_{i-1}) - \frac{b_i^{f+b} - b_i^{f-b}}{2}(\dot{\tilde{p}}_i - \dot{\tilde{p}}_{i+1}). \end{aligned} \tag{2–15}$$

To facilitate analysis, we redraw the graph of the 1D network, so that each vehicle in the new graph is drawn in the interval $[0, 1]$, irrespective of the number of vehicles. The i-th vehicle in the "original" graph, is now drawn at position $(N - i)/N$ in the new graph. Figure 2-1 shows an example.

The starting point for the PDE derivation is to consider a function $\tilde{p}(x, t) : [0, 1] \times [0, \infty) \to \mathbb{R}$ that satisfies:

$$\tilde{p}_i(t) = \tilde{p}(x, t)|_{x=(N-i)/N}, \tag{2–16}$$

such that functions that are defined at discrete points i will be approximated by functions that are defined everywhere in $[0, 1]$. The original functions are thought of as samples of their continuous approximations. We formally introduce the following scalar functions

$k^f(x), k^b(x), b^f(x), b^b(x)$ and $m(x) : [0,1] \to \mathbb{R}$ defined according to the stipulation:

$$k_i^{f \text{ or } b} = k^{f \text{ or } b}(x)|_{x=\frac{N-i}{N}}, \qquad b_i^{f \text{ or } b} = b^{f \text{ or } b}(x)|_{x=\frac{N-i}{N}}, \qquad m_i = m(x)|_{x=\frac{N-i}{N}}. \tag{2–17}$$

In addition, we define functions $k^{f+b}(x)$, $k^{f-b}(x)$, $b^{f+b}(x)$, $b^{f-b}(x) : [0,1]^D \to \mathbb{R}$ as

$$\begin{aligned} k^{f+b}(x) &:= k^f(x) + k^b(x), & k^{f-b}(x) &:= k^f(x) - k^b(x), \\ b^{f+b}(x) &:= b^f(x) + b^b(x), & b^{f-b}(x) &:= b^f(x) - b^b(x). \end{aligned}$$

Due to (2–17), these satisfy

$$\begin{aligned} k_i^{f+b} &= k^{f+b}(x)|_{x=(N-i)/N}, & k_i^{f-b} &= k^{f-b}(x)|_{x=(N-i)/N} \\ b_i^{f+b} &= b^{f+b}(x)|_{x=(N-i)/N}, & b_i^{f-b} &= b^{f-b}(x)|_{x=(N-i)/N}. \end{aligned}$$

To obtain a PDE model from (2–15), we first rewrite it as

$$\begin{aligned} m_i \ddot{\tilde{p}}_i =& \frac{k_i^{f-b}}{N} \frac{(\tilde{p}_{i-1} - \tilde{p}_{i+1})}{2(1/N)} + \frac{k_i^{f+b}}{2N^2} \frac{(\tilde{p}_{i-1} - 2\tilde{p}_i + \tilde{p}_{i+1})}{1/N^2} \\ &+ \frac{b_i^{f-b}}{N} \frac{(\dot{\tilde{p}}_{i-1} - \dot{\tilde{p}}_{i+1})}{2(1/N)} + \frac{b_i^{f+b}}{2N^2} \frac{(\dot{\tilde{p}}_{i-1} - 2\dot{\tilde{p}}_i + \dot{\tilde{p}}_{i+1})}{1/N^2}. \end{aligned} \tag{2–18}$$

Using the following finite difference approximations:

$$\begin{aligned} \left[\frac{\tilde{p}_{i-1} - \tilde{p}_{i+1}}{2(1/N)}\right] &= \left[\frac{\partial \tilde{p}(x,t)}{\partial x}\right]_{x=(N-i)/N}, & \left[\frac{\tilde{p}_{i-1} - 2\tilde{p}_i + \tilde{p}_{i+1}}{1/N^2}\right] &= \left[\frac{\partial^2 \tilde{p}(x,t)}{\partial x^2}\right]_{x=(N-i)/N}, \\ \left[\frac{\dot{\tilde{p}}_{i-1} - \dot{\tilde{p}}_{i+1}}{2(1/N)}\right] &= \left[\frac{\partial^2 \tilde{p}(x,t)}{\partial x \partial t}\right]_{x=(N-i)/N}, & \left[\frac{\dot{\tilde{p}}_{i-1} - 2\dot{\tilde{p}}_i + \dot{\tilde{p}}_{i+1}}{1/N^2}\right] &= \left[\frac{\partial^3 \tilde{p}(x,t)}{\partial x^2 \partial t}\right]_{x=(N-i)/N}. \end{aligned}$$

For large N, Eq. (2–18) can be seen as a finite difference discretization of the following PDE:

$$m(x)\frac{\partial^2 \tilde{p}(x,t)}{\partial t^2} = \Big(\frac{k^{f-b}(x)}{N}\frac{\partial}{\partial x} + \frac{k^{f+b}(x)}{2N^2}\frac{\partial^2}{\partial x^2} + \frac{b^{f-b}(x)}{N}\frac{\partial^2}{\partial x \partial t} + \frac{b^{f+b}(x)}{2N^2}\frac{\partial^3}{\partial x^2 \partial t}\Big)\tilde{p}(x,t).$$

The boundary conditions of the above PDE depend on the arrangement of reference vehicle in the redrawn graph of the network. For our case, the boundary condition is of

Dirichlet type at $x = 1$ where the reference vehicle is, and of Neumann type at $x = 0$:

$$\tilde{p}(1,t) = 0, \qquad \frac{\partial \tilde{p}}{\partial x}(0,t) = 0.$$

2.3 Role of Heterogeneity on Stability Margin

The starting point of our analysis is the investigation of the homogeneous and symmetric case: $m_i = m_0, k_i^{(\cdot)} = k_0, b_i^{(\cdot)} = b_0$ for some positive constants m_0, k_0, b_0, where $i \in \{1, \dots, N\}$. The analysis leading to the proof of Theorem 2.1 is carried out using the PDE model derived in the previous section. In the homogeneous and symmetric control case, using the notation introduced earlier, we get

$$m(x) = m_0, \quad k^{f+b}(x) = 2k_0, \quad k^{f-b}(x) = 0, \quad b^{f+b}(x) = 2b_0, \quad b^{f-b}(x) = 0.$$

The PDE (2–8) simplifies to:

$$m_0 \frac{\partial^2 \tilde{p}(x,t)}{\partial t^2} = \frac{k_0}{N^2} \frac{\partial^2 \tilde{p}(x,t)}{\partial x^2} + \frac{b_0}{N^2} \frac{\partial^3 \tilde{p}(x,t)}{\partial x^2 \partial t}. \tag{2–19}$$

This is a wave equation with Kelvin-Voigt damping. Due to the linearity and homogeneity of the above PDE and boundary conditions, we are able to apply the method of separation of variables. We assume a solution of the form $\tilde{p}(x,t) = \sum_{\ell=1}^{\infty} \phi_\ell(x) h_\ell(t)$. Substituting it into PDE (2–19), we obtain the following time-domain ODE

$$m_0 \frac{d^2 h_\ell(t)}{dt^2} + \frac{b_0 \lambda_\ell}{N^2} \frac{dh_\ell(t)}{dt} + \frac{k_0 \lambda_\ell}{N^2} h_\ell(t) = 0, \tag{2–20}$$

where λ_ℓ solves the boundary value problem

$$\frac{d^2 \phi_\ell(x)}{dx^2} + \lambda_\ell \phi_\ell(x) = 0, \tag{2–21}$$

with the following boundary conditions, which come from (2–9):

$$\frac{d\phi_\ell}{dx}(0) = 0, \quad \phi_\ell(1) = 0. \tag{2–22}$$

Following straightforward algebra, the eigenvalues and eigenfunction of the above boundary value problem is given by (see [77] for a BVP example)

$$\lambda_\ell = \pi^2 \frac{(2\ell-1)^2}{4}, \quad \phi_\ell(x) = cos(\frac{2\ell-1}{2}\pi x), \quad \ell = 1, 2, \cdots. \tag{2–23}$$

Take Laplace transform to both sides of the (2–20) with respect to the time variable t, we obtain the characteristic equation of the PDE (2–19):

$$m_0 s^2 + \frac{b_0 \lambda_\ell}{N^2} s + \frac{k_0 \lambda_\ell}{N^2} = 0.$$

The eigenvalues of the PDE (2–19) are now given by

$$s_\ell^{\pm} = -\frac{\lambda_\ell b_0}{2m_0 N^2} \pm \frac{1}{2m_0 N} \sqrt{\frac{\lambda_\ell^2 b_0^2}{N^2} - 4\lambda_\ell m_0 k_0} \tag{2–24}$$

For small ℓ and large N so that $N > (2\ell-1)\pi b_0/(4\sqrt{m_0 k_0})$, the discriminant is negative, making the real part of the eigenvalues equal to $-\lambda_\ell b_0/(2m_0 N^2)$. The least stable eigenvalue, the one closest to the imaginary axis, is obtained with $\ell = 1$:

$$s_1^{\pm} = -\frac{\pi^2 b_0}{8m_0}\frac{1}{N^2} + \Im \quad \Rightarrow \quad S := |Real(s_1^{\pm})| = \frac{\pi^2 b_0}{8m_0 N^2}, \tag{2–25}$$

where $\Im$ is an imaginary number.

We are now ready to present the proof of Theorem 2.1.

Proof of Theorem 2.1. Recall that in case of symmetric control we have

$$k_i^f = k_i^b, \quad b_i^f = b_i^b, \quad \forall i \in \{1, \cdots, N\}.$$

In this case, using the notation introduced earlier, we have

$$k^{f-b}(x) = 0, \quad b^{f-b}(x) = 0,$$

The PDE (2–8) is simplified to:

$$m(x)\frac{\partial^2 \tilde{p}(x,t)}{\partial t^2} = \frac{k^{f+b}(x)}{2N^2}\frac{\partial^2 \tilde{p}(x,t)}{\partial x^2} + \frac{b^{f+b}(x)}{2N^2}\frac{\partial^3 \tilde{p}(x,t)}{\partial x^2 \partial t}, \tag{2–26}$$

The proof proceeds by a perturbation method. To be consistent with the bounds of the mass and control gains of each vehicle, let

$$\begin{aligned} m(x) &= m_0 + \delta\tilde{m}(x), \quad \tilde{m}(x) \in [-m_0, m_0] \\ k^{f+b}(x) &= 2k_0 + \delta\tilde{k}(x), \quad \tilde{k}(x) \in [-2k_0, 2k_0] \\ b^{f+b}(x) &= 2b_0 + \delta\tilde{b}(x), \quad \tilde{b}(x) \in [-2b_0, 2b_0]. \end{aligned}$$

where δ is a small positive number, denoting the amount of heterogeneity and $\tilde{m}(x), \tilde{k}(x), \tilde{b}(x)$ are the perturbation profiles. Take Laplace transform to both sides of PDE (2–26) with respect to t, we have

$$m(x)s^2\eta = \frac{k^{f+b}(x)}{2N^2}\frac{\partial^2\eta}{\partial x^2} + \frac{b^{f+b}(x)}{2N^2}s\frac{\partial^2\eta}{\partial x^2}, \tag{2–27}$$

Let the perturbed eigenvalue be $s = s_\ell = s_\ell^{(0)} + \delta s_\ell^{(\delta)}$, the Laplace transform of $\tilde{p}(x,t)$ be $\eta = \eta^{(0)} + \delta\eta^{(\delta)}$, where $s_\ell^{(0)}$ and $\eta^{(0)}$ correspond to the unperturbed PDE (2–19), i.e.

$$m_0(s^{(0)})^2\eta^{(0)} = \frac{k_0}{N^2}\frac{\partial^2\eta^{(0)}}{\partial x^2} + \frac{b_0}{N^2}s^{(0)}\frac{\partial^2\eta^{(0)}}{\partial x^2}. \tag{2–28}$$

Eq. (2–24) provides the formula for $s_\ell^{(0)}$ (actually, $s_\ell^{\pm}$), and $\eta^{(0)}$ is the solution to above equation, which is given by $\eta^{(0)} = \sum_{\ell=1}^{\infty}\eta_\ell^{(0)} = \sum_{\ell=1}^{\infty}\phi_\ell(x)H_\ell(s)$, where $H_\ell(s)$ is the Laplace transform of $h(t)$ given in (2–20). Plugging the expressions for s_ℓ and η into (2–27), and doing an $O(1)$ balance leads to the eigenvalue equation for the unperturbed PDE, which is exactly Eq. (2–28):

$$\mathcal{P}\eta^{(0)} = 0, \text{ where } \mathcal{P} := \left(m_0(s_\ell^{(0)})^2 - \frac{b_0 s_\ell^{(0)} + k_0}{N^2}\frac{\partial^2}{\partial x^2}\right) \tag{2–29}$$

Next we do an $O(\delta)$ balance, which leads to:

$$\mathcal{P}\eta^{(\delta)} = \Big(- 2m_0 s_\ell^{(0)} s_\ell^{(\delta)}\eta^{(0)} - \tilde{m}(x)(s_\ell^{(0)})^2\eta^{(0)} + \frac{\tilde{k}(x)}{2N^2}\frac{\partial^2\eta^{(0)}}{\partial x^2} + s_\ell^{(0)}\frac{\tilde{b}(x)}{2N^2}\frac{\partial^2\eta^{(0)}}{\partial x^2} + s_\ell^{(\delta)}\frac{b_0}{N^2}\frac{\partial^2\eta^{(0)}}{\partial x^2}\Big) =: R$$

For a solution $\eta^{(\delta)}$ to exist, R must lie in the range space of the operator $\mathcal{P}$. Since $\mathcal{P}$ is self-adjoint, its range space is orthogonal to its null space. Thus, we have,

$$< R, \eta_\ell^{(0)} >= 0 \tag{2–30}$$

where ϕ_ℓ is also the ℓ^{th} basis vector of the null space of operator $\mathcal{P}$. We now have the following equation:

$$\int_0^1 \Big(-2m_0 s_\ell^{(0)} s_\ell^{(\delta)} \eta^{(0)} - \tilde{m}(x)(s_\ell^{(0)})^2 \eta^{(0)} + \frac{\tilde{k}(x)}{2N^2}\frac{\partial^2 \eta^{(0)}}{\partial x^2} + s_\ell^{(0)}\frac{\tilde{b}(x)}{2N^2}\frac{\partial^2 \eta^{(0)}}{\partial x^2} + s_\ell^{(\delta)}\frac{b_0}{N^2}\frac{\partial^2 \eta^{(0)}}{\partial x^2}\Big)\eta_\ell^{(0)} dx = 0.$$

Following straightforward manipulations, we got:

$$s_\ell^{(\delta)} = \frac{b_0 \lambda_\ell}{m_0^2 N^2}\int_0^1 \tilde{m}(x)(\phi_\ell(x))^2 dx - \frac{\lambda_\ell}{2m_0 N^2}\int_0^1 \tilde{b}(x)(\phi_\ell(x))^2 dx + \Im, \tag{2–31}$$

where $\Im$ is an imaginary number when N is large ($N > (2\ell-1)\pi b_0/(4\sqrt{m_0 k_0})$). Using this, and substituting the equation above into $s_\ell = s_\ell^{(0)} + \delta s_\ell^{(\delta)} + O(\delta^2)$, and setting $\ell = 1$, we obtain the stability margin of the heterogeneous network:

$$S = \frac{b_0\pi^2}{8m_0N^2} - \delta\frac{b_0\pi^2}{4m_0^2N^2}\int_0^1 \tilde{m}(x)\cos^2\big(\frac{\pi}{2}x\big)dx + \delta\frac{\pi^2}{8m_0N^2}\int_0^1 \tilde{b}(x)\cos^2\big(\frac{\pi}{2}x\big)dx + O(\delta^2).$$

Plugging the bounds $|\tilde{m}(x)| \le m_0$ and $|\tilde{b}(x)| \le 2b_0$, we obtain the desired result. □

We now present numerical computations that corroborates the PDE-based analysis. We consider the following mass and control gain profile:

$$\begin{aligned} k_i^f = k_i^b &= 1 + 0.2\sin(2\pi(N-i)/N), \\ b_i^f = b_i^b &= 0.5 + 0.1\sin(2\pi(N-i)/N), \\ m_i &= 1 + 0.2\sin(2\pi(N-i)/N). \end{aligned} \tag{2–32}$$

In the associated PDE model (2–26), this corresponds to $k^f(x) = k^b(x) = 1 + 0.2\sin(2\pi x)$, $b^f(x) = b^b(x) = 0.5 + 0.1\sin(2\pi x)$, $m(x) = 1 + 0.2\sin(2\pi x)$. The eigenvalues of the PDE,

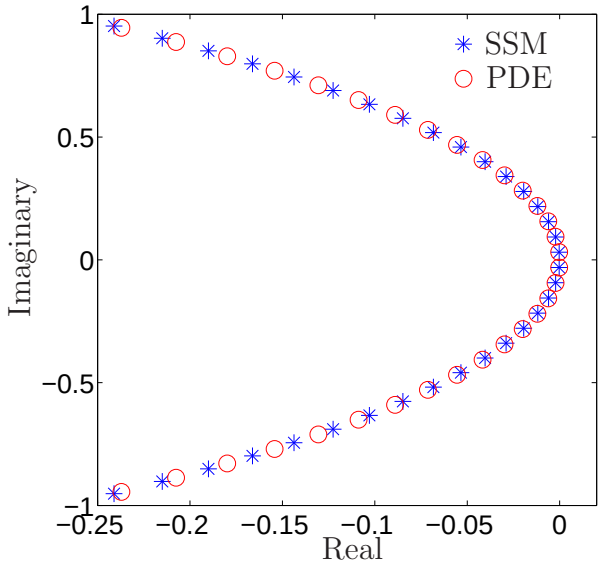

Figure 2-2. Numerical comparison of eigenvalues between state space and PDE models.

that are computed numerically using a Galerkin method with Fourier basis, are compared with that of the state space model to check how well the PDE model captures the closed loop dynamics. Figure 2-2 depicts the comparison of eigenvalues of the state-space model (SSM) (2–7) and the PDE model (2–26) with symmetric control. Eigenvalues shown are for a platoon of 50 vehicles, and the mass and control gains profile are given in (2–32). Only some eigenvalues close to the imaginary axis are compared in the figure. It shows the eigenvalues of the state-space model is accurately approximated by the PDE model, especially the ones close to the imaginary axis. We see from Figure 2-3 that the closed-loop stability margin of the controlled formation is well captured by the PDE model. In addition, the plot corroborates the predicted bound (2–11). The legends of SSM, PDE and lower bound, upper bound stand for the stability margin computed from the state space model, from the PDE model, and the asymptotic lower and upper bounds (2–11) in Theorem 2.1. The mass and control gains profile are given in (2–32).

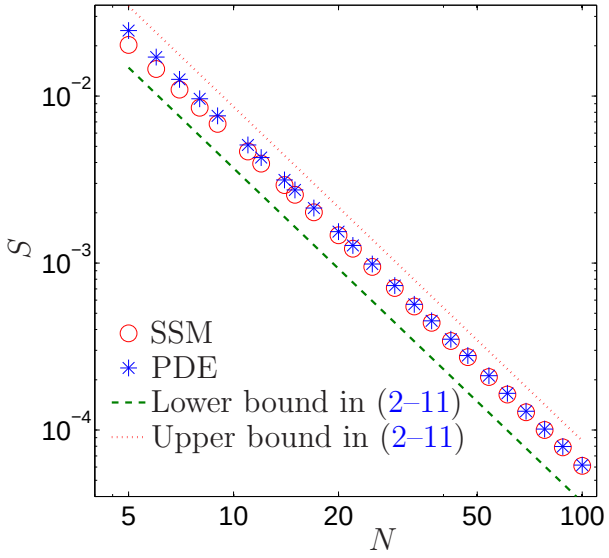

Figure 2-3. Stability margin of the heterogeneous platoon as a function of number of vehicles.

2.4 Role of Asymmetry on Stability Margin

In this section, we consider two scenarios of asymmetric control, we first present the results when there is asymmetry in the velocity feedback alone (Theorem 2.3). The results when there is equal asymmetry in both position and velocity feedbacks (Theorem 2.4).

2.4.1 Asymmetric Velocity Feedback

With symmetric control, one obtains an $O(\frac{1}{N^2})$ scaling law for the stability margin because the coefficient of the $\frac{\partial^3}{\partial x^2 \partial t}$ term in the PDE (2–26) is $O(\frac{1}{N^2})$ and the coefficient of the $\frac{\partial^2}{\partial x \partial t}$ term is 0. Any asymmetry between the forward and the backward velocity gains will lead to non-zero $b^{f-b}(x)$ and a presence of $O(\frac{1}{N})$ term as coefficient of $\frac{\partial^2}{\partial x \partial t}$. By a judicious choice of asymmetry, there is thus a potential to improve the stability margin from $O(\frac{1}{N^2})$ to $O(\frac{1}{N})$. A poor choice of control asymmetry may lead to instability, as we'll show in the sequel.

We begin by considering the forward and backward feedback gain profiles

$$k^f(x) = k^b(x) = k_0, \quad b^f(x) = b_0 + \varepsilon \tilde{b}^f(x), \quad b^b(x) = b_0 + \varepsilon \tilde{b}^b(x), \tag{2–33}$$

where $\varepsilon > 0$ is a small parameter signifying the percent of asymmetry and $\tilde{b}^f(x)$, $\tilde{b}^b(x)$ are functions defined over $[0, 1]$ that capture velocity gain perturbation from the nominal value b_0. Define

$$\tilde{b}^s(x) := \tilde{b}^f(x) + \tilde{b}^b(x), \qquad \tilde{b}^m(x) := \tilde{b}^f(x) - \tilde{b}^b(x). \tag{2–34}$$

Due to the definition of $k^{f+b}, k^{f-b}, b^{f+b}$ and b^{f-b}, we have

$$\begin{aligned} k^{f+b}(x) &= 2k_0, & k^{f-b}(x) &= 0, \\ b^{f+b}(x) &= 2b_0 + \varepsilon\tilde{b}^s(x), & b^{f-b}(x) &= \varepsilon\tilde{b}^m(x). \end{aligned}$$

The PDE (2–8) with homogeneous mass m_0 now becomes

$$m_0\frac{\partial^2\tilde{p}(x,t)}{\partial t^2} = \Big(\frac{k_0}{N^2}\frac{\partial^2}{\partial x^2} + \frac{b_0}{N^2}\frac{\partial^3}{\partial x^2\partial t}\Big)\tilde{p}(x,t) + \varepsilon\Big(\frac{\tilde{b}^s(x)}{2N^2}\frac{\partial^3}{\partial x^2\partial t} + \frac{\tilde{b}^m(x)}{N}\frac{\partial^2}{\partial x\partial t}\Big)\tilde{p}(x,t). \tag{2–35}$$

We now study the problem of how does the choice of the perturbations $\tilde{b}^s(x)$ and $\tilde{b}^m(x)$ (within limits so that the gains $b^f(x)$ and $b^b(x)$ are within pre-specified bounds) affect the stability margin. An answer to this question also helps in designing beneficial perturbations to improve the stability margin. The following result is used in the subsequent analysis.

Proposition 2.1. *Consider the eigenvalue problem of the PDE (2–35) with mixed Dirichlet and Neumann boundary condition (2–9). The least stable eigenvalue is given by the following formula that is valid for $\varepsilon \ll 1$ and large N:*

$$s_1 = s_1^{(0)} - \varepsilon\frac{\pi}{4m_0N}\int_0^1 \tilde{b}^m(x)\sin(\pi x)\,dx - \varepsilon\frac{\pi^2}{8m_0N^2}\int_0^1 \tilde{b}^s(x)\cos^2\Big(\frac{\pi}{2}x\Big)\,dx + O(\varepsilon^2) + \Im \tag{2–36}$$

where $s_1^{(0)}$ is the least stable eigenvalue of the unperturbed PDE (2–19) with the same boundary conditions and $\Im$ is an imaginary number when N is large ($N > \pi b_0/(4\sqrt{m_0k_0})$).

□

The proof of Proposition 2.1 is similar to the proof of Theorem 2.1. It is given in the Appendix. Now we are ready to prove Theorem 2.3.

Proof of Theorem 2.3. It follows from Proposition 2.1 that to minimize the least stable eigenvalue, one needs to choose only $\tilde{b}^m(x)$ carefully. The reason is the second term involving $\tilde{b}^s(x)$ has the $O(1/N^2)$ trend. Therefore, we choose

$$\tilde{b}^s(x) \equiv 0.$$

This means that the perturbations to the "front" and "back" velocity gains satisfy:

$$\tilde{b}^f(x) = -\tilde{b}^b(x) \qquad \Leftrightarrow \qquad \tilde{b}^m(x) = 2\tilde{b}^f(x).$$

The most beneficial gains can now be readily obtained from Proposition 2.1. To minimize the least stable eigenvalue with $\tilde{b}^s(x) \equiv 0$, we should choose $\tilde{b}^m(x)$ to make the integral $\int_0^1 \tilde{b}^m(x)\sin(\pi x)dx$ as large as possible, which is achieved by setting $\tilde{b}^m(x)$ to be the largest possible value everywhere in the interval $[0,1]$. The constraint $|b_i^{(\cdot)} - b_0|/b_0 \leq \varepsilon$ translates to $b_0(1-\varepsilon) \leq b^{(\cdot)}(x) \leq b_0(1+\varepsilon)$, which means $\|\tilde{b}^f\|_\infty \leq b_0$ and $\|\tilde{b}^b\|_\infty \leq b_0$. With the choice of $\tilde{b}^s$ made above, we therefore have the constraint $\|\tilde{b}^m\| \leq 2b_0$. The solution to the optimization problem is therefore obtained by choosing $\tilde{b}^m(x) = 2b_0 \ \forall x \in [0,1]$. This gives us the optimal gains

$$\tilde{b}^f(x) = b_0, \quad \tilde{b}^b(x) = -b_0, \quad \Rightarrow \quad b^f(x) = b_0(1+\varepsilon), \quad b^b(x) = b_0(1-\varepsilon).$$

The least stable eigenvalue is obtained from Proposition (2.1):

$$s_1^+ = s^{(0)} - \frac{\varepsilon b_0}{m_0 N} - 0 + O(\varepsilon^2) + \Im.$$

Since $s^{(0)}$ is the least stable eigenvalue for the symmetric PDE, we know from Theorem 2.1 that $s^{(0)} = O(1/N^2)$. Therefore, it follows from the equation above that the stability margin is $S = Re(s_1^+) = \frac{\varepsilon b_0}{m_0 N} + O(\frac{1}{N^2})$. This proves the first statement of the theorem.

To prove the second statement, the control gain design $b_i^f = (1-\varepsilon)b_0$ and $b_i^b = (1+\varepsilon)b_0$ becomes $b^f(x) = (1-\varepsilon)b_0$ and $b^b(x) = (1+\varepsilon)b_0$. With this choice, it follows from Proposition (2.1) that

$$s_1^+ = s^{(0)} + \frac{\varepsilon b_0}{m_0 N} - 0 + O(\varepsilon^2) + \Im.$$

Since $s^{(0)} = O(1/N^2)$, the second term, which is $O(1/N)$, will dominate for large N. Since this term is positive, the second statement is proved. □

2.4.2 Asymmetric Position and Velocity Feedback with Equal Asymmetry

When there is equal asymmetry in the position and velocity feedback, we consider the following homogeneous and asymmetric control gains:

$$\begin{aligned} k^f(x) &= (1+\varepsilon)k_0, & k^b(x) &= (1-\varepsilon)k_0, \\ b^f(x) &= (1+\varepsilon)b_0, & b^b(x) &= (1-\varepsilon)b_0, \end{aligned} \tag{2–37}$$

where ε is the amount of asymmetry satisfying $\varepsilon \in (0,1)$.

Proof of Theorem 2.4. The PDE model with the control gains specified in (2–37) becomes

$$m_0 \frac{\partial^2 \tilde{p}(x,t)}{\partial t^2} = \frac{2\varepsilon k_0}{N}\frac{\partial \tilde{p}(x,t)}{\partial x} + \frac{k_0}{N^2}\frac{\partial^2 \tilde{p}(x,t)}{\partial x^2} + \frac{2\varepsilon b_0}{N}\frac{\partial^2 \tilde{p}(x,t)}{\partial x \partial t} + \frac{b_0}{N^2}\frac{\partial^3 \tilde{p}(x,t)}{\partial x^2 \partial t}, \tag{2–38}$$

By the method of separation of variables, we assume a solution of the form $\tilde{p}(x,t) = \sum_{\ell=1}^{\infty} \phi_\ell(x) h_\ell(t)$. Substituting it into PDE (2–38), we obtain the following time-domain ODE

$$m_0 \frac{d^2 h_\ell(t)}{dt^2} + b_0 \lambda_\ell \frac{dh_\ell(t)}{dt} + k_0 \lambda_\ell h_\ell(t) = 0, \tag{2–39}$$

where λ_ℓ solves the following boundary value problem

$$\mathcal{L}\phi_\ell(x) = 0, \quad \mathcal{L} := \frac{d^2}{dx^2} + 2\varepsilon N \frac{d}{dx} + \lambda_\ell N^2, \tag{2–40}$$

with the following boundary condition, which comes from (2–9):

$$\frac{d\phi_\ell}{dx}(0) = 0, \quad \phi_\ell(1) = 0. \tag{2–41}$$

Taking Laplace transform of both sides of (2–39) with respect to the time variable t, we have the following characteristic equation for the PDE model

$$m_0 s^2 + b_0 \lambda_\ell s + k_0 \lambda_\ell = 0. \tag{2–42}$$

We now solve the boundary value problem (2–40)-(2–41). We multiply both sides of (2–40) by $e^{2\varepsilon N x} N^2$ to obtain the standard Sturm-Liouville eigenvalue problem

$$\frac{d}{dx}\left(e^{2\varepsilon N x}\frac{d\phi_\ell(x)}{dx}\right) + \lambda_\ell^{(\varepsilon)} N^2 e^{2\varepsilon N x}\phi_\ell(x) = 0. \tag{2–43}$$

According to Sturm-Liouville Theory, all the eigenvalues are real and have the following ordering $\lambda_1 < \lambda_2 < \cdots$, see [77]. To solve the boundary value problem (2–40)-(2–41), we assume solution of the form, $\phi_\ell(x) = e^{rx}$, then we obtain the following equation

$$r^2 + 2\varepsilon N r + \lambda_\ell N^2 = 0, \quad \Rightarrow \quad r = -\varepsilon N \pm N\sqrt{\varepsilon^2 - \lambda_\ell}. \tag{2–44}$$

Depending on the discriminant in the above equation, there are three cases to analyze:

- $\lambda_\ell < \varepsilon^2$, the eigenfunction has the following form

  $$\phi_\ell(x) = c_1 e^{(-\varepsilon N + N\sqrt{\varepsilon^2-\lambda_\ell})x} + c_2 e^{(-\varepsilon N - N\sqrt{\varepsilon^2-\lambda_\ell})x}.$$

  where c_1, c_2 are some constants. Applying the boundary condition (2–41), it's straightforward to see that, for non-trivial eigenfunctions $\phi_\ell(x)$ to exit, the following equation must be satisfied $(\varepsilon N - N\sqrt{\varepsilon^2 - \lambda_\ell})/(\varepsilon N + N\sqrt{\varepsilon^2 - \lambda_\ell}) = e^{2N\sqrt{\varepsilon^2-\lambda_\ell}}$. For positive ε, this leads to a contradiction, so there is no eigenvalue for this case.
- $\lambda_\ell = \varepsilon^2$, the eigenfunction $\phi_\ell(x)$ has the following form

  $$\phi_\ell(x) = c_1 e^{-\varepsilon N x} + c_2 x e^{-\varepsilon N x}.$$

Again, applying the boundary condition (2–41), for non-trivial eigenfunctions $\phi_\ell(x)$ to exit, we have the following $\varepsilon N = -1$, which implies there is no eigenvalue for this case either.

- $\lambda_\ell > \varepsilon^2$, the eigenfunction has the following form

$$\phi_\ell(x) = e^{-\varepsilon N x}(c_1 \cos(N\sqrt{\lambda_\ell - \varepsilon^2}x) + c_2 \sin(N\sqrt{\lambda_\ell - \varepsilon^2}x)).$$

Applying the boundary condition (2–41), for non-trivial eigenfunctions $\phi_\ell(x)$ to exit, the eigenvalues λ_ℓ must satisfy $\lambda_\ell = \varepsilon^2 + \frac{a_\ell^2}{N^2}$ where a_ℓ solves the transcendental equation $-a_\ell/(\varepsilon N) = \tan(a_\ell)$. A graphical representation of the functions $\tan x$ and $-x/\varepsilon N$ with respect to x shows that $a_\ell \in (\frac{(2\ell-1)\pi}{2}, \ell\pi)$.

From the last case, we see that $a_1 \in (\pi/2, \pi)$, and $\lambda_1 \to \varepsilon^2$ from above as $N \to \infty$, i.e. $\inf_N \lambda_1 = \varepsilon^2$. For each $\ell \in \{1, 2, \cdots\}$, the two roots of the characteristic equations (2–42) are given by

$$s_\ell^\pm = \frac{-b_0\lambda_\ell \pm \sqrt{b_0^2\lambda_\ell^2 - 4m_0k_0\lambda_\ell}}{2m_0}. \tag{2–45}$$

Depending on the discriminant in (2–45), there are two cases to analyze:

- If $\lambda_1 \geq 4m_0k_0/b_0^2$, then the discriminant in (2–45) for each ℓ is non-negative, the *less stable* eigenvalue can be written as

$$s_\ell^+ = -\frac{\lambda_\ell b_0 - \sqrt{(\lambda_\ell b_0)^2 - 4\lambda_\ell m_0 k_0}}{2m_0} = -\frac{2k_0}{b_0 + \sqrt{b_0^2 - 4m_0k_0/\lambda_\ell}}.$$

The least stable eigenvalue is achieved by setting $\lambda_\ell = \lambda_\infty$. Since $\lambda_\ell \to \infty$ as $\ell \to \infty$, we have the stability margin

$$S = |Re(s_1^+)| \geq \frac{2k_0}{b_0 + \sqrt{b_0^2 - 0}} = \frac{k_0}{b_0}.$$

- Otherwise, the discriminant in (2–45) is indeterministic, i.e. it's negative for small ℓ and positive for large ℓ is non-positive. For those ℓ's which make the discriminant

negative, the least stable eigenvalue among them is given by

$$s_1^{\pm} = -\frac{\lambda_1 b_0}{2m_0} + \Im.$$

where $\Im$ is an imaginary number. For those ℓ's which make the discriminant non-positive, we have from the first case that the least stable eigenvalue among them is given by

$$s_1^{+} = -\frac{2k_0}{b_0 + \sqrt{b_0^2 - 4m_0 k_0/\lambda_\infty}}$$

The stability margin is given by taking the minimum of absolute value of the real part of the above two eigenvalues,

$$S \geq \min\left\{\frac{b_0\lambda_1}{2m_0}, \frac{k_0}{b_0}\right\}.$$

Combining the above two cases, and using the fact that $\lambda_1 \geq \varepsilon^2$, we obtain that the stability margin can be bounded below as follows

$$S \geq \min\left\{\frac{b_0\varepsilon^2}{2m_0}, \frac{k_0}{b_0}\right\}.$$

This concludes the proof. □

2.4.3 Numerical Comparison of Stability Margin

Figure 2-4 depicts the numerically obtained stability margins for both the PDE and state-space models (SSM) with symmetric and asymmetric control gains. The mass of each vehicle used is $m_0 = 1$. The nominal control gains are $k_0 = 1$, $b_0 = 0.5$. The asymmetric control gains used are the ones given in Theorem 2.3 and Theorem 2.4 respectively, and the amount of asymmetry is $\varepsilon = 0.1$. The legends "SSM" and "PDE" stand for the stability margin computed from the state-space model and the PDE model, respectively. The figure shows that 1) the stability margin of the PDE model matches that of the state-space model accurately, even for small values of N; 2) the stability

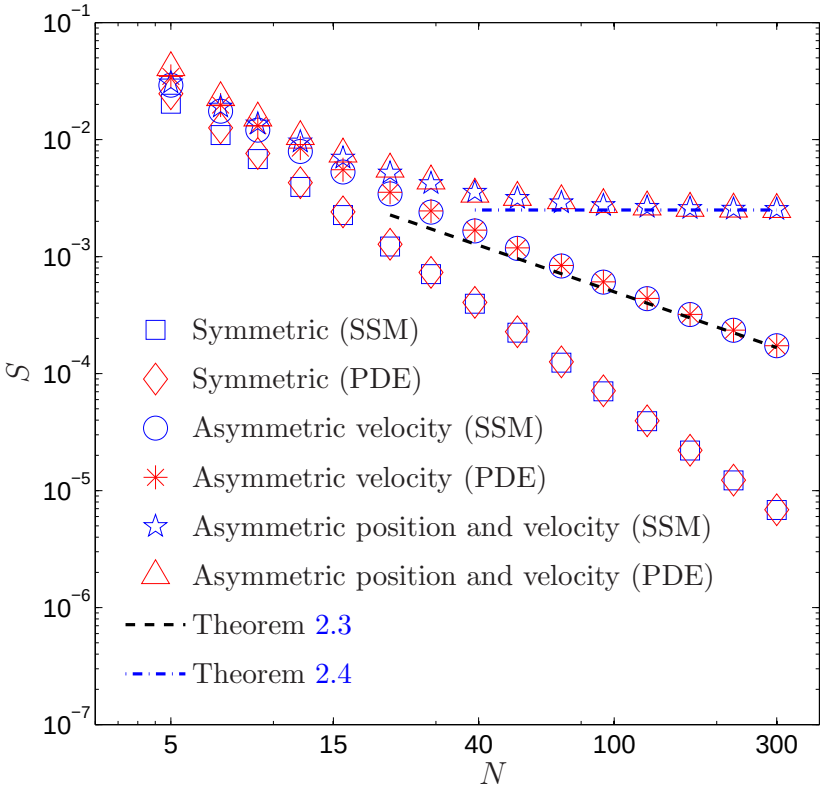

Figure 2-4. Stability margin improvement by asymmetric control.

margin with asymmetric velocity feedback shows large improvement over the symmetric case even though the velocity gains differ from their nominal values only by $\pm 10\%$. The improvement is particularly noticeable for large values of N; 3) With equal amount of asymmetry in both the position and velocity feedback, the stability margin can be uniformly bounded away from 0, which eliminates the degradation of stability margin with increasing N; 4) the asymptotic formulae given in Theorem 2.3 and Theorem 2.4 are quire accurate.

Numerical validation that poor choice of asymmetry in control gains can lead to instability is shown in Figure 2-5. The mass of each vehicle is $m_0 = 1$. The nominal control gains are $k_0 = 1$, $b_0 = 0.5$, and the control gains used are the ones given by (2–14)

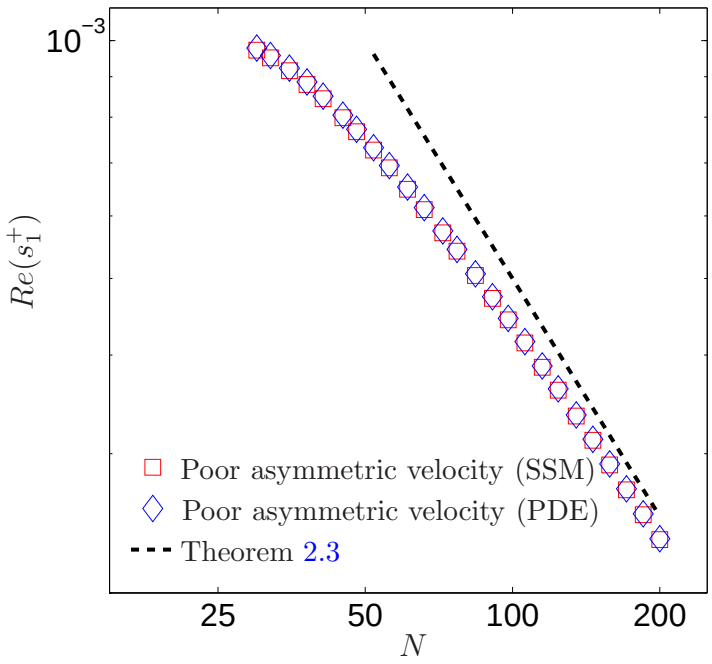

Figure 2-5. The real part of the most unstable eigenvalues with poor asymmetry.

in Theorem 2.3 with $\varepsilon = 0.1$. Note that the real part of these eigenvalues are positive and Eq. (2–14) also makes an accurate prediction.

2.5 Scaling of Stability Margin with both Asymmetry and Heterogeneity

In this section, we study the stability margin of the system with both heterogeneity and asymmetry. The main job of this section is to prove Theorem 2.5.

Proof of Theorem 2.5. The proof also relies on perturbation technique. Based on the bounds of the control gains and the definition of $k^{f+b}, k^{f-b}, b^{f+b}$ and b^{f-b}, we have

$$k^{f-b}(x) = 0, \quad k^{f+b}(x) = 2k_0 + \varepsilon\tilde{k}(x), \quad \tilde{k}(x) \in [-2k_0, 2k_0]$$
$$b^{f+b}(x) = 2\varepsilon b_0, \quad b^{f+b}(x) = 2b_0 + \varepsilon\tilde{b}(x), \quad \tilde{b}(x) \in [-2b_0, 2b_0].$$

The PDE (2–8) with homogeneous mass m_0 now becomes

$$\begin{aligned} m_0\frac{\partial^2\tilde{p}(x,t)}{\partial t^2} &= \Big(\frac{k_0}{N^2}\frac{\partial^2}{\partial x^2} + \frac{b_0}{N^2}\frac{\partial^3}{\partial x^2\partial t}\Big)\tilde{p}(x,t) \\ &\quad + \varepsilon\Big(\frac{\tilde{k}(x)}{2N^2}\frac{\partial^2}{\partial x^2} + \frac{\tilde{b}(x)}{2N^2}\frac{\partial^3}{\partial x^2\partial t} + \frac{2b_0}{N}\frac{\partial^2}{\partial x\partial t}\Big)\tilde{p}(x,t). \end{aligned} \tag{2–46}$$

Let the eigenvalues and Laplace transformation of $\tilde{p}(x,t)$ for the above perturbed PDE be $s_\ell = s_\ell^{(0)} + \varepsilon s_\ell^{(\varepsilon)}, \eta = \eta^{(0)} + \varepsilon\eta^{(\varepsilon)}$ respectively, where $s_\ell^{(0)}$ and $\eta^{(0)}$ are corresponding to the unperturbed PDE (2–19). Taking a Laplace transform of PDE (2–46), plugging in the expressions for s_ℓ and η, and doing an $O(\varepsilon)$ balance, which leads to:

$$\mathcal{P}\eta^{(\varepsilon)} = \frac{\tilde{k}(x)}{2N^2}\frac{d^2\eta^{(0)}}{dx^2} + s_\ell^{(0)}\frac{2b_0}{N}\frac{d\eta^{(0)}}{dx} + s_\ell^{(0)}\frac{\tilde{b}(x)}{2N^2}\frac{d^2\eta^{(0)}}{dx^2} - 2m_0 s_\ell^{(0)} s_\ell^{(\varepsilon)}\eta^{(0)} + s_\ell^{(\varepsilon)}\frac{b_0}{N^2}\frac{d^2\eta^{(0)}}{dx^2} =: R,$$

where $\mathcal{P}$ is defined in (2–29). For a solution $\eta^{(\varepsilon)}$ to exist, R must lie in the range space of the self-adjoint operator $\mathcal{P}$. Thus, we have,

$$< R, \eta_\ell^{(0)} >= 0$$

We now have the following equation:

$$\int_0^1 \Big(\frac{\tilde{k}(x)}{2N^2}\frac{d^2\eta^{(0)}}{dx^2} + s_\ell^{(0)}\frac{2b_0}{N}\frac{d\eta^{(0)}}{dx} + s_\ell^{(0)}\frac{\tilde{b}(x)}{2N^2}\frac{d^2\eta^{(0)}}{dx^2} - 2m_0 s_\ell^{(0)} s_\ell^{(\varepsilon)}\eta^{(0)} + s_\ell^{(\varepsilon)}\frac{b_0}{N^2}\frac{d^2\eta^{(0)}}{dx^2}\Big)\eta_\ell^{(0)} dx = 0$$

Straightforward manipulations show that:

$$\begin{aligned} m_0(s_\ell^{(0)} + \frac{b_0\lambda_\ell}{2m_0N^2})s_\ell^{(\varepsilon)} = &- s_\ell^{(0)}\frac{(2\ell-1)\pi}{2N}\int_0^1 b_0 \sin\big((2\ell-1)\pi x\big)\, dx \\ &- s_\ell^{(0)}\frac{(2\ell-1)^2\pi^2}{8N^2}\int_0^1 \tilde{b}(x)\cos^2\big(\frac{(2\ell-1)\pi}{2}x\big)\, dx \\ &- \frac{(2\ell-1)^2\pi^2}{8N^2}\int_0^1 \tilde{k}(x)\cos^2\big(\frac{(2\ell-1)\pi}{2}x\big)\, dx. \end{aligned}$$

Notice that the existence of the last two terms in the RHS of the above equation is due to heterogeneity in the control gains, and their coefficients are orders of $1/N^2$. In addition, the first term which results from asymmetry has coefficient of order $1/N$, which dominates the terms with order $1/N^2$ for large N. Hence heterogeneity in control gains does not change the scaling trend of stability margin, but only introducing asymmetry does. The rest of the proof for the first part of Theorem 2.5 follows by substituting the equation above into $s_\ell = s_\ell^{(0)} + \varepsilon s_\ell^{(\varepsilon)}$, and setting $\ell = 1$.

The proof for the second part of Theorem 2.5 is similar to the argument shown above, we therefore ignore the proof. □

2.6 Summary

We studied the role of heterogeneity and control asymmetry on the stability margin of a large 1-D network of double-integrator vehicles. The control is in a distributed sense that the control signal at every vehicle depends on the relative position and velocity measurements from its two nearest neighbors (one one either side). It was shown that heterogeneity had little effect on how the stability margin scaled with N, the number of vehicles, whereas asymmetry played a significant role. If front-back asymmetry is introduced in the control gains, even by an arbitrarily small amount, the stability margin can be improved to $O(1/N)$ with asymmetric velocity feedback. The stability margin can be even improved to $O(1)$ if there is equal amount of asymmetry in the position and velocity feedback. Additionally, we showed that no matter the control was symmetric or not, vehicle-to-vehicle heterogeneity did not change the scaling of stability margin. Therefore, in terms of stability margin, the asymmetric control with equal asymmetry scheme provides a best way to achieve the goal of larger stability margin. The scenarios with unequal asymmetry in position and velocity feedback and asymmetric position feedbacks are open problems.

2.7 Technical Proofs

2.7.1 Proof of Theorem 2.2

With the profiles and control gains given in Theorem 2.2, the PDE (2–8) simplifies to:

$$m(x)\frac{\partial^2 \tilde{p}(x,t)}{\partial t^2} = \frac{\rho b(x)}{N^2}\frac{\partial^2 \tilde{p}(x,t)}{\partial x^2} + \frac{b(x)}{N^2}\frac{\partial^3 \tilde{p}(x,t)}{\partial x^2 \partial t}, \tag{2–47}$$

where $m_{\min} \leq m(x) \leq m_{\max}, b_{\min} \leq b(x) \leq b_{\max}$. Due to the linearity and homogeneity of the above PDE and boundary conditions, we are able to apply the method of separation of variables. We assume solution of the form $\tilde{p}(x,t) = \sum_{\ell=1}^{\infty} \phi_\ell(x) h_\ell(t)$. Substituting the

solution into (2–47) and dividing both sides by $\phi_\ell(x)h_\ell(s)$, we obtain:

$$\frac{\frac{d^2h_\ell(t)}{dt^2}}{\frac{\rho}{N^2}h_\ell(t)+\frac{1}{N^2}h(t)} = \frac{\frac{d^2\phi_\ell(x)}{dx^2}}{m(x)\phi_\ell(x)/b(x)} \tag{2–48}$$

Since each side of the above equation is independent from the other, so it's necessary for both sides equal to the same constant $-\lambda_\ell$. Then we have two separate equations:

$$\frac{d^2h_\ell(t)}{dt^2}+\frac{\lambda_\ell}{N^2}\frac{dh_\ell(t)}{dt}+\frac{\rho\lambda_\ell}{N^2}h_\ell(t)=0, \tag{2–49}$$

$$\frac{d^2\phi_\ell(x)}{dx^2}+\lambda_\ell\frac{m(x)}{b(x)}\phi(x)=0. \tag{2–50}$$

The spatial part solves the following regular Sturm-Liouville eigenvalue problem

$$\begin{aligned}\frac{d^2\phi_\ell(x)}{dx^2}+\lambda_\ell\frac{m(x)}{b(x)}\phi(x)=0,\\ \frac{d\phi(0)}{dx}=\phi(1)=0.\end{aligned} \tag{2–51}$$

The Rayleigh quotient is given by

$$\lambda_\ell=\frac{\int_0^1(d\phi(x)/dx)^2dx}{\int_0^1\phi^2(x)m(x)/b(x)dx}. \tag{2–52}$$

Since $m_{\min}\le m(x)\le m_{\max}, b_{\min}\le b(x)\le b_{\max}$, we have that $\frac{m_{\min}}{b_{\max}}\le m(x)/b(x)\le\frac{m_{\max}}{b_{\min}}$. Plugging the lower and upper bounds for $m(x)/b(s)$, we have the following relation:

$$\frac{b_{\min}}{m_{\max}}\frac{\int_0^1(d\phi(x)/dx)^2dx}{\int_0^1\phi^2(x)dx}\le\lambda_\ell\le\frac{b_{\max}}{m_{\min}}\frac{\int_0^1(d\phi(x)/dx)^2dx}{\int_0^1\phi^2(x)dx}$$

Since we know the eigenvalue $\bar{\lambda}_\ell$ corresponding to Rayleigh quotient $\frac{\int_0^1(d\phi(x)/dx)^2dx}{\int_0^1\phi^2(x)dx}$ is the eigenvalue obtained from (2–51) with $m(x)/b(x)=1$. And $\bar{\lambda}_\ell$ is given by

$$\bar{\lambda}_\ell=\frac{(2\ell-1)^2\pi^2}{4} \tag{2–53}$$

where ℓ is the wave number, $\ell=1,2,\cdots$.

It is straight forward to see that the least eigenvalue $\bar{\lambda}_\ell$ is obtain by setting $\ell = 1$, i.e. $\bar{\lambda}_1 = \pi^2/4$. So we have the following bounds for the least eigenvalue of λ_ℓ.

$$\frac{b_{\min}\pi^2}{4m_{\max}} \leq \lambda_1 \leq \frac{b_{\max}\pi^2}{4m_{\min}} \tag{2–54}$$

Take Laplace transform to both sides of (2–50), we obtain the following characteristic equation for the PDE model (2–47).

$$s^2 + \frac{\lambda_\ell}{N^2}s + \frac{\rho\lambda_\ell}{N^2} = 0.$$

Its eigenvalues turn out to be the roots of the above equation,

$$s_\ell^{\pm} := \frac{-\lambda_\ell/N^2 \pm \sqrt{\lambda_\ell^2/N^4 - 4\rho\lambda_\ell/N^2}}{2}. \tag{2–55}$$

We call $s_\ell^{\pm}$ the ℓ-th pair of eigenvalues. The discriminant D in (2–55) is given by:

$$D := \lambda_\ell^2/N^4 - 4\rho\lambda_\ell/N^2.$$

For large N and small ℓ, D is negative. So both the eigenvalues in (2–55) are complex, then the stability margin is only determined by the real parts of $s_\ell^{\pm}$. It follows from (2–55) that the least stable eigenvalue (the ones closest to the imaginary axis) among them is the one that is obtained by minimizing λ_ℓ over ℓ. Then, this minimum is achieved at $\ell = 1$, and the real part is obtained

$$Real(s_1^{\pm}) = -\frac{\lambda_1}{2N^2}.$$

Following the definition of stability margin $S := |Real(s_1^{\pm})|$ as well as the bounds for λ_1 given by (2–54), we complete the proof. □

2.7.2 Proof of Proposition 2.1

The proof proceeds by a perturbation method. Let the eigenvalues and Laplace transformation of $\tilde{p}(x,t)$ for the perturbed PDE (2–35) be $s_\ell = s_\ell^{(0)} + \varepsilon s_\ell^{(\varepsilon)}, \eta = \eta^{(0)} + \varepsilon\eta^{(\varepsilon)}$ respectively, where $s_\ell^{(0)}$ and $\eta^{(0)}$ are corresponding to the unperturbed PDE (2–19). Taking

a Laplace transform of PDE (2–35), plugging in the expressions for s_ℓ and η, and doing an $O(\varepsilon)$ balance, which leads to:

$$\mathcal{P}\eta^{(\varepsilon)} = s_\ell^{(0)}\frac{\tilde{b}^m(x)}{N}\frac{d\eta^{(0)}}{dx} + s_\ell^{(0)}\frac{\tilde{b}^s(x)}{2N^2}\frac{d^2\eta^{(0)}}{dx^2} - 2m_0 s_\ell^{(0)} s_\ell^{(\varepsilon)}\eta^{(0)} + s_\ell^{(\varepsilon)}\frac{b_0}{N^2}\frac{d^2\eta^{(0)}}{dx^2} =: R,$$

where $\mathcal{P}$ is defined in (2–29). For a solution $\eta^{(\varepsilon)}$ to exist, R must lie in the range space of the self-adjoint operator $\mathcal{P}$. Thus, we have,

$$< R, \eta_\ell^{(0)} >= 0$$

We now have the following equation:

$$\int_0^1 \Big(s_\ell^{(0)}\frac{\tilde{b}^m(x)}{N}\frac{d\eta^{(0)}}{dx} + s_\ell^{(0)}\frac{\tilde{b}^s(x)}{2N^2}\frac{d^2\eta^{(0)}}{dx^2} - 2m_0 s_\ell^{(0)} s_\ell^{(\varepsilon)}\eta^{(0)} + s_\ell^{(\varepsilon)}\frac{b_0}{N^2}\frac{d^2\eta^{(0)}}{dx^2}\Big)\eta_\ell^{(0)} dx = 0$$

Straightforward manipulations show that:

$$\begin{aligned} m_0(s_\ell^{(0)} + \frac{b_0\lambda_\ell}{2m_0N^2})s_\ell^{(\varepsilon)} = &- s_\ell^{(0)}\frac{(2\ell-1)\pi}{4N}\int_0^1 \tilde{b}^m(x)\sin\big((2\ell-1)\pi x\big)\,dx \\ &- s_\ell^{(0)}\frac{(2\ell-1)^2\pi^2}{8N^2}\int_0^1 \tilde{b}^s(x)\cos^2\big(\frac{(2\ell-1)\pi}{2}x\big)\,dx. \end{aligned} \tag{2–56}$$

Substituting the equation above into $s_\ell = s_\ell^{(0)} + \varepsilon s_\ell^{(\varepsilon)}$, and setting $\ell = 1$, we complete the proof. □

CHAPTER 3
ROBUSTNESS TO EXTERNAL DISTURBANCES OF 1-D VEHICULAR PLATOON

In this chapter we study the robustness to external disturbances of a large 1-D platoon of vehicles with distributed control. We consider the robustness to external disturbances for two decentralized control architectures: *predecessor-following* and *bidirectional*. It has been known for quite some time that the predecessor-following architecture has extremely poor robustness to external disturbances [45, 46]. In was shown that string instability with the predecessor-following architecture is independent of the design of the controller on each vehicle, but a fundamental artifact of the architecture [31]. The high sensitivity to disturbance of predecessor-following architecture led to the examination of the bidirectional architecture. Most works focus on symmetric bidirectional architecture. The symmetry assumption significantly simplified analysis. It was shown that symmetric bidirectional architectures also suffers from poor robustness to external disturbances [31, 52, 67].

Although a rich literature exists on sensitivity to disturbances with predecessor-following and symmetric bidirectional architectures, to the best of our knowledge, a precise comparison of the performance of these two architectures - in terms of quantitative measures of robustness is lacking. This chapter addresses exactly this problem. In particular, we establish how certain H_∞ norms, that quantifies the system's robustness, scale with the size of the platoon for each of these two architectures. We study two scenarios to quantify robustness. First, we study the effect of disturbance acting on the leader on the tracking error of the last vehicle. Second, we study the effect of disturbances acting on all the vehicles in the platoon (except the leader) on their tracking errors. Correspondingly, two kinds of performance metrics are used to quantify the robustness: i) the *leader-to-trailer amplification*, which is defined as the H_∞ norm of the transfer function from the disturbance on the leader to the position tracking error of the last

vehicle; ii) the *all-to-all amplification*, which is defined as the H_∞ norm of the transfer function from the disturbances on all the followers to their position tracking errors.

For the predecessor-following architecture, it is well known that the leader-to-trailer amplification grows geometrically and the all-to-all amplification can not be bounded above uniformly in N, the number of vehicles in the platoon [31, 53]. In this chapter, we show that they are both $O(\alpha^N)$ for some $\alpha > 1$. Thus, as the size of the platoon increases, the amplification of disturbance increases geometrically. We then show that with symmetric bidirectional architecture, the leader-to-trailer amplification is $O(N)$, whereas the all-to-all amplification is $O(N^3)$. In addition, the resonance frequencies in both cases are $O(1/N)$ [53]. Thus, among the two control architectures, the symmetric bidirectional architecture performs far better than the predecessor-following architecture in terms of sensitivity to disturbance, especially as the platoon size becomes large.

The analysis for the symmetric bidirectional architecture is carried out with a PDE approximation of the closed-loop dynamics, which is derived in the previous chapter. The asymptotic formulae for the two amplification factors mentioned above and the resonance frequencies are obtained using a PDE-based analysis. Numerical computations of the coupled-ODE model are provided to verify the analysis of the corresponding PDE model. Although the PDE is derived under the assumption that N is large, numerical results show that it makes an accurate approximation even when N is small (e.g. $N = 10$).

We assume each vehicle has a double-integrator dynamics and the platoon is homogeneous: each vehicle in the platoon has the same open-loop dynamics and uses the same control law. The assumption of double-integrator dynamics comes from the fact that single-integrator models fail to reproduce the slinky-type effects or string instability [3] and higher order dynamics will result in instability for sufficient large N [52, 53]. In addition, heterogeneity in vehicle mass and control gains has little effect on the stability margin and sensitivity to disturbance of the platoon [62, 67, 84]. However, we show by numerical simulation that asymmetry has a substantial effect on the robustness of the 1-D

platoon. Judicious asymmetry in the control gains can improve the robustness of the 1-D platoon considerably over symmetric control.

The rest of this chapter is organized as follows. Section 3.1 presents the problem statement. Section 3.2 describes the PDE model of the 1-D platoon of double-integrator vehicles with symmetric bidirectional architecture. Analysis of the H_∞ norms of the system for both symmetric bidirectional and predecessor-following architectures as well as the conjecture for asymmetric bidirectional architecture and their numerical verifications appear in Section 3.3. The chapter ends with a summary in Section 3.4.

3.1 Problem Formulation

We consider the formation control of $N+1$ homogeneous vehicles (1 leader and N followers) which are moving in 1-D Euclidean space, as shown in Figure 2-1 (a). The position of the i-th vehicle is denoted by $p_i \in \mathbb{R}$. The dynamics of each vehicle are modeled as a double integrator:

$$m_i \ddot{p}_i = u_i + w_i, \quad i \in \{1, 2, \cdots, N\}, \tag{3–1}$$

where m_i is the mass, u_i is the control input and w_i is the external disturbance on the i-th vehicle. The disturbance on each vehicle is assumed to be $w_i = a_i \sin(\omega t + \theta_i)$. This is a commonly used model for vehicle dynamics in studying vehicular formations, and results from feedback linearization of non-linear vehicle dynamics [3, 39, 49].

The control objective is that vehicles maintain a rigid formation geometry while following a constant-velocity type desired trajectory. The desired geometry of the formation is specified by constant desired inter-vehicle spacing $\Delta_{(i-1,i)}$ for $i \in \{1, \cdots, N\}$, where $\Delta_{(i-1,i)}$ is the desired value of $p_{i-1}(t) - p_i(t)$. Each vehicle i knows the desired gaps $\Delta_{(i-1,i)}$, $\Delta_{(i,i+1)}$. The desired trajectory of the platoon is specified in terms of a leader whose dynamics are independent of the other vehicles. The leader is indexed by 0, and its trajectory is denoted by $p_0^*(t) = vt + \Delta_{(0,N)}$, where v is a positive constant, which is the cruise velocity of the platoon. The desired trajectory of the i-th vehicle, $p_i^*(t)$, is given by

$p_i^*(t) = p_0^*(t) - \Delta_{(0,i)} = p_0^*(t) - \sum_{j=1}^{i} \Delta_{(j-1,j)}$. To facilitate analysis, we define the tracking error:

$$\tilde{p}_i := p_i - p_i^* \qquad \Rightarrow \qquad \dot{\tilde{p}}_i = \dot{p}_i - \dot{p}_i^*. \tag{3–2}$$

We consider the following decentralized control law, where the control on the i-th vehicle depends on the relative position and velocity measurements from its immediate predecessor and possibly its immediate follower:

$$\begin{aligned} u_i =& - k_i^f(\tilde{p}_i - \tilde{p}_{i-1}) - k_i^b(\tilde{p}_i - \tilde{p}_{i+1}) - b_i^f(\dot{\tilde{p}}_i - \dot{\tilde{p}}_{i-1}) - b_i^b(\dot{\tilde{p}}_i - \dot{\tilde{p}}_{i+1}) \\ u_N =& - k_i^f(\tilde{p}_N - \tilde{p}_{N-1}) - b_i^f(\dot{\tilde{p}}_N - \dot{\tilde{p}}_{N-1}), \end{aligned} \tag{3–3}$$

where $i \in \{1, \cdots, N-1\}$ and k_i^f, k_i^b (respectively, b_i^f, b_i^b) are the front and back position (respectively, velocity) gains of the i-th vehicle. Note that the information needed to compute the control action can be easily accessed by on-board sensors, since only relative information is used.

Results in [62, 67, 84] show that heterogeneity in vehicle mass and control gains has little effect on the sensitivity to disturbance and stability margin of the platoon. Therefore we focus on *homogeneous* platoons, in which every vehicle has the same dynamics and employs the same control law. In particular,

$$\begin{aligned} k_i^f &= (1+\varepsilon_k)k_0, \quad k_i^b = (1-\varepsilon_k)k_0, \\ b_i^f &= (1+\varepsilon_b)b_0, \quad b_i^b = (1-\varepsilon_b)b_0, \\ m_i &= 1, \qquad\qquad i \in \{1, 2, \cdots, N\}, \end{aligned} \tag{3–4}$$

where $\varepsilon_k \in [0,1]$ and $\varepsilon_b \in [0,1]$ are the amounts of asymmetry in the position and velocity gains respectively.

Definition 3.1. *We call the architecture corresponding to $\varepsilon_k = \varepsilon_b = 0$ the* symmetric bidirectional*, since the control action on each vehicle depends equally on the information from its immediate predecessor and follower; and the architecture corresponding to*

$\varepsilon_k = \varepsilon_b = 1$ *are called the* predecessor-following*, since the control action on each vehicle only depends on the information from its immediate predecessor. The architecture corresponding to other cases is called* asymmetric bidirectional. □

We study how the sensitivities to external disturbances scale with respect to the number of vehicles N in the platoon. We define the following two metrics.

Definition 3.2. *The* leader-to-trailer amplification H_{LTT} *is defined as the* H_∞ *norm of the transfer function from the disturbance on the leader to the last vehicle's position tracking error. The* all-to-all amplification H_{ATA} *is defined as the* H_∞ *norm of the transfer function from the disturbances acting on all the followers to their position tracking errors.* □

In the case of leader-to-trailer amplification, we assume there is a sinusoidal disturbance only on the leader, whereas the other vehicles are undisturbed, i.e. $w_i = 0, i \in \{1, \cdots, N\}$. We examine the effect of the disturbance on the leader $W = w_0 = a_0 \sin(\omega t + \theta_0) \in \mathbb{R}$ to the position tracking error of the last vehicle $E = \tilde{p}_N \in \mathbb{R}$. Without loss of generality, let $a_0 = 1$ and $\theta_0 = 0$ for this case. With this sinusoidal disturbance, the desired trajectory of the leader is now given by $p_0^*(t) = vt + \Delta_{(0,N)} + \sin(\omega t)$. In the predecessor-following architecture, the closed-loop dynamics can now be expressed as the following coupled-ODE model

$$\ddot{\tilde{p}}_i = -2k_0(\tilde{p}_i - \tilde{p}_{i-1}) - 2b_0(\dot{\tilde{p}}_i - \dot{\tilde{p}}_{i-1}) + \omega^2 \sin(\omega t), \tag{3–5}$$

where $i \in \{1, \cdots, N\}$. For the bidirectional architecture, the closed-loop dynamics can be expressed as

$$\begin{aligned} \ddot{\tilde{p}}_i = &- k_i^f(\tilde{p}_i - \tilde{p}_{i-1}) - k_i^b(\tilde{p}_i - \tilde{p}_{i+1}) \\ &- b_i^f(\dot{\tilde{p}}_i - \dot{\tilde{p}}_{i-1}) - b_i^b(\dot{\tilde{p}}_i - \dot{\tilde{p}}_{i+1}) + \omega^2 \sin(\omega t), \\ \ddot{\tilde{p}}_N = &- k_i^f(\tilde{p}_N - \tilde{p}_{N-1}) - b_i^f(\dot{\tilde{p}}_N - \dot{\tilde{p}}_{N-1}) + \omega^2 \sin(\omega t), \end{aligned} \tag{3–6}$$

where $i \in \{1, \cdots, N-1\}$.

In the case of all-to-all amplification, we assume there are disturbances acting on all the followers but not the leader, and study the H_∞ norm of the transfer function from the disturbances on all the followers $W = [w_1, w_2, \cdots, w_N] \in \mathbb{R}^N$ to their position tracking errors $E = [\tilde{p}_1, \tilde{p}_2, \cdots, \tilde{p}_N] \in \mathbb{R}^N$, where $\tilde{p}_i$ is defined in (3–2). Since there is no disturbance on the leader, its desired trajectory is then given by $p_0^*(t) = vt + \Delta_{(0,N)}$. Using the position tracking errors defined in (3–2), for the predecessor-following architecture, the closed-loop dynamics can be expressed as

$$\ddot{\tilde{p}}_i = -k_i^f(\tilde{p}_i - \tilde{p}_{i-1}) - b_i^f(\dot{\tilde{p}}_i - \dot{\tilde{p}}_{i-1}) + w_i, \tag{3–7}$$

where $i \in \{1, \cdots, N\}$. For the bidirectional architecture, the closed-loop dynamics can be written as

$$\begin{aligned} \ddot{\tilde{p}}_i = &-k_i^f(\tilde{p}_i - \tilde{p}_{i-1}) - k_i^b(\tilde{p}_i - \tilde{p}_{i+1}) \\ &- b_i^f(\dot{\tilde{p}}_i - \dot{\tilde{p}}_{i-1}) - b_i^b(\dot{\tilde{p}}_i - \dot{\tilde{p}}_{i+1}) + w_i, \\ \ddot{\tilde{p}}_N = &-k_i^f(\tilde{p}_N - \tilde{p}_{N-1}) - b_i^f(\dot{\tilde{p}}_N - \dot{\tilde{p}}_{N-1}) + w_N, \end{aligned} \tag{3–8}$$

where $i \in \{1, \cdots, N-1\}$.

For both the disturbance amplifications considered above, the coupled-ODE models with the predecessor-following and bidirectional architectures can be represented in the following state-space form:

$$\dot{X} = AX + BW, \quad E = CX, \tag{3–9}$$

where X is the state vector, which is defined as $X := [\tilde{p}_1, \dot{\tilde{p}}_1, \cdots, \tilde{p}_N, \dot{\tilde{p}}_N] \in \mathbb{R}^{2N}$, W is input vector (external disturbances) and E is the output vector (position tracking errors). For example, the state matrix for the predecessor-following and symmetric bidirectional architecture are given by $A^{p \text{ or } b} = I_N \otimes M_1 + L^{p \text{ or } b} \otimes M_2$, where I_N is the $N \times N$ identity

matrix and $\otimes$ denotes the Kronecker product. The auxiliary matrices M_1, M_2 are given by:

$$M_1 = \begin{bmatrix} 0 & 1 \\ 0 & 0 \end{bmatrix}, \quad M_2 = \begin{bmatrix} 0 & 0 \\ -k_0 & -b_0 \end{bmatrix}.$$

The matrix $L^{(\cdot)}$ for the predecessor-following and symmetric bidirectional architectures are respectively given by

$$L^p = \begin{bmatrix} 1 & & & \\ -1 & 1 & & \\ & \ddots & \ddots & \\ & & -1 & 1 \end{bmatrix}, \quad L^b = \begin{bmatrix} 2 & -1 & & & \\ -1 & 2 & -1 & & \\ & \ddots & \ddots & \ddots & \\ & & -1 & 2 & -1 \\ & & & -1 & 1 \end{bmatrix}.$$

For the case of the leader-to-trailer amplification, the input matrix B and output matrix C are given by $B = \omega^2[0, 1, \cdots, 0, 1]^{\mathrm{T}} \in \mathbb{R}^{2N}$, $C = [0, 0, \cdots, 0, 1, 0] \in \mathbb{R}^{2N}$ respectively. The corresponding matrices for the case of all-to-all amplification are given by $B = I_N \otimes [0, 1]^{\mathrm{T}}$, $C = I_N \otimes [1, 0]$ respectively. The case with asymmetric control can be constructed similarly, but the state matrix A in general does not have such "nice" form as shown above.

Recall that the H_∞ norm of a transfer function $G(s) = C(sI - A)^{-1}B$ from W to E is defined as:

$$||G(j\omega)||_{H_\infty} = \sup_{\omega \in \mathbb{R}^+} \sigma_{\max}[G(jw)] = \sup_{W} \frac{||E||_{\mathcal{L}_2}}{||W||_{\mathcal{L}_2}}, \tag{3–10}$$

where $\sigma_{\max}$ denotes the maximum singular value. [1] For the predecessor-following architecture, the dynamics of each vehicle only depend on the information from its predecessor. Due to this special coupled structure, a closed-form transfer function can be derived.

[1] In this chapter, the $\mathcal{L}_2$ norm is well-defined in the extended space $\mathcal{L}_e^2 = \{u | u_\tau \in \mathcal{L}^2, \forall\, \tau \in [0, \infty)\}$, where $u_\tau(t) = (i)\ u(t),\ \text{if } 0 \le t \le \tau; (ii)\ 0,\ \text{if } t > \tau$. See [85, Chapter 5]. With a little abuse of notation, we suppress the subscript and write $\mathcal{L}^2 = \mathcal{L}_e^2$.

Therefore we can derive estimates for the leader-to-trailer and all-to-all amplifications by using standard matrix theory. However, for bidirectional architecture, it is in general difficult to find a closed-form formula for the leader-to-trailer and all-to-all amplifications from the state-space domain. There are several reasons. First of all, when the number of vehicles in the platoon is large, it's very involved to compute matrix inverse and multiplications, which makes it difficult to find a closed-form transfer function for this architecture. Second, the coupled-ODE model provides no information about at which frequency ω the system's resonance occurs and which input causes the worst disturbance amplification. Third, the calculation of singular value for a large matrix is not a easy task. Due to these reasons, we take an alternate route and propose a PDE model, which is seen as a continuum approximation of the coupled-ODE models (3–6) and (3–8), to analyze and study the H_∞ norms of the 1-D platoon of double-integrator vehicles. This PDE model provides a convenient framework to analysis. Base on the PDE model, closed-form formulae of the H_∞ norms and resonance frequency are obtained.

3.2 PDE Models of the Platoon with Symmetric Bidirectional Architecture

The analysis in the symmetric bidirectional architecture relies on PDE models, which are seen as a continuum approximation of the closed loop dynamics (3–6) and (3–8) in the limit of large N, by following the steps involved in a finite-difference discretization in reverse. The derivation of the PDE model is similar to the procedures in the previous chapter.

3.2.1 PDE Model for the Case of Leader-to-Trailer Amplification

We first derive a PDE model for the case of leader-to-trailer amplification, where there is disturbance only on the leader, i.e. $w_i = 0$, for $i \in \{1, 2, \cdots, N\}$. With symmetric control gains $k_i^f = k_i^b = k_0, b_i^f = b_i^b = b_0$, the closed-loop dynamics (3–6) can be written as

$$\ddot{\tilde{p}}_i = \frac{k_0}{N^2}\frac{(\tilde{p}_{i-1} - 2\tilde{p}_i + \tilde{p}_{i+1})}{1/N^2} + \frac{b_0}{N^2}\frac{(\dot{\tilde{p}}_{i-1} - 2\dot{\tilde{p}}_i + \dot{\tilde{p}}_{i+1})}{1/N^2} + \omega^2 \sin(\omega t). \tag{3–11}$$

Following the same procedures in Chapter 2, we consider a function $\tilde{p}(x,t) : [0,1] \times [0, \infty) \to \mathbb{R}$ that satisfies:

$$\tilde{p}_i(t) = \tilde{p}(x,t)|_{x=(N-i)/N}, \tag{3–12}$$

such that functions that are defined at discrete points i will be approximated by functions that are defined everywhere in $[0,1]$. The original functions are thought of as samples of their continuous approximations. Use the following finite difference approximations:

$$\left[\frac{\tilde{p}_{i-1} - 2\tilde{p}_i + \tilde{p}_{i+1}}{1/N^2}\right] = \left[\frac{\partial^2 \tilde{p}(x,t)}{\partial x^2}\right]_{x=(N-i)/N},$$
$$\left[\frac{\dot{\tilde{p}}_{i-1} - 2\dot{\tilde{p}}_i + \dot{\tilde{p}}_{i+1}}{1/N^2}\right] = \left[\frac{\partial^3 \tilde{p}(x,t)}{\partial x^2 \partial t}\right]_{x=(N-i)/N}.$$

Under the assumption that N is large but finite, Eq. (3–11) can be seen as finite difference discretization of the following PDE:

$$\frac{\partial^2 \tilde{p}(x,t)}{\partial t^2} = \frac{k_0}{N^2}\frac{\partial^2 \tilde{p}(x,t)}{\partial x^2} + \frac{b_0}{N^2}\frac{\partial^3 \tilde{p}(x,t)}{\partial x^2 \partial t} + \omega^2 \sin(\omega t). \tag{3–13}$$

The boundary conditions of PDE (3–13) depend on the arrangement of leader in the graph. For our case, the boundary conditions are of the Dirichlet type at $x = 1$ where the leader is, and Neumann at $x = 0$:

$$\frac{\partial \tilde{p}}{\partial x}(0,t) = 0, \qquad \tilde{p}(1,t) = 0. \tag{3–14}$$

3.2.2 PDE Model for the Case of All-to-All Amplification

For this case, there are disturbances on all the followers but no disturbance on the leader. With symmetric control, the closed-loop dynamics are slightly different from (3–11), which are given by

$$\ddot{\tilde{p}}_i = \frac{k_0}{N^2}\frac{(\tilde{p}_{i-1} - 2\tilde{p}_i + \tilde{p}_{i+1})}{1/N^2} + \frac{b_0}{N^2}\frac{(\dot{\tilde{p}}_{i-1} - 2\dot{\tilde{p}}_i + \dot{\tilde{p}}_{i+1})}{1/N^2} + a_i \sin(\omega t + \theta_i). \tag{3–15}$$

Following the same procedure as in 3.2.1, we derive the following PDE model

$$\frac{\partial^2 \tilde{p}(x,t)}{\partial t^2} = \frac{k_0}{N^2}\frac{\partial^2 \tilde{p}(x,t)}{\partial x^2} + \frac{b_0}{N^2}\frac{\partial^3 \tilde{p}(x,t)}{\partial x^2 \partial t} + a(x)\sin(\omega t + \theta(x)), \tag{3–16}$$

where $a(x), \theta(x) : [0,1] \to \mathbb{R}$ defined according to the following stipulations:

$$a_i = a(x)|_{x=\frac{N-i}{N}}, \qquad \theta_i = \theta(x)|_{x=\frac{N-i}{N}}. \tag{3–17}$$

The boundary conditions of the above PDE (3–16) are the same as before, which is given in (3–14).

The PDE models (3–13) and (3–16) are forced wave equations with Kelvin-Voigt damping. They are approximations of the coupled-ODE models in the sense that a finite difference discretization of the PDEs yield (3–6) and (3–8) respectively. The finite difference method to numerically solve partial differential equation, its approximation errors and stability analysis are well studied in [77, 86]. Interested reader is referred to [77, 86] for a comprehensive study.

3.3 Robustness to External Disturbances

3.3.1 Leader-to-trailer amplification with symmetric bidirectional architecture

For a single-input-single-output system, the H_∞ norm of the platoon is effectively the maximum magnitude of the frequency response. For any sinusoidal disturbance $w_0 = \sin(\omega t)$ on the leader, we need to find the sinusoidal output $\tilde{p}(0,t)$ with the maximum amplitude over all frequencies ω.

We first present the first main result of this chapter concerning the leader-to-trailer amplification for symmetric bidirectional architecture.

Theorem 3.1. *Consider the PDE model (3–13)-(3–14) of the 1-D platoon with symmetric bidirectional architecture, the leader-to-trailer amplification H^{sb}_{LTT} and resonance frequency ω^{sb}_r have the asymptotic formula*

$$H^{sb}_{LTT} \approx \frac{8\sqrt{k_0}N}{b_0\pi^2}, \quad \omega^{sb}_r \approx \frac{\sqrt{k_0}\pi}{2N}. \tag{3–18}$$

These formulae hold for large N. □

Proof of Theorem 3.1. Consider the case of leader-to-trailer amplification, whose dynamics are characterized by PDE (3–13) with boundary condition (3–14). It is a nonhomogeneous PDE with homogeneous boundary conditions. The solution of $\tilde{p}(0,t)$ can be solved by eigenfunction expansion, see [77, Chapter 8]. To proceed, we first consider the following homogeneous PDE with homogeneous boundaries (3–14)

$$\frac{\partial^2 \tilde{p}(x,t)}{\partial t^2} = \frac{k_0}{N^2}\frac{\partial^2 \tilde{p}(x,t)}{\partial x^2} + \frac{b_0}{N^2}\frac{\partial^3 \tilde{p}(x,t)}{\partial x^2 \partial t}. \tag{3–19}$$

The above PDE can be solved by the method of separation of variables, we assume solution of the form $\tilde{p}(x,t) = \sum_{\ell=1}^{\infty} \phi_\ell(x) h_\ell(t)$. Substituting the solution into the above PDE (3–19), we get the following space-dependent ODE

$$\frac{1}{N^2}\frac{d^2\phi_\ell(x)}{dx^2} + \lambda_\ell \phi_\ell(x) = 0, \tag{3–20}$$

where $\lambda_\ell = (2\ell-1)^2\pi^2/(4N^2)$ and $\phi_\ell(x) = \cos((2\ell-1)\pi x/2)$ are the eigenvalue and its corresponding eigenfunction of the Sturm-Liouville eigenvalue problem (3–20) with following boundary conditions, which come from (3–14),

$$\frac{d\phi_\ell}{dx}(0) = 0, \qquad\qquad \phi_\ell(1) = 0. \tag{3–21}$$

Notice that the eigenvalue λ_1 is the smallest eigenvalue, which is called the principal mode of the damped wave equation (3–19). Since the eigenfunctions are complete (because of Sturm-Liouville Theory), any piecewise smooth functions can be expanded in a series of these eigenfunctions, see [77]. Therefore, we expand the external forcing terms in PDE (3–13) as

$$\omega^2 \sin(\omega t) = \sum_{\ell=1}^{\infty} c_\ell \phi_\ell(x) \omega^2 \sin(\omega t), \tag{3–22}$$

where c_ℓ is given by $c_\ell = 2\int_0^1 \phi_\ell(x)\, dx = (-1)^{\ell+1}4/((2\ell-1)\pi)$. Substituting (3–22) into PDE (3–13), and using $\tilde{p}(x,t) = \sum_{\ell=1}^{\infty} \phi_\ell(x) h_\ell(t)$, we get the following ODEs

$$\frac{d^2 h_\ell(t)}{dt^2} + b_0\lambda_\ell \frac{dh_\ell(t)}{dt} + k_0\lambda_\ell h_\ell(t) = c_\ell \omega^2 \sin(\omega t), \tag{3–23}$$

where $\ell \in \{1, 2, \cdots\}$. These are second order systems with sinusoidal input whose amplitude depends on their frequency ω.

For each mode λ_ℓ, the steady-state response $h_\ell(t)$ is given by

$$\begin{aligned} h_\ell(t) &= \frac{c_\ell \omega^2}{\sqrt{\omega^4 + (b_0^2\lambda_\ell^2 - 2k_0\lambda_\ell)\omega^2 + k_0^2\lambda_\ell^2}} \sin(\omega t + \psi_\ell) \\ &= A_\ell \sin(\omega t + \psi_\ell) \end{aligned} \tag{3–24}$$

for some constant ψ_ℓ. The maximum amplitude A_ℓ and its resonance frequency for each mode can be determined by a straightforward manner, which are:

$$A_\ell = \frac{8N}{(2\ell-1)^2\pi^2} \frac{1}{\sqrt{b_0^2/k_0 - (2\ell-1)^2 b_0^4\pi^2/(16k_0^2N^2)}}, \tag{3–25}$$

$$\omega_\ell = \frac{\sqrt{k_0}\pi}{\sqrt{4N^2 - b_0^2\pi^2/(2k_0^2)}}. \tag{3–26}$$

The position tracking error of the last vehicle is now given by $\tilde{p}(0,t) = \sum_{\ell=1}^{\infty} \phi_\ell(0) h_\ell(t) = \sum_{\ell=1}^{\infty} A_\ell \sin(\omega t)$. To get the maximum amplitude, the frequency ω must be one of the resonance frequency ω_ℓ of the damped wave equation (3–13), see [77]. For large N, it's not difficult to see from (3–25) that, the maximum is achieve at $\omega_r^{sb} = \omega_1$. Moreover, since A_1 dominates the other A_ℓ ($\ell = 2, 3, \cdots$), the H_∞ norm of the system is approximately A_1. Using the assumption that N is large in (3–25) and (3–26), we compete the proof. □

3.3.2 All-to-all Amplification with Symmetric Bidirectional Architecture

We now present the result on all-to-all amplification for the 1-D platoon of double-integrator vehicles with symmetric bidirectional architecture.

Theorem 3.2. *Consider the PDE model (3–14)-(3–16) of the 1-D platoon with symmetric bidirectional architecture, the all-to-all amplification H_{ATA}^{sb} and resonance frequency ω_r^{sb}*

have the asymptotic formula

$$H_{ATA}^{sb} \approx \frac{8N^3}{\sqrt{k_0}b_0\pi^3}, \quad \omega_r^{sb} \approx \frac{\sqrt{k_0}\pi}{2N}. \tag{3–27}$$

These formulae hold for large N. □

Proof of Theorem 3.2. For a multi-input-multi-output system, the H_∞ norm is defined as the supremum of the maximum singular value of the transfer function matrix $G(j\omega)$ over all frequency $\omega \in \mathbb{R}^+$. Equivalently, it can be interpreted in a sinusoidal, steady-state sense as follows (see [87]). For any frequency ω, any vector of amplitudes $a = [a_1, \cdots, a_N]$ with $\|a\|_2 \leq 1$, and any vector of phases $\theta = [\theta_1, \cdots, \theta_N]$, the input vector

$$\begin{aligned} W &= [w_1, \cdots, w_N] \\ &= [a_1 \sin(\omega t + \theta_1), \cdots, a_N \sin(\omega t + \theta_N)] \end{aligned} \tag{3–28}$$

yields the steady-state response of E of the form

$$E = [\tilde{p}_1, \cdots, \tilde{p}_N] = [b_1 \sin(\omega t + \psi_1), \cdots, b_N \sin(\omega t + \psi_N)]. \tag{3–29}$$

The H_∞ norm of $G(j\omega)$ can be defined as

$$\|G(j\omega)\|_{H_\infty} = \sup \|b\|_2 = \sup_{\omega \in \mathbb{R}^+, a, \theta \in \mathbb{R}^N} \frac{\|E\|_{\mathcal{L}_2}}{\|W\|_{\mathcal{L}_2}}, \tag{3–30}$$

where $b = [b_1, \cdots, b_N]$. Therefore, in the PDE counterpart, the H_∞ norm is determined by

$$H_\infty = \sup_{\omega \in \mathbb{R}^+, a(x), \theta(x)} \frac{||\tilde{p}(x,t)||_{\mathcal{L}_2}}{\|a(x)\sin(\omega t + \theta(x))\|_{\mathcal{L}_2}}, \tag{3–31}$$

where $a(x)$ and $\theta(x)$ are piecewise smooth functions defined in $[0, 1]$.

PDE (3–16) is a nonhomogeneous PDE with homogeneous boundary conditions, therefore we can use eigenfunction expansion to expand the nonhomogeneous terms. Before we proceed, notice that

$$a(x)\sin(\omega t + \theta(x)) = a_1(x)\sin(\omega t) + a_2(x)\cos(\omega t),$$

where $a_1(x) = a(x)\cos(\theta(x))$ and $a_2(x) = a(x)\sin(\theta(x))$. From the superposition property of linear system, the output is the sum of the outputs corresponding to inputs $a_1(x)\sin(\omega t)$ and $a_2(x)\cos(\omega t)$ respectively.

We first consider the response of the PDE with input $a_1(x)\sin(\omega t)$. The PDE is now given by

$$\frac{\partial^2 \tilde{p}(x,t)}{\partial t^2} = \frac{k_0}{N^2}\frac{\partial^2 \tilde{p}(x,t)}{\partial x^2} + \frac{b_0}{N^2}\frac{\partial^3 \tilde{p}(x,t)}{\partial x^2 \partial t} + a_1(x)\sin(\omega t). \tag{3–32}$$

As before, using eigenfunction expansion, $a_1(x)$ can be expanded as a series in terms of $\phi_\ell(x)$, i.e. $a_1(x) = \sum_{\ell=1}^{\infty} d_\ell \phi_\ell(x)$. Substituting the series into the above PDE and using $\tilde{p}(x,t) = \sum_{\ell=1}^{\infty} \phi_\ell(x) h_\ell(t)$, we have the following time-dependent ODEs:

$$\frac{d^2 h_\ell(t)}{dt^2} + b_0\lambda_\ell \frac{dh_\ell(t)}{dt} + k_0\lambda_\ell h_\ell(t) = d_\ell \sin(\omega t), \tag{3–33}$$

where $\ell \in \{1, 2, \cdots\}$ and d_ℓ is given by

$$d_\ell = 2\int_0^1 a_1(x)\phi_\ell(x)\, dx. \tag{3–34}$$

Again, for each mode λ_ℓ, the steady-state response $h_\ell(t)$ is given by

$$\begin{aligned} h_\ell(t) &= \frac{d_\ell}{\sqrt{\omega^4 + (b_0^2\lambda_\ell^2 - 2k_0\lambda_\ell)\omega^2 + k_0^2\lambda_\ell^2}} \sin(\omega t + \psi_\ell) \\ &= A_\ell d_\ell \sin(\omega t + \psi_\ell), \end{aligned} \tag{3–35}$$

for some constant ψ_ℓ. Following straightforward algebra, the maximum amplitude A_ℓ and its resonance frequency for each mode is

$$A_\ell = \begin{cases} \frac{8N^3}{(2\ell-1)^3 b_0 \pi^3} \frac{1}{\sqrt{k_0 - (2\ell-1)^2 b_0^2 \pi^2/(16N^2)}}, & \text{if } \ell \le \ell_0 \\ \frac{1}{\lambda_\ell k_0}, & \text{otherwise.} \end{cases} \tag{3–36}$$

$$\omega_\ell = \begin{cases} \frac{(2\ell-1)\pi}{2N}\sqrt{k_0 - (2\ell-1)^2 b_0^2 \pi^2/(8N^2)}, & \text{if } \ell \le \ell_0 \\ 0, & \text{otherwise.} \end{cases} \tag{3–37}$$

where $\ell_0 = \frac{2\sqrt{2k_0}N+\pi}{2\pi}$.

Again, when N is large, it's not difficult to see from (3–36) that, the maximum of A_ℓ is achieve at $\omega = \omega_1$. Therefore, for a finite $\mathcal{L}_2$ norm of $a_1(x)$, to achieve the largest $\mathcal{L}_2$ norm of $\tilde{p}(x,t)$, $a_1(x)$ should be equal to the eigenfunction of the first mode $a_1(x) = \phi_1(x)$, i.e. the projection of $a_1(x)$ onto other eigenfunctions is zero $d_\ell = 0$ ($\ell = 2, 3, \cdots$). Similarly, the following relationship $a_2(x) = \phi_1(x)$ should hold for input $a_2(x)\cos(\omega t)$, which implies $\theta(x) = \theta_0$ is constant, since $a_1(x) = a(x)\cos(\phi(x))$ and $a_2(x) = a(x)\sin(\phi(x))$.

Consequently, the output with the maximum $\mathcal{L}_2$ norm is given by

$$\tilde{p}(x,t) = A_1\phi_1(x)\sin(\omega t + \psi_1). \tag{3–38}$$

Therefore, the H_∞ norm of the system is obtained

$$H_\infty = A_1\frac{\|\phi_1(x)\sin(\omega t + \psi_1)\|_{\mathcal{L}_2}}{\|\phi_1(x)\sin(\omega t + \theta_0)\|_{\mathcal{L}_2}} = A_1. \tag{3–39}$$

Using the assumption that N is large in (3–36) and (3–37), we compete the proof. □

3.3.3 Disturbance Amplification with Predecessor-Following Architecture

Similar results as leader-to-trailer amplification with predecessor-following architecture exist in the literature [31, 45]. In this section, we present these results for the sake of completion. In addition, we have also consider the case of all-to-all amplification.

Theorem 3.3. *Consider an N-vehicle platoon with predecessor-following architecture, the leader-to-trailer amplification H^p_{LTT} and all-to-all amplification H^p_{ATA} are asymptotically*

$$H^p_{LTT} \approx \alpha^N, \tag{3–40}$$

$$H^p_{ATA} \approx \beta\sqrt{\frac{\alpha^{2N}-1}{\alpha^2-1}}, \tag{3–41}$$

where the above formulae hold for large N. In particular, $\alpha = |T(j\omega_r^p)| > 1$, $\beta = |S(j\omega_r^p)|$, where

$$T(s) = \frac{2b_0 s + 2k_0}{s^2 + 2b_0 s + 2k_0}, \quad S(s) = \frac{1}{s^2 + 2b_0 s + 2k_0},$$

and ω_r is the resonance frequency for both cases, which is given by

$$\omega_r^p \approx \frac{\sqrt{\sqrt{k_0^4 + 4k_0^3 b_0^2} - k_0^2}}{b_0}.$$

□

The proof follows a similar line of attack as the work in [31]. Interested readers are referred to Corollary 1 of [88] for an explicit proof.

3.3.4 Disturbance Amplification with Asymmetric Bid. Architecture

For the asymmetric bidirectional architecture, we consider the following control gains, which stabilize the platoon, see Chapter 2:

1) Equal amount of asymmetry, i.e. $0 < \varepsilon_k = \varepsilon_b < 1$. In this case, it was shown in Theorem 3.5 of [68] that certain amplification factor (which is different from H_{LTT} and H_{ATA} defined in this chapter) grows exponentially in N. We show by numerical simulations that the leader-to-trailer H_{LTT}^{as} and all-to-all amplifications H_{ATA}^{as} with equal asymmetry are approximately $O(e^N)$, see Section 3.3.6. The asymmetric bidirectional architecture with equal asymmetry in the position and velocity feedback thus suffers from high sensitivity to disturbances, as the predecessor-following architecture. However, it doesn't imply asymmetric bidirectional architectures is not preferable, as shown below.

2) Asymmetric velocity feedback, i.e. $\varepsilon_k = 0, 0 < \varepsilon_b < 1$. It was shown in Chapter 2 that the stability margin, which is defined as the absolute value of the real part of the least stable eigenvalue of the state matrix A, can be improved considerably by using the asymmetric velocity feedback over symmetric control. The analysis was also carried out based on the PDE model we derived before. We conjecture that the robustness can also be ameliorated significantly with asymmetric velocity feedback, which is witnessed by extensive numerical simulations.

Conjecture 3.1. *Consider an N-vehicle platoon with asymmetric bidirectional architecture. When there is small asymmetry in the velocity feedback, i.e. $\varepsilon_k = 0, 0 < \varepsilon_b \ll 1$, the leader-to-trailer amplification H^{av}_{LTT} and all-to-all amplification H^{av}_{ATA} asymptotically satisfy*

$$H^{av}_{LTT} \approx O(1), \quad H^{av}_{ATA} \approx O(N^2). \qquad \square$$

3.3.5 Design Guidelines

Comparing the above conjecture with those results in Theorem 3.1, Theorem 3.2 and Theorem 3.3 as well as Theorem 3.5 of [68] (equal asymmetry), we see that asymmetric velocity feedback yields the best robustness performance compared to other architectures. The next preferable choice is the symmetric bidirectional architecture. The predecessor-following and asymmetric bidirectional with equal amount of asymmetry are the worst choices for control design in terms of robustness, their leader-to-trailer and all-to-all amplifications grow extremely fast with N.

Besides the robustness performance metrics analyzed in this chapter, it was also studied in the previous chapter that how the stability margin scales with the size of platoon. It was shown in the previous chapter that with symmetric bidirectional architecture, the stability margin decays to zero as $O(1/N^2)$. It can be improved to $O(1/N)$ with asymmetric velocity feedback. In addition, it was shown in [88] and [89] that with predecessor-following architecture and asymmetric bidirectional architecture with equal asymmetry, the stability margin are $O(1)$. However, the transient errors in these architectures grow considerably before they die out.

In conclusion, to get a better stability margin and robustness performance, the asymmetric velocity feedback is the best choice for control design.

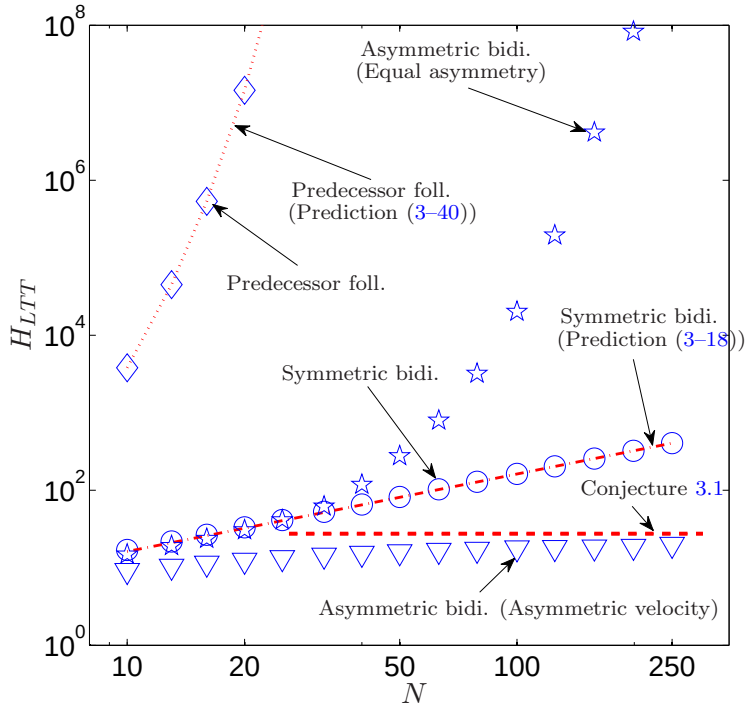

(a) Leader-to-trailer amplification H_{LTT}

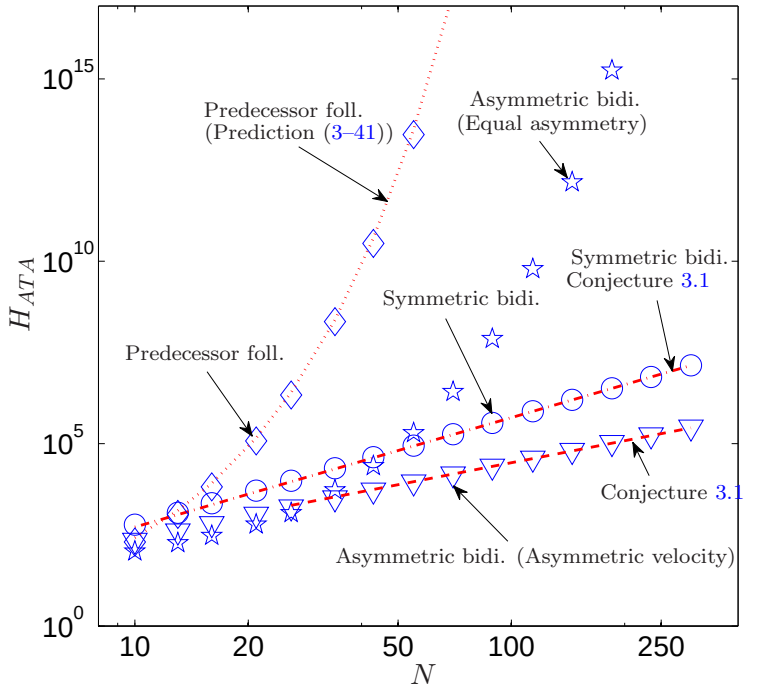

(b) All-to-all amplification H_{ATA}

Figure 3-1. Numeric comparison of disturbance amplification between different architectures.

3.3.6 Numerical Verification

In this section, we compare the robustness of the platoon with different control architectures. In addition, we verify the analytic predictions in Theorem 3.1, Theorem 3.2 and Theorem 3.3 with their numerically computed values. All numerical calculations are performed in Matlab©. Figure 3-1 shows the comparison between the predecessor-following and bidirectional architectures for both the leader-to-trailer amplification and all-to-all amplification. We can see that for both amplifications, they grow geometrically in the predecessor-following architecture and asymmetric bidirectional architecture with equal asymmetry. In contrast, in the symmetric bidirectional architecture, these amplifications grow much slower than the two architectures aforementioned. In addition, the asymmetric velocity feedback architecture gives the best robustness performance. Besides, we see that the numerical results of the two amplifications in the asymmetric velocity feedback architecture coincide with our conjecture. Moreover, the analytic predictions match the numerical results very well, which verified our analysis in Theorem 3.1, Theorem 3.2 and Theorem 3.3. In all cases, the control gains used are $k_0 = 1$ and $b_0 = 0.5$. The amounts of asymmetry in the cases of equal asymmetry and asymmetric velocity feedback are given by $\varepsilon_k = \varepsilon_b = 0.2$ and $\varepsilon_k = 0, \varepsilon_b = 0.2$ respectively.

3.4 Summary

We studied the robustness to external disturbances of large platoon of vehicles with two decentralized control architectures: predecessor-following and bidirectional. In particular, we examined how the leader-to-trailer amplification and all-to-all amplification scale with N, the number of vehicles in the platoon. For both metrics, we obtained their explicit scaling laws with respect to the number of vehicles in the platoon for symmetric control. In addition, we also consider the effect of asymmetric control on the disturbance amplification. Numerical simulations show that the asymmetric velocity feedback in the bidirectional architecture has much lower sensitivity to external disturbance than the other

architectures. The analysis of asymmetric control on the robustness to disturbance is an ongoing work.

CHAPTER 4
STABILITY MARGIN AND ROBUSTNESS OF VEHICLE TEAMS WITH D-DIMENSIONAL INFORMATION GRAPH

We consider the problem of formation control of vehicles in higher-dimensional space so that neighboring vehicles maintain a constant pre-specified spacing while in motion. This problem is relevant to a number of applications such as formation flying of aerial, ground, and autonomous vehicles for surveillance, reconnaissance, mine-sweeping. The interaction between vehicles is described by an information graph. In this chapter, we limit our attention to a specific class of information graphs, namely, D-dimensional (finite) lattices. These are natural choices for information graphs in 2D or 3D formation problems in which vehicles are arranged in regular pattern and relative measurements are possible among physically closest vehicles. The platoon problem is a special case, whose information graph is a 1-D lattice. A few lead vehicles are provided information on their desired trajectories that they use in computing their control actions; while the rest of the vehicles are allowed to use only locally available information.

The one-dimensional version of this problem, in which a string of vehicles moving in a straight line have to be controlled to maintain a constant inter-vehicle separation, has been extensively studied [38, 48, 51]. The general trend of the results is that the problem scales poorly with the number of vehicles: as the number of vehicles increase the sensitivity to disturbances increases [31, 52, 53] and the stability margin decays [47, 48]. The information graphs considered in the literature are usually limited to at most two neighbors, with notable exceptions such as [53, 62, 90] that consider more general information exchange architectures.

Our goal is to examine how the stability margin and robustness to external disturbances scale with the size of the formation and the structure of the information graph that specifies allowable information exchange between pairs of vehicles. Each vehicle is modeled as a double integrator, and we assume that the vehicle is fully actuated, which means each coordinate of the position of the vehicle can be independently controlled. A distributed

control algorithm is studied in which every vehicle (except for a few lead vehicles) use only relative position and relative velocity with respect to its neighbors in the information graph.

We show that when the network is homogeneous and symmetric (all vehicles use the same control gains and information from each neighbor is given equal weight), the stability margin decays to 0 as $O(1/N^{2/D})$ when the graph is "square". Therefore, increasing the dimension (which may need nodes physically apart to exchange information) of the information graph can improve the stability margin by a considerable amount. For non-square information graph, the stability margin can be made independent of the number of agents by choosing the "aspect ratio" appropriately. That may entail an increase in the number of lead vehicles that have access to the formation's desired trajectory.

The rest of this chapter is organized as follows. Section 4.1 presents the distributed formation control problem and the main results. The state-space and PDE model of the controlled formation is described in Section 4.2. Section 4.3 analyzes the scaling laws of the stability margin and disturbance amplification with D-dimensional information graph. The chapter ends with a summary given in Section 4.4.

4.1 Problem Formulation and Main Results

4.1.1 Problem Formulation

We consider the formation control of N identical vehicles. The position of each vehicle is a D_s-dimensional vector (with $D_s = 1, 2$ or 3); D_s is referred to as the *spatial dimension* of the formation. Let $p_i^{(\mathrm{d})} \in \mathbb{R}$ be the d-th coordinate of the i-th vehicle's position, whose dynamics are modeled by a double integrator:

$$\ddot{p}_i^{(\mathrm{d})} = u_i^{(\mathrm{d})} + w_i^{(\mathrm{d})}, \qquad \mathrm{d} = 1, \ldots, D_s, \tag{4–1}$$

where $u_i^{(\mathrm{d})} \in \mathbb{R}$ is the control input and $w_i^{(\mathrm{d})} = a_i \sin(\omega t + \theta_i) \in \mathbb{R}$ is the external disturbances. The underlying assumption is that each of the D_s coordinates of a vehicle's position can be independently actuated. We say that the vehicles are *fully actuated*. The

spatial dimension D_s is 1 for a platoon of vehicles moving in a straight line, $D_s = 2$ for a formation of ground vehicles and $D_s = 3$ for a formation of flight vehicles. Under the above assumption, the each coordinates of a vehicle's position can be independently studied; see [3, 91] for examples.

The control objective is to make the group of vehicles track a pre-specified desired trajectory while maintaining a desired formation geometry. The desired formation geometry is specified by a desired relative position vector $\Delta_{i,j} := p_i^*(t) - p_j^*(t)$ for *every* pair of vehicles (i, j), where $p_i^*(t)$ is the desired trajectory of the vehicle i. The desired inter-vehicular spacings have to be specified in a mutually consistent fashion. Desired trajectory of the formation is specified in the form of a few fictitious "reference vehicles", each of which perfectly tracks its own desired trajectory. The reference vehicles are generalization of the fictitious leader and follower vehicles in one-dimensional platoons [43, 47, 48].
A subset of vehicles can measure their relative positions with respect to the reference vehicles, and these measurements are used in computing their control actions. In this way, desired trajectory information of the formation is specified only to a subset of the vehicles in the group. In this chapter we consider the desired trajectory of the formation to be of a constant-velocity type, so that $\Delta_{i,j}$'s don't change with time.

Next we define an *information graph* that makes it convenient to describe distributed control architectures.

Definition 4.1. *An* information graph *is an undirected graph* $\mathbf{G} = (\mathbf{V}, \mathbf{E})$*, where the set of* nodes $\mathbf{V} = \{1, 2, \ldots, N, N+1, \ldots, N+N_r\}$ *consists of* N *real vehicles and* N_r *reference vehicles. The set of edges* $\mathbf{E} \subset \mathbf{V} \times \mathbf{V}$ *specify which pairs of nodes (vehicles) are allowed to exchange information to compute their local control actions. Two nodes* i *and* j *are called* neighbors *if* $(i, j) \in \mathbf{E}$*, and the set of neighbors of* i *are denoted by* $\mathcal{N}_i$*.* □

Note that information exchange may or may not involve an explicit communication network. For example, if vehicle i measures the relative position of vehicle j with respect to itself by using a radar and uses that information to compute its control action, we

consider it as "information exchange" between i and j. If a vehicle i has access to desired trajectory information then there is an edge between i and a reference vehicle.

As in the previous chapters, we consider the following *distributed* control law, whereby the control action at a vehicle depends on i) the *relative position measurements* ii) the *relative velocity measurements* with its neighbors in the information graph:

$$u_i^{(\mathrm{d})} = \sum_{j \in \mathcal{N}_i} -k_{(i,j)}^{(\mathrm{d})}(p_i^{(\mathrm{d})} - p_j^{(\mathrm{d})} - \Delta_{i,j}^{(\mathrm{d})}) - b_{(i,j)}^{(\mathrm{d})}(v_i^{(\mathrm{d})} - v_j^{(\mathrm{d})}), \quad i = 1, \ldots, N, \tag{4–2}$$

where $k_{(\cdot)}^{(\mathrm{d})}$ are proportional gains and $b_{(\cdot)}^{(\mathrm{d})}$ are derivative gains. Note that all the variables in (4–2) are scalars. It is assumed that vehicle i knows its own neighbors (the set $\mathcal{N}_i$), and the desired spacing $\Delta_{i,j}^{(\mathrm{d})}$.

Example 4.1. *Consider the two formations shown in Figure 4-2 (a) and (b). Their spatial dimensions are $D_s = 1$ and $D_s = 2$, respectively. The information graph, however, is the same in both cases:*

$$\mathbf{V} = \{1, 2, \ldots, 9\},$$

$$\mathbf{E} = \{(1,2), (1,4), (1,7), (2,3), (2,5), (2,8), (3,6), (3,9), (4,5), (5,6), (7,8), (8,9)\}.$$

A drawing of the information graph appears in Figure 4-2 (c). Although the information graph is the same, the desired spacings $\Delta_{i,j}$'s are different in the two formations. For example, $\Delta_{2,5}^{(1)} \neq 0$ in the one-dimensional formation shown in Figure 4-2(a) whereas $\Delta_{2,5}^{(1)} = 0$ in the two-dimensional formation shown in Figure 4-2 (b).

In this chapter we restrict ourselves to a specific class of information graph, namely a finite rectangular lattice:

Definition 4.2 (D-dimensional lattice:)**.** *A D-dimensional lattice, specifically a $n_1 \times n_2 \times \cdots \times n_D$ lattice, is a graph with $n_1 n_2 \ldots n_D$ nodes. In the D-dimensional space $\mathbb{R}^D$, the coordinate of i-th node is $\vec{i} := [i_1, \ldots, i_D]^T$, where $i_1 \in \{0, 1, \ldots, (n_1 - 1)\}$, $i_2 \in \{0, 1, \ldots, (n_2 - 1)\}$, ... and $i_D \in \{0, 1, \ldots, (n_d - 1)\}$. An edge exists between two*

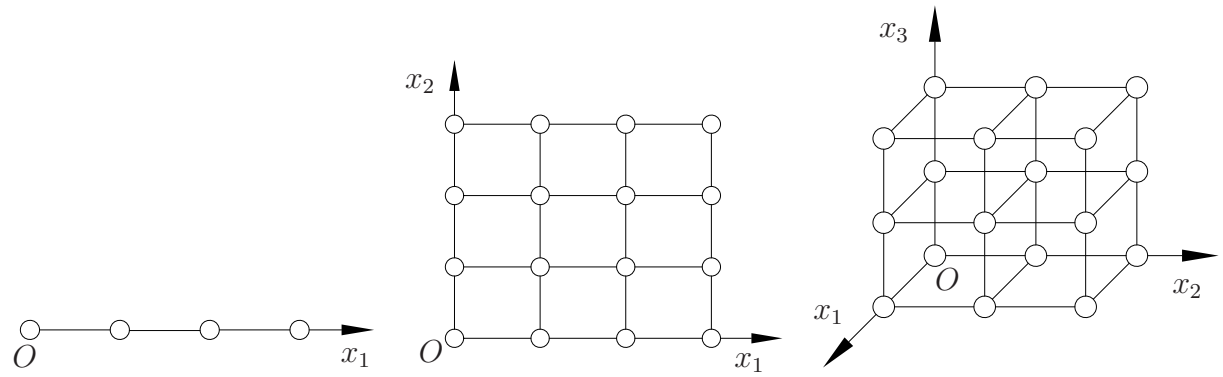

(a) A 1D 4 lattice. (b) A 2D 4×4 lattice. (c) A 3D $2 \times 3 \times 3$ lattice.

Figure 4-1. Examples of 1D, 2D and 3D lattices.

nodes $\vec{i}$ and $\vec{j}$ if and only if $\|\vec{i} - \vec{j}\| = 1$, where $\|\cdot\|$ is the Euclidean norm in $\mathbb{R}^D$. A $n_1 \times n_2 \times \cdots \times n_D$ lattice is denoted by $\mathbf{Z}_{n_1 \times n_2 \times \cdots \times n_D}$. With a slight abuse of notation, "the i-th node" is used to denote the node on the lattice with coordinate $\vec{i}$. □

Figure 4-1 depicts three examples of lattices. A D-dimensional lattice is drawn in $\mathbb{R}^D$ with a Cartesian reference frame whose axes are denoted by $x_1, x_2, \ldots, x_D$. Note that these coordinate axes may not be related to the coordinate axes in the physical space $\mathbb{R}^{D_s}$. We also define N_d $(d = 1, \ldots, D)$ as the number of real vehicles in the x_d direction. Then we have the relation $N_1 N_2 \ldots N_D = N$ and $n_1 n_2 \ldots n_D = N + N_r$. In this chapter an information graph $\mathbf{G}$ is always a lattice $\mathbf{Z}_{n_1 \times n_2 \cdots \times n_D}$. For a given N, the choice of $N_r, D, N_1, N_2, \ldots, N_D$ serves to determine the specific choice of the information graph within the class.

For the ease of exposition and notational simplicity, we make the following two assumptions regarding the reference vehicles and the distributed control architecture (4–2):

Assumption 4.1. *For each $(i,j) \in \mathbf{E}$, the gain $k_{(i,j)}^{(d)}$, $b_{(i,j)}^{(d)}$ does not depend on d.* □

Assumption 4.1 means that the local control gains do not explicitly depend upon the coordinate d. Such an assumption is not restrictive because of the fully actuated assumption. If the local control gains are allowed to depend upon d then one could repeat

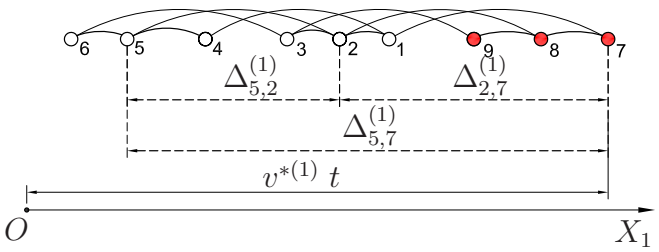

(a) Desired formation geometry of a 1-D spatial platoon with 6 vehicles and 3 reference vehicles.

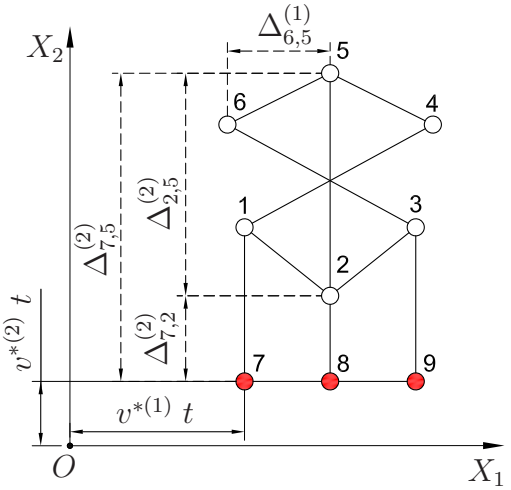

(b) Desired formation geometry of a 2-D spatial vehicle formation with 6 vehicles and 3 reference vehicles.

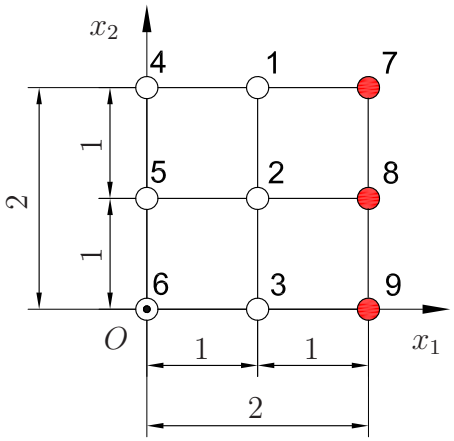

(c) The information graph for both the 1-D platoon and the 2-D formation shown in (a) and (b).

Figure 4-2. Example of two distinct spatial formations that have the same associated information graph.

the analysis of this chapter separately for each value of d. Note that the assumption does not mean that the control gains are spatially homogeneous.

Assumption 4.2. *The reference vehicles are arranged so that a node i in the information graph corresponds to a reference vehicle if and only if $i_1 = n_1 - 1$.* □

Assumption 4.2 means that all reference vehicles are assumed to be arranged on a single "face" of the lattice, and every vehicle on this face is a reference vehicle. Assumption 4.2 implies that $N_1 = n_1 - 1, n_2 = N_2, \cdots, N_D = n_D$ and $N = N_1 N_2 \dots N_D$ and $N_r = N_2 \dots N_D$. This arrangement of reference vehicles simplifies the presentation of the

results. Arrangements of reference vehicles on other boundaries of the lattice can also be considered, which does not significantly change the results. We have carried such analysis in [37, 92], we don't present them here in the interest of brevity.

An information graph is said to be *square* if $N_1 = N_2 = \ldots = N_D = N^{1/D}$.

As a result of the Assumption 4.1, we can rewrite (4–2) as

$$u_i = \sum_{j \in \mathcal{N}_i} -k_{(i,j)}(p_i - p_j - \Delta_{i,j}) - b_{(i,j)}(v_i - v_j), \tag{4–3}$$

where the superscript (d) has been suppressed.

Remark 4.1. *The dimension D of the information graph is distinct from the spatial dimension D_s. Figure 4-2 shows an example of two formations in space, one with $D_s = 1$ and the other with $D_s = 2$. Red (filled) circles represent reference vehicles and black (unfilled) circles represent actual vehicles. Dashed lines (in (a), (b)) represent desired relative positions, while solid lines represent edges in the information graph. The information graph for both the formations is the same 3×3 two-dimensional lattice, i.e., $D = 2$. On account of the fully actuated dynamics and Assumption 4.1, the spatial dimension D_s plays no role in the results of this chapter. The dimension of the information graph D, on the other hand, will be shown to play a crucial role.*

4.1.2 Main Result 1: Scaling Laws for Stability Margin

The first main result gives an asymptotic formula for controlled formation with symmetric control:

Theorem 4.1. *Consider an N-vehicle formation with vehicle dynamics (4–1) and control law (4–2), under Assumptions 4.1 and 4.2. With symmetric control, the stability margin of the closed-loop is given by the formula*

$$S = \frac{\pi^2 b_0}{8} \frac{1}{N_1^2}. \tag{4–4}$$

□

Square information graph. For a square information graph, $N = N_1 N_2 \dots N_D = N_1^D$, and we have the following corollary:

Corollary 4.1. *Consider an N-vehicle formation with vehicle dynamics (4–1) and control law (4–2), under Assumptions 4.1 and 4.2. When the information graph is a square D-dimensional lattice, the closed-loop stability margin with symmetric control is given by the asymptotic formula*

$$S = \frac{\pi^2 b_0}{8} \frac{1}{N^{2/D}}. \tag{4–5}$$

□

The result from Corollary 4.1 shows that for a constant choice of symmetric control gains k_0 and b_0, the stability margin approaches 0 as $N \to \infty$. The dimension D of the information graph determines the scaling. Specifically, the stability margin scales as $O(1/N^2)$ for 1D information graph, as $O(1/N)$ for 2D information graph, and as $O(1/N^{2/3})$ for 3D information graph. Thus, *for the same control gains, increasing the dimension of the information graph improves the stability margin significantly.* In practice, this may require a communication network with long range connections in the physical space. Note that an information graph is only a drawing of the connectivity. A neighbor in the information graph need not be physically close.

Remark 4.2. *It was shown in [47] that the closed-loop stability margin for a circular platoon approaches zero as $O(1/N^2)$ even with the centralized LQR controller. It is interesting to note that distributed control (with an information graph of dimension $D > 1$) yields a better scaling law for the stability margin than centralized LQR control.*

Non-square information graph. It follows from Theorem 4.1 that by choosing the structure of the information graph in such a way that n_1 increases slowly in relation to N, the loss of the stability margin as a function of N can be slowed down. In fact, when n_1 is held at a constant value independent of N, it follows from Theorem 4.1 that the stability margin is a constant independent of the total number of vehicles. More

generally, consider an information graph with $n_1 = O(N^c)$, where $c \in [0, 1]$ is a fixed constant. Using Theorem 4.1, it follows that $S = O(1/N^{2c})$ as $N \to \infty$. If $c < \frac{1}{D}$, the resulting reduction of S with N is slower than that obtained for a square lattice; cf. Corollary 4.1. This shows that within the class of D dimensional lattices (for a fixed D), certain information graphs provide better scaling of the stability margin than others. The price one pays for improving stability margin by reducing n_1 is an increase in the number of reference vehicles. This is because the number of reference vehicles N_r is related to n_1 by $N_r = N/N_1$ (see Assumption 4.2).

It is important to stress that not all non-square graphs are advantageous. For example, if $N_1 = O(N)$ and N_2 through N_D are $O(1)$, it follows from Theorem 4.1 that the stability margin is $S = O(1/N^2)$. This is the same trend as in a 1-D information graph. In this case, we can say that the D dimensional information graph effectively behaves as a one dimensional graph.

Figure 4-3 shows a few examples of information graph that are relevant to the discussion above. Figure 4-3 (a) shows a 2-dimensional information graph in which the first dimension is held constant, i.e. $N_1 = O(1)$ and $N_2 = O(N)$. Figure 4-3 (b) shows a 2-dimensional information graph that is "asymptotically" 1-D (as $N \to \infty$) since the size of the first dimension increases linearly with N, i.e. $N_1 = O(N)$ and $N_2 = O(1)$. Figure 4-3 (c) shows a 2-dimensional information graph in which both sides are of length $O(\sqrt{N})$.

Figure 4-4 provides numerical corroboration of stability margin predicted by Theorem 4.1 for a vehicle formation with information graphs of various "shapes" as shown in Figure 4-3. The legend "SSM" means computed from the "state space model" (4–10), which is presented in Section 4.2. For the first case, $N_1 = 5$ and $N_2 = N/5$. Theorem 4.1 predicts that in this case $S = O(1)$ even as $N \to \infty$, which results in a stability margin that is independent of N. In the second case, $N_2 = 5$ and $N_1 = N/5$, which leads to $S = O(1/N^2)$, which is the same as that with an 1-D information graph. The third case

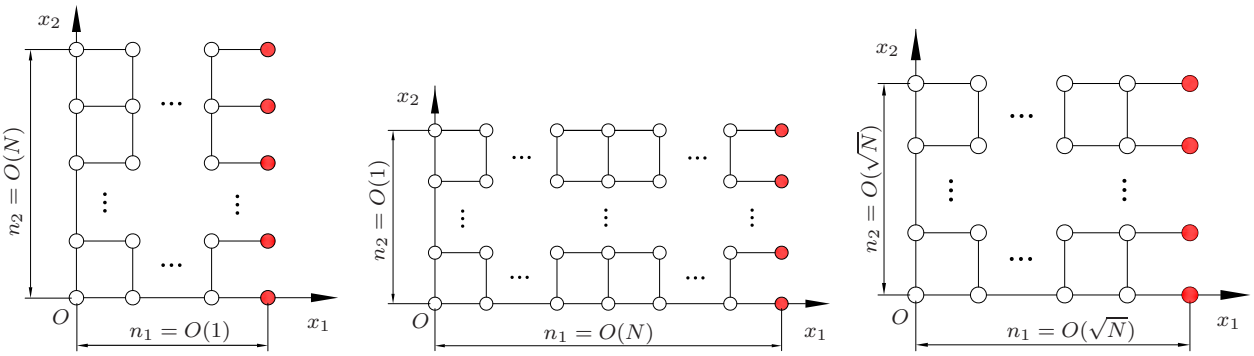

(a) Non-square information graph (b) Non-square information graph (c) Square information graph

Figure 4-3. Information graphs with different aspect ratios.

is that of a square information graph, $N_1 = N_2 = \sqrt{N}$, which leads to $S = O(1/N)$. Theorem 4.1 and corollary 4.1 predicts the stability margin quite accurately in each of the cases. The control gains used in all the calculations are $k_0 = 0.1$ and $b_0 = 0.5$. The stability margin as a function of N for three distinct 2D information graphs (that are described in Figure 4-3) are shown in this figure. The stability margin is computed by computing the eigenvalues of the closed-loop state matrix; the state space model is described in (4–10) in Section 4.2. The plots show that the formulae (4–6) in Theorem 4.1 and Corollary 4.1 make excellent predictions of the trend of stability margin.

4.1.3 Main Result 2: Scaling Laws for Disturbance Amplification

In this chapter, we only consider the all-to-all amplification, which is defined as the H_∞ norm of the transfer function from the disturbances on all the vehicles (except leaders) to their position tracking errors. The concept of leader-to-trailer has no direct physical meaning in the formation with D-dimensional information graph, so we ignore that case.

Theorem 4.2. *Consider an N-vehicle formation with vehicle dynamics (4–1) and control law (4–2), under Assumptions 4.1 and 4.2. With symmetric control, the all-to-all*

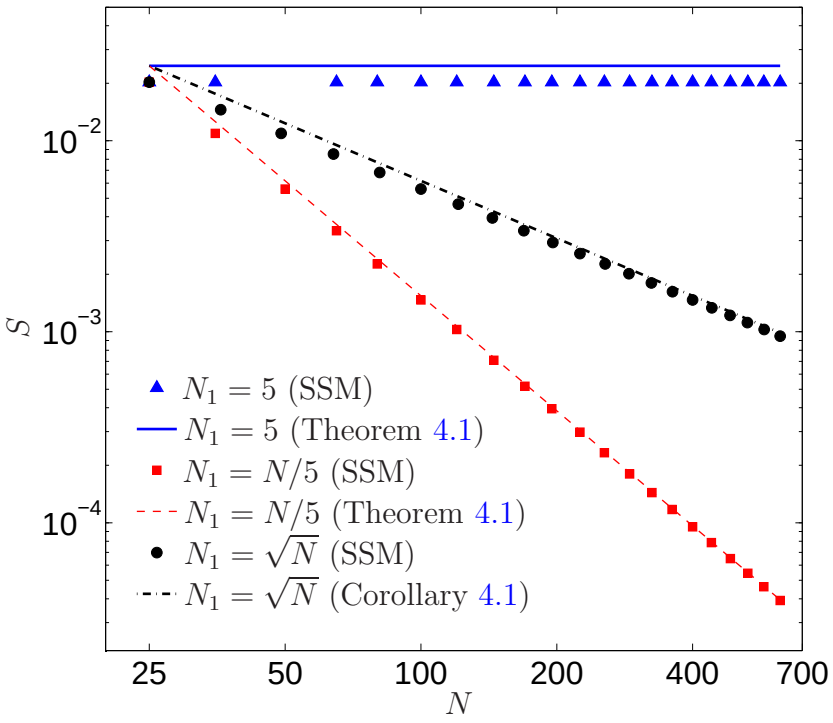

Figure 4-4. Numerical verification of stability margin

amplification and its peak frequency of the closed-loop are given by

$$H_{ATA} \approx \frac{8}{\sqrt{k_0} b_0 \pi^3} N_1^3, \quad \omega_r \approx \frac{\sqrt{k_0}\pi}{2} \frac{1}{N_1}. \tag{4–6}$$

□

Again, we see that the all-to-all amplification only depends on N_1, the number of real vehicles on the x_1 axis of the information graph. Thus, following the same argument for stability margin, we are able to design a non-square information graph with proper aspect ratio such that the scaling laws of the disturbance amplification grows much slower than N or is independent of N, the number of vehicles in the formation.

4.2 Closed-Loop Dynamics: State-Space and PDE Models

4.2.1 State-Space Model of the Controlled Vehicle Formation

The dynamics of the i-th vehicle is obtained by combining the open loop dynamics (4–1) with the control law (4–3), which yields

$$\ddot{p}_i = \sum_{j \in \mathcal{N}_i} -k_{(i,j)}(p_i - p_j - \Delta_{i,j}) - b_{(i,j)}(v_i - v_j) + w_i, \quad i = 1, \ldots, N. \tag{4–7}$$

Let $p_i^*(t)$ denote the desired trajectory of the i-th vehicle. The trajectory is uniquely determined from the trajectories of the reference vehicles and the desired formation geometry. For example, suppose the trajectory of a reference vehicle r is v^*t. If the d-th coordinate of the desired gap between a vehicle i and the reference vehicle r is $\Delta_{ir}^{(d)}$, then the d-th coordinate of the desired trajectory of i is $p^{*(d)}(t) = v^{*(d)}t + \Delta_{ir}^{(d)}$.

To facilitate analysis, we define the following coordinate transformation:

$$\tilde{p}_i := p_i - p_i^* \qquad \Rightarrow \qquad \dot{\tilde{p}}_i = \dot{p}_i - v^* = v_i - v^*. \tag{4–8}$$

Substituting (4–8) into (4–7), we have

$$\ddot{\tilde{p}}_i = \sum_{j \in \mathcal{N}_i} -k_{(i,j)}(\tilde{p}_i - \tilde{p}_j) - b_{(i,j)}(\dot{\tilde{p}}_i - \dot{\tilde{p}}_j) + w_i. \tag{4–9}$$

Since the trajectory of a reference vehicle is assumed to be equal to its desired trajectory, $\tilde{p}_i = 0$ if i is a reference vehicle. Using (4–9), the state-space model of the vehicle formation can now be written compactly as:

$$\dot{X} = AX + BW, \quad E = CX, \tag{4–10}$$

where X is the state vector, which is defined as $X := [\tilde{p}_1, \dot{\tilde{p}}_1, \cdots, \tilde{p}_N, \dot{\tilde{p}}_N] \in \mathbb{R}^{2N}$, W is input vector (external disturbances) and E is the output vector (position tracking errors).

Our goal is to analyze the closed-loop stability margin and disturbance amplification with increasing number of vehicles N. We approximate the dynamics of the spatially

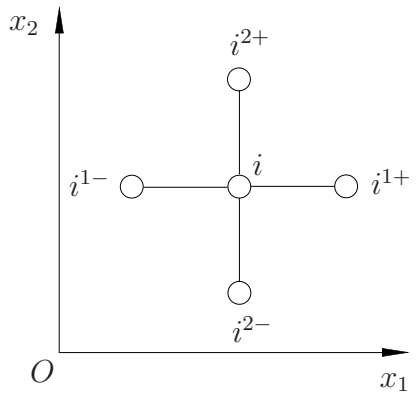

Figure 4-5. A pictorial representation of the i-th vehicle and its four nearby neighbors.

discrete formation by a partial differential equation (PDE) model that is valid for large values of N. This PDE model is used for analysis and control design.

4.2.2 PDE Model of the Controlled Vehicle Formation

For a given choice of the information graph, the i-th vehicle has the coordinate $\vec{i} = [i_1, i_2, \ldots, i_D]^T$ in $\mathbb{R}^D$. We interpret $\tilde{p}_i$ as a function of the coordinate $\vec{i}$. In the following, we consider a continuous approximation of this function to write a PDE model.

For the i-th node with coordinate $\vec{i} = [i_1, \ldots, i_D]^T$, we use i^{d+} and i^{d-} to denote the nodes with coordinates $[i_1, \ldots, i_{d-1}, i_d + 1, i_{d+1}, \ldots, i_D]^T$ and $[i_1, \ldots, i_{d-1}, i_d - 1, i_{d+1}, \ldots, i_D]^T$, respectively.

For $D = 2$, a node i in the interior of the graph and its four neighbors, i.e., i^{1+}, i^{1-},i^{2+}, and i^{2-}. Figure 4-5 shows a pictorial representation of the i-th vehicle and its four nearby neighbors in a 2D information graph. i^{1+} stands for the neighbor of the i-th vehicle in the x_1 positive direction relative to vehicle i, and i^{1-} stands for the neighbor of the i-th vehicle in the x_1 negative direction relative to vehicle i. And i^{2+} and i^{2-} can be interpreted in the same way.. The dynamics (4–9) can now be expressed as:

$$\begin{aligned}\ddot{\tilde{p}}_i = &- \sum_{d=1}^{D} k_{(i,i^{d+})}(\tilde{p}_i - \tilde{p}_{i^{d+}}) - \sum_{d=1}^{D} k_{(i,i^{d-})}(\tilde{p}_i - \tilde{p}_{i^{d-}}) \\ &- \sum_{d=1}^{D} b_{(i,i^{d+})}(\dot{\tilde{p}}_i - \dot{\tilde{p}}_{i^{d+}}) - \sum_{d=1}^{D} b_{(i,i^{d-})}(\dot{\tilde{p}}_i - \dot{\tilde{p}}_{i^{d-}}) + w_i. \end{aligned} \tag{4–11}$$

We define,

$$k_i^{d,f+b} := k_{(i,i^{d+})} + k_{(i,i^{d-})}, \qquad k_i^{d,f-b} := k_{(i,i^{d+})} - k_{(i,i^{d-})},$$
$$b_i^{d,f+b} := b_{(i,i^{d+})} + b_{(i,i^{d-})}, \qquad b_i^{d,f-b} := b_{(i,i^{d+})} - b_{(i,i^{d-})}, \tag{4–12}$$

where $d \in \{1, \ldots, D\}$; the superscripts f and b denote *front* and *back*, respectively. Substituting (4–12) into (4–11), we have

$$\begin{aligned}\ddot{\tilde{p}}_i = &- \sum_{d=1}^{D} \frac{k_i^{d,f+b} + k_i^{d,f-b}}{2}(\tilde{p}_i - \tilde{p}_{i^{d+}}) - \sum_{d=1}^{D} \frac{k_i^{d,f+b} - k_i^{d,f-b}}{2}(\tilde{p}_i - \tilde{p}_{i^{d-}}) \\ &- \sum_{d=1}^{D} \frac{b_i^{d,f+b} + b_i^{d,f-b}}{2}(\dot{\tilde{p}}_i - \dot{\tilde{p}}_{i^{d+}}) - \sum_{d=1}^{D} \frac{b_i^{d,f+b} - b_i^{d,f-b}}{2}(\dot{\tilde{p}}_i - \dot{\tilde{p}}_{i^{d-}}) + w_i. \end{aligned} \tag{4–13}$$

To proceed further, we first redraw the information graph in such a way so that it always lies in the unit D-cell $[0,1]^D$, irrespective of the number of vehicles. Note that in graph-theoretic terms, a graph is defined only in terms of its node and edge sets. A drawing of a graph in an Euclidean space, also called an embedding [93], is merely a convenient visualization tool. For the rest of this section, we will consider the following drawing (embedding) of the lattice $\mathbf{Z}_{n_1 \times \ldots n_D}$ in the Euclidean space $\mathbb{R}^D$. The Euclidean coordinate of the i-th node, whose "original" Euclidean position was $[i_1, \ldots, i_D]^T$, is now drawn at position $[i_1 c_1, i_2 c_2, \ldots, i_D c_D]^T$, where

$$c_d := \frac{1}{n_d - 1}, \quad d = 1, \ldots, D. \tag{4–14}$$

Figure 4-6 shows an example, where the original lattice, shown in Figure 4-6(a), is redrawn to fit into $[0,1]^2$, which is shown in Figure 4-6(b).

The starting point for the PDE derivation is to consider a function $\tilde{p}(x,t) : [0,1]^D \times [0, \infty) \to \mathbb{R}$ defined over the unit D-cell in $\mathbb{R}^D$ that satisfies:

$$\tilde{p}_i(t) = \tilde{p}(x,t)|_{x=[i_1 c_1, i_2 c_2, \ldots, i_D c_D]^T} \tag{4–15}$$

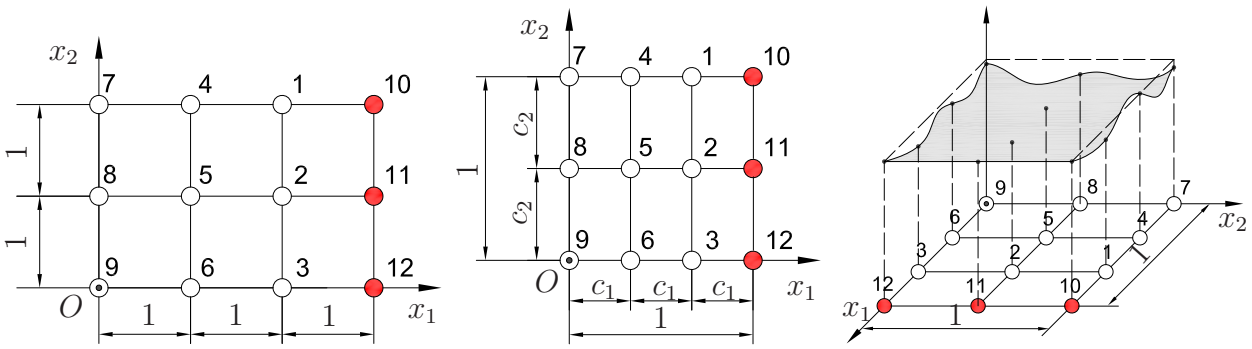

(a) Original lattice (b) Redrawn lattice (c) function approximation

Figure 4-6. Original lattice, its redrawn lattice and a continuous approximation.

Figure 4-6 pictorially depicts the approach: functions that are defined at discrete points (the vertices of the lattice drawn in $[0,1]^D$) will be approximated by functions that are defined everywhere in $[0,1]^D$. The original functions are thought of as samples of their continuous approximations. In figure 4-6, (a) is a 2D information graph for a formation with 3×3 vehicles and 3 reference vehicles. (b) shows a redrawn information graph of (a), so that it lies in the unit 2-cell $[0,1]^2$. (c) gives a pictorial representation of continuous approximation of a discrete function whose values are defined on the nodes in the redrawn lattice as shown in (b). We formally introduce the following scalar functions $k_d^f, k_d^b, b_d^f, b_d^b : [0,1]^D \to \mathbb{R}$ (for $d \in \{1,\ldots,D\}$) defined according to the stipulation:

$$
\begin{aligned}
k_{(i,i^{d+})} &= k_d^f(x)|_{x=[i_1c_1,i_2c_2,\ldots,i_Dc_D]^T}, & k_{(i,i^{d-})} &= k_d^b(x)|_{x=[i_1c_1,i_2c_2,\ldots,i_Dc_D]^T} \\
b_{(i,i^{d+})} &= b_d^f(x)|_{x=[i_1c_1,i_2c_2,\ldots,i_Dc_D]^T}, & b_{(i,i^{d-})} &= b_d^b(x)|_{x=[i_1c_1,i_2c_2,\ldots,i_Dc_D]^T} \\
a_{(i,i^{d+})} &= a(x)|_{x=[i_1c_1,i_2c_2,\ldots,i_Dc_D]^T}, & \theta_{(i,i^{d-})} &= \theta(x)|_{x=[i_1c_1,i_2c_2,\ldots,i_Dc_D]^T}.
\end{aligned}
\tag{4–16}
$$

In addition, we define functions $k_d^{f+b}, k_d^{f-b}, b_d^{f+b}, b_d^{f-b} : [0,1]^D \to \mathbb{R}$ as

$$
\begin{aligned}
k_d^{f+b}(x) &:= k_d^f(x) + k_d^b(x), & k_d^{f-b}(x) &:= k_d^f(x) - k_d^b(x), \\
b_d^{f+b}(x) &:= b_d^f(x) + b_d^b(x), & b_d^{f-b}(x) &:= b_d^f(x) - b_d^b(x).
\end{aligned}
\tag{4–17}
$$

Due to (4–16), these satisfy

$$k_i^{d,f+b} = k_d^{f+b}(x)|_{x=[i_1c_1,i_2c_2,\ldots,i_Dc_D]^{\mathrm{T}}}, \qquad k_i^{d,f-b} = k_d^{f-b}(x)|_{x=[i_1c_1,i_2c_2,\ldots,i_Dc_D]^{\mathrm{T}}},$$
$$b_i^{d,f+b} = b_d^{f+b}(x)|_{x=[i_1c_1,i_2c_2,\ldots,i_Dc_D]^{\mathrm{T}}}, \qquad b_i^{d,f-b} = b_d^{f-b}(x)|_{x=[i_1c_1,i_2c_2,\ldots,i_Dc_D]^{\mathrm{T}}}.$$

To obtain a PDE model from (4–13), we first rewrite it as

$$\begin{aligned}\ddot{\tilde{p}}_i =& \sum_{d=1}^{D} k_i^{d,f-b} c_d \frac{(\tilde{p}_{i^{d+}} - \tilde{p}_{i^{d-}})}{2c_d} + \sum_{d=1}^{D} \frac{k_i^{d,f+b}}{2} c_d^2 \frac{(\tilde{p}_{i^{d+}} - 2\tilde{p}_i + \tilde{p}_{i^{d-}})}{c_d^2} \\ &+ \sum_{d=1}^{D} b_i^{d,f-b} c_d \frac{(\dot{\tilde{p}}_{i^{d+}} - \dot{\tilde{p}}_{i^{d-}})}{2c_d} + \sum_{d=1}^{D} \frac{b_i^{d,f+b}}{2} c_d^2 \frac{(\dot{\tilde{p}}_{i^{d+}} - 2\dot{\tilde{p}}_i + \dot{\tilde{p}}_{i^{d-}})}{c_d^2} \\ &+ a_i \sin(\omega t + \theta_i). \end{aligned} \tag{4–18}$$

and then use the following finite difference approximations for every $d \in \{1, \ldots, D\}$:

$$\begin{aligned}\left[\frac{\tilde{p}_{i^{d+}} - \tilde{p}_{i^{d-}}}{2c_d}\right] &= \left[\frac{\partial \tilde{p}(x,t)}{\partial x_d}\right]_{x=[i_1c_1,i_2c_2,\ldots,i_Dc_D]^{\mathrm{T}}}, \\ \left[\frac{\tilde{p}_{i^{d+}} - 2\tilde{p}_i + \tilde{p}_{i^{d-}}}{c_d^2}\right] &= \left[\frac{\partial^2 \tilde{p}(x,t)}{\partial {x_d}^2}\right]_{x=[i_1c_1,i_2c_2,\ldots,i_Dc_D]^{\mathrm{T}}}, \\ \left[\frac{\dot{\tilde{p}}_{i^{d+}} - \dot{\tilde{p}}_{i^{d-}}}{2c_d}\right] &= \left[\frac{\partial^2 \tilde{p}(x,t)}{\partial x_d \partial t}\right]_{x=[i_1c_1,i_2c_2,\ldots,i_Dc_D]^{\mathrm{T}}}, \\ \left[\frac{\dot{\tilde{p}}_{i^{d+}} - 2\dot{\tilde{p}}_i + \dot{\tilde{p}}_{i^{d-}}}{c_d^2}\right] &= \left[\frac{\partial^3 \tilde{p}(x,t)}{\partial {x_d}^2 \partial t}\right]_{x=[i_1c_1,i_2c_2,\ldots,i_Dc_D]^{\mathrm{T}}}. \end{aligned}$$

We emphasize that $x_1, \ldots, x_D$ above are the coordinate directions in the Euclidean space in which the information graph is drawn, which are unrelated to the coordinate axes of the Euclidean space that the vehicles physically occupy. Substituting the expression (4–14) for c_d, (4–18) is seen as a finite difference approximation of the following PDE:

$$\begin{aligned}\frac{\partial^2 \tilde{p}(x,t)}{\partial t^2} = \sum_{d=1}^{D} \Big(& \frac{k_d^{f-b}(x)}{n_d - 1} \frac{\partial}{\partial x_d} + \frac{k_d^{f+b}(x)}{2(n_d-1)^2} \frac{\partial^2}{\partial {x_d}^2} + \frac{b_d^{f-b}(x)}{n_d - 1} \frac{\partial^2}{\partial x_d \partial t} \\ & + \frac{b_d^{f+b}(x)}{2(n_d-1)^2} \frac{\partial^3}{\partial {x_d}^2 \partial t} \Big) \tilde{p}(x,t) + a(x) \sin(\omega t + \theta(x)). \end{aligned} \tag{4–19}$$

The boundary conditions of PDE (4–19) depend on the arrangement of reference vehicles in the information graph. If there are reference vehicles on the boundary, the boundary

condition is of Dirichlet type. If there are no reference vehicles, the boundary condition is of the Neumann type.

Under Assumption 4.2, the boundary conditions are of the Dirichlet type on that face of the unit cell where the reference vehicles are, and Neumann on all other faces:

$$\begin{aligned}&\tilde{p}(1, x_2, \ldots, x_D, t) = 0, \quad \frac{\partial \tilde{p}}{\partial x_1}(0, x_2, \ldots, x_D, t) = 0,\\ &\frac{\partial \tilde{p}}{\partial x_d}(x, t) = 0, \quad x = [x_1, \ldots, x_{d-1}, 0 \text{ or } 1, x_{d+1}, \ldots, x_D]^T, \quad (d > 1).\end{aligned} \tag{4–20}$$

If other arrangements of reference vehicles are used, the boundary conditions may be different. It can be verified in a straightforward manner that the PDE (4–19) yields the original set of coupled ODEs (4–11) upon finite difference discretization, see [77, 86].

4.3 Analysis of Stability Margin and Disturbance Amplification

In this section, we consider the following homogeneous and symmetric control gains

$$k_{(i,j)} = k_0, \qquad b_{(i,j)} = b_0, \qquad \forall (i,j) \in \mathbf{E},$$

where k_0 and b_0 are positive scalars. In this case, using the notation in (4–12) and (4–16), we have

$$k_d^{f+b}(x) = 2k_0, \quad k_d^{f-b}(x) = 0, \quad b_d^{f+b}(x) = 2b_0, \quad b_d^{f-b}(x) = 0, \quad d = 1, \ldots, D.$$

The PDE given in (4–19) without forcing simplifies to:

$$\frac{\partial^2 \tilde{p}(x,t)}{\partial t^2} = \sum_{d=1}^{D} \Big(\frac{k_0}{(n_d - 1)^2} \frac{\partial^2}{\partial {x_d}^2} + \frac{b_0}{(n_d - 1)^2} \frac{\partial^3}{\partial {x_d}^2 \partial t} \Big) \tilde{p}(x,t). \tag{4–21}$$

The closed-loop eigenvalues of the PDE model require consideration of the eigenvalue problems

$$\mathcal{L}\eta(x) = -\lambda \eta(x), \tag{4–22}$$

where the linear operator $\mathcal{L}$ is defined as:

$$\mathcal{L} = \sum_{d=1}^{D} \frac{1}{(n_d - 1)^2} \frac{\partial^2}{\partial {x_d}^2}, \tag{4–23}$$

and η is an eigenfunction that satisfies the boundary condition (4–20) under Assumption 4.2. For this boundary condition, the eigenvalues (note that they are different from the eigenvalues of the PDE model) and eigenfunctions are obtained by the method of separation of variables ([77, 86])

$$\begin{aligned}
\lambda_\ell &= \Big(\frac{(2\ell_1 - 1)\pi}{2(n_1 - 1)}\Big)^2 + \frac{(\ell_2 \pi)^2}{(n_2 - 1)^2} + \cdots + \frac{(\ell_D \pi)^2}{(n_D - 1)^2} \\
&= \pi^2 \Big(\frac{(2\ell_1 - 1)^2}{4(n_1 - 1)^2} + \frac{\ell_2^2}{(n_2 - 1)^2} + \cdots + \frac{\ell_D^2}{(n_d - 1)^2}\Big), \\
\eta_\ell(x) &= \cos\Big(\frac{(2\ell_1 - 1)\pi x_1}{2}\Big) \cos(\ell_2 \pi x_2) \cdots \cos(\ell_D \pi x_D),
\end{aligned} \tag{4–24}$$

where we use the notation $\ell = (\ell_1, \cdots, \ell_D)$ to denote the wave vector in which $\ell_1 \in \{1, 2, \cdots\}$ and $\ell_2, \cdots, \ell_D \in \{0, 1, 2, \cdots\}$. After taking a Laplace transform of both sides of the PDE (4–21) with respect to t, and using the method of separation of variables, the eigenvalues of the PDE turn out to be the roots of the characteristic equation:

$$s^2 + b_0 \lambda_\ell s + k_0 \lambda_\ell = 0, \tag{4–25}$$

where s is the Laplace variable and λ_ℓ is the eigenvalue in (4–24).

The two roots of (4–25) are

$$s_\ell^{\pm} := \frac{-b_0 \lambda_\ell \pm \sqrt{b_0^2 \lambda_\ell^2 - 4 k_0 \lambda_\ell}}{2}. \tag{4–26}$$

We call $s_\ell^{\pm}$ the ℓ-th pair of eigenvalues.

Provided each of the n_d's are large so that the PDE (4–19) with the boundary condition (4–20) is an accurate approximation of the (spatially) discrete formation dynamics (4–10) under Assumption 4.2, the least stable eigenvalue of the PDE (4–21)

provides information on the stability margin of the closed-loop formation dynamics. We are now ready to prove Theorem 4.1 that was stated in Section 4.1.

Proof of Theorem 4.1. Consider the eigenvalue problem for PDE (4–21) with mixed Dirichlet and Neumann boundary conditions (4–20). Let's first examine the discriminant in (4–26),

$$\begin{aligned} D := b_0^2\lambda_\ell^2 - 4k_0\lambda_\ell =& \pi^4 b_0^2\Big(\frac{(2\ell_1-1)^2}{4(n_1-1)^2} + \frac{\ell_2^2}{(n_2-1)^2} + \cdots + \frac{\ell_D^2}{(n_d-1)^2}\Big)^2 \\ & - 4\pi^2 k_0\Big(\frac{(2\ell_1-1)^2}{4(n_1-1)^2} + \frac{\ell_2^2}{(n_2-1)^2} + \cdots + \frac{\ell_D^2}{(N_d-1)^2}\Big), \end{aligned}$$

Under the assumption n_d ($d = 1, \ldots, D$) are very large, for small ℓ_d, D is negative. So both the eigenvalues in (4–26) are complex, then the stability margin is only determined by the real parts of $s_\ell^\pm$. For large ℓ_d, D is positive, so both the eigenvalues in (4–26) are real. It is easy to verify that the real part in this case are much larger than that with negative discriminant D. Therefore, we only consider the case when the eigenvalues are complex.

It follows from (4–26) that the least stable eigenvalues $s_{\min}$ (the ones closest to the imaginary axis) among them is the one that is obtained by minimizing λ_ℓ over the D-tuples $(\ell_1, \ldots, \ell_D)$. Using (4–24), this minimum is achieved at $\ell_1 = 1, \ell_2 = \cdots = \ell_D = 0$,

$$s_{\min} = s^\pm_{(1,0,\ldots,0)},$$

and the real part is obtained

$$Re(s_{\min}) = -\frac{b_0\lambda_\ell}{2} = -\frac{\pi^2 b_0}{8(n_1-1)^2}.$$

Following the definition of stability margin,

$$S := |Re(s_{\min})| = \frac{\pi^2 b_0}{8(n_1-1)^2} = \frac{\pi^2 b_0}{8N_1^2}, \tag{4–27}$$

where the last equality following from $N_1 = n_1 - 1$. □

We now prove Theorem 4.2 that was stated in Section 4.1.

Proof of Theorem 4.2. We first observe that the smallest eigenvalue of the operator $\mathcal{L}$ given in (4–23) is obtained by minimizing λ_ℓ over the D-tuples $(\ell_1, \ldots, \ell_D)$. Using (4–24), this minimum is achieved at $\ell_1 = 1, \ell_2 = \cdots = \ell_D = 0$,

$$\lambda_{\min} = \lambda_{(1,0,\ldots,0)} = \frac{\pi^2}{4(n_1-1)^2} = \frac{\pi^2}{4N_1^2},$$

where the last equality following from $N_1 = n_1 - 1$.

We now write the PDE model with external disturbances as

$$\frac{\partial^2 \tilde{p}(x,t)}{\partial t^2} = \sum_{d=1}^{D} \Big(\frac{k_0}{(n_d-1)^2} \frac{\partial^2}{\partial {x_d}^2} + \frac{b_0}{(n_d-1)^2} \frac{\partial^3}{\partial {x_d}^2 \partial t} \Big) \tilde{p}(x,t) + u(x,t),$$

where $u(x,t) = a(x)\sin(\omega t + \theta(x))$ is the external sinusoidal disturbance. Take Laplace transform to both sides of the above PDE with respect to the time variable t, we get

$$s^2 P(x,s) = \sum_{d=1}^{D} \Big(\frac{k_0}{(n_d-1)^2} \frac{\partial^2 P(x,s)}{\partial {x_d}^2} + \frac{b_0 s}{(n_d-1)^2} \frac{\partial^2 P(x,s)}{\partial {x_d}^2} \Big) + U(x,s), \tag{4–28}$$

where s is the Laplace variable and $P(x,s), U(x,s)$ are the Laplace transforms of $\tilde{p}(x,t)$ and $u(x,t)$ respectively. Using the method of separation of variables, we assume a solution of the form $P(x,s) = \eta(x)h(s)$, where $\eta(x)$ is the eigenfunction of the linear operator $\mathcal{L}$. Substituting $P(x,s) = \eta(x)h(s)$ into (4–28), we get

$$s^2 \eta(x) h(s) = \sum_{d=1}^{D} \Big(\frac{k_0}{(n_d-1)^2} \frac{\partial^2 \eta(x)}{\partial {x_d}^2} + \frac{b_0 s}{(n_d-1)^2} \frac{\partial^2 \eta(x)}{\partial {x_d}^2} \Big) h(s) + U(x,s),$$

Now, substituting $\mathcal{L}\eta(x) = -\lambda_\ell \eta(x)$ into the above equation, we have

$$s^2 \eta(x) h(s) = (-k_0 \lambda_\ell - b_0 \lambda_\ell s) \eta(x) h(s) + U(x,s),$$

which implies

$$(s^2 + k_0 \lambda_\ell + b_0 \lambda_\ell s) P(x,s) = U(x,s),$$

We thus obtain the following transfer function from $U(x,s)$ to $P(x,s)$ (see [94])

$$G(s) = \frac{P(x,s)}{U(x,s)} = \frac{1}{s^2 + b_0\lambda_\ell s + k_0\lambda_\ell}, \tag{4–29}$$

where λ_ℓ is the ℓ-th eigenvalue of the linear operator $\mathcal{L}$, it is given in (4–24). Similar to finite-dimensional system, the H_∞ norm of a transfer function is given by the supremum of the square root of the largest eigenvalue of $G(j\omega)^* G(j\omega)$, we have

$$\begin{aligned}\|G(j\omega)\|_{H_\infty} &= \sqrt{\sup_\omega \sup_\ell \frac{1}{-\omega^2 - b_0\lambda_\ell j\omega + k_0\lambda_\ell} \frac{1}{-\omega^2 + b_0\lambda_\ell j\omega + k_0\lambda_\ell}} \\ &= \sup_\omega \sup_\ell \frac{1}{\sqrt{(k_0\lambda_\ell - \omega^2)^2 + (b_0\lambda_\ell\omega)^2}} = \sup_\ell A_\ell. \end{aligned} \tag{4–30}$$

where

$$A_\ell = \begin{cases} \frac{2}{\lambda_\ell^{3/2} b_0 \sqrt{4k_0 - \lambda_\ell b_0^2}}, & \text{if } \lambda_\ell \le 2k_0/b_0^2, \\ \frac{1}{\lambda_\ell k_0}, & \text{otherwise.} \end{cases} \tag{4–31}$$

$$\omega_\ell = \begin{cases} \frac{\sqrt{4\lambda_\ell k_0 - 2\lambda_\ell^2 b_0^2}}{2}, & \text{if } \lambda_\ell \le 2k_0/b_0^2, \\ 0, & \text{otherwise.} \end{cases} \tag{4–32}$$

For any fixed k_0, b_0, when n_d is large, we have $\lambda_\ell \le 2k_0/b_0^2$. The H_∞ norm and the peak frequency of the transfer function $G(s)$ are given by

$$\|G(j\omega)\|_{H_\infty} = A_{(1,0,\cdots)} = \frac{2}{\lambda_{\min}^{3/2} b_0 \sqrt{4k_0 - \lambda_{\min} b_0^2}}, \tag{4–33}$$

$$\omega_r = \frac{\sqrt{4\lambda_{\min} k_0 - 2\lambda_{\min}^2 b_0^2}}{2}. \tag{4–34}$$

Recall that $\lambda_{\min} = \frac{\pi^2}{4(n_1-1)^2} = \frac{\pi^2}{4N_1^2}$, use the assumption that n_d is large, we finish the proof. Similar proof based on the state-space model (4–10) can be found in [88, 95]. □

4.4 Summary

We studied the problem of distributed control of a large formation of vehicle teams with D-dimensional information graph. We showed that the stability margin scales as

$O(1/N^{2/D})$ and the all-to-all amplification scales as $O(N^{3/D})$ for a D-dimensional square information graph. Therefore, increasing the dimension of the information graph can improve the stability margin and robustness to external disturbances by a considerable amount. For non-square information graph, the stability margin and all-to-all amplification can be made independent of the number of agents by choosing the "aspect ratio" appropriately. However, it should be taken into account that increasing the dimension of the information graph or choosing a beneficial aspect ratio may require long range communication or entail an increase in the number of lead vehicles. These results are therefore useful to the designer in making trade-offs between performance and cost in designing information exchange architectures for decentralized control.

Our results for square D-lattices are complementary to those of [90], in which the effect of graph dimension on the response of the closed loop to stochastic disturbances is quantified in terms of "microscopic" and "macroscopic" measures. It was shown in [90] that for $D > 3$, these performance measures become independent of N, while for smaller D, the performance becomes worse without bound as the number of vehicles increase. In contrast, we showed that the stability margin decays to 0 and all-to-all amplification increase to ∞ as N increases in every D. Though the decay is slower for larger D, it is never independent of N. To achieve a size-independent stability margin and all-to-all amplification, the graph needs to be non-square. Since the analysis of [90] is done in the spatial Fourier domain, it is not clear if non-square lattices with boundaries can be handled in that framework.

CHAPTER 5
IMPROVING CONVERGENCE RATE OF DISTRIBUTED CONSENSUS THROUGH ASYMMETRIC WEIGHTS

Study of consensus has a long history in systems and control theory as well as computer science. Early works can be dated back to the 1960s (see [96] and the references therein). Distributed consensus has been widely studied in the past few decades due to its broad applications in distributed computing, multi-vehicle rendezvous, data fusion in large sensor network, coordinated control of multi-agent system and formation flight of unmanned vehicles and clustered satellites, etc. (see [1, 5, 9–11, 97, 98]). In distributed consensus, each agent in a network updates its state by using a weighted summation of its own state and the states of its neighbors so that all the agents' states will reach a common value.

The topic of this chapter is the convergence rate of distributed linear consensus protocol on graphs with fixed (time invariant) topology. We study how to design the graph weights to improve the convergence rate of distributed consensus protocol. The convergence rate is extremely important, since it determines practical applicability of the protocol. If the convergence rate is too small, it will take extremely large number of iterations to drive the states of all agents sufficiently close. This is unfavorable for agents such as wireless sensors who have limited battery lifetimes.

Compared to the vast literature on design of consensus protocols, however, the literature on convergence rate analysis is meager. A few works can be found in [70–72, 99, 100]. The related problem of mixing time of Markov chains is studied in [73]. In [36], convergence rates for a specific class of graphs, that we call L-Z geometric graphs, are established as a function of the number of agents. Generally speaking, the convergence rates of distributed consensus algorithms tend to be slow, and decrease as the number of agents increases. It was shown in [74] that the convergence rate can be arbitrarily fast in small-world networks. However, networks in which communication is only possible between agents that are close enough are not likely to be small-world.

One of the seminal works on this subject is convex optimization of weights on edges of the graph to maximize the consensus convergence rate [27, 29]. Convex optimization imposes the constraint that the weights of the graph must be symmetric, which means any two neighboring agents put equal weight on the information received from each other. The convergence rate of consensus protocols on graphs with symmetric weights degrades considerably as the number of agents in the network increases. In a D-dimensional lattice, for instance, the convergence rate is $O(1/N^{2/D})$ if the weights are symmetric, where N is the number of agents. This result follows as a special case of the results in [36]. Thus, the convergence rate becomes arbitrarily small if the size of the network grows without bound.

In [75, 76], finite-time distributed consensus protocols are proposed to improve the performance over asymptotic consensus. However, in general, the finite time needed to achieve consensus depends the number of agents in the network. Thus, for large size of networks, although consensus can be achieved in finite time, the time needed to reach consensus becomes large.

In this chapter, we study the problem of how to increase the convergence rate of consensus protocols by designing *asymmetric* weights on edges. We first consider lattice graphs and derive precise formulae for convergence rate in these graphs. In particular, we show that in lattice graphs, with proper choice of asymmetric weights, the convergence rate of distributed consensus can be bounded away from zero uniformly in N. Thus, the proposed asymmetric design makes distributed consensus highly scalable; the time to reach consensus is now independent of the number of agents in the network. By time to reach consensus we mean the time needed for the states of all nodes to reach an ϵ neighborhood of the asymptotic consensus value. We provide the formulae for asymptotic steady-state consensus value. With asymmetric weights, the consensus value in general is not the average of the initial conditions.

We next propose a weight design scheme for arbitrary 2-dimensional geometric graphs, i.e., graphs consisting of nodes in $\mathbb{R}^2$. Here we use the idea of continuum approximation to extend the asymmetric design from lattices to geometric graphs. We show how a Sturm-Liouville operator can be used to approximate the graph Laplacian in the case of lattices. The spectrum of the Laplacian and the convergence rate of consensus protocols are intimately related. The discrete weights in lattices can be seen as samples of a continuous weight function that appears in the S-L operator. Based on this analogy, a weight design algorithm is proposed in which a node i chooses the weight on the edge to a neighbor j depending on the relative angle between i and j. Numerical simulations show that the convergence rate with asymmetric designed weights in large graphs is an order of magnitude higher than that with (i) optimal symmetric weights, which are obtained by convex optimization [27, 29], and (ii) asymmetric weights obtained by Metropolis-Hastings method, which assigns weights uniformly to each edge connecting itself to its neighbor. The proposed weight design method is decentralized, every node can obtain its own weight based on the angular position measurements with its neighbors. In addition, it is computationally much cheaper than obtaining the optimal symmetric weights using convex optimization method. The proposed weight design method can be extended to geometric graphs in $\mathbb{R}^D$, but in this chapter we limit ourselves to $\mathbb{R}^2$.

The rest of this chapter is organized as follows. Section 5.1 presents the problem statement. Results on size-independent convergence rate on lattice graphs with asymmetric weight are stated in Section 5.2. Asymmetric weight design method for more general graphs appear in Section 5.3. The chapter ends with a summary in Section 5.4.

5.1 Problem Formulation

To study the problem of distributed linear consensus in networks, we first introduce some terminologies. The network of N agents is modeled by a graph $\mathbf{G} = (\mathbf{V}, \mathbf{E})$ with vertex set $\mathbf{V} = \{1, \ldots, N\}$ and edge set $\mathbf{E} \subset \mathbf{V} \times \mathbf{V}$. We use (i, j) to represent a directed edge from i to j. A node i can receive information from j if and only if $(i, j) \in \mathbf{E}$. In

this chapter, we assume that communication is bidirectional, i.e. $(i,j) \in \mathbf{E}$ if and only if $(j,i) \in \mathbf{E}$. For each edge $(i,j) \in \mathbf{E}$ in the graph, we associate a weight $W_{i,j} > 0$ to it. The set of neighbors of i is defined as $\mathcal{N}_i := \{j \in \mathbf{V} : (i,j) \in \mathbf{E}\}$. The Laplacian matrix L of an arbitrary graph $\mathbf{G}$ with edge weights $W_{i,j}$ is defined as

$$L_{i,j} = \begin{cases} -W_{i,j} & i \neq j, (i,j) \in \mathbf{E}, \\ \sum_{k=1}^{N} W_{i,k} & i = j, (i,k) \in \mathbf{E}, \\ 0 & \text{otherwise.} \end{cases} \tag{5–1}$$

A linear consensus protocol is an iterative update law:

$$x_i(k+1) = W_{i,i}\, x_i(k) + \sum_{j \in \mathbb{N}_i} W_{i,j}\, x_j(k), \quad i \in \mathbf{V}, \tag{5–2}$$

with initial conditions $x_i(0) \in \mathbb{R}$, where $k = \{0, 1, 2, \cdots\}$ is the discrete time index. Following standard practice we assume the weight matrix W is a stochastic matrix, i.e. $W_{i,j} \geq 0$ and $W\mathbf{1} = \mathbf{1}$, where $\mathbf{1}$ is a vector with all entries of 1. The distributed consensus protocol (5–2) can be written in the following compact form:

$$x(k+1) = Wx(k), \tag{5–3}$$

where $x(k) = [x_1(k), x_2(k), \cdots, x_N(k)]^T$ is the states of the N agents at time k. It's straightforward to obtain the following relation $L = I - W$, where I is the $N \times N$ identity matrix and L is the Laplacian matrix associated with the graph with $W_{i,j}$ as its weights on the directed edge (i,j). In addition, their spectra are related by $\sigma(L) = 1 - \sigma(W)$, i.e. $\mu_\ell(L) = 1 - \lambda_\ell(W)$, where $\ell \in \{1, 2, \cdots, N\}$ and μ_ℓ, λ_ℓ are the eigenvalues of L and W respectively. The linear distributed consensus protocol (5–3) implies $x(k) = W^k x(0)$. We assume W is strongly connected (irreducible) and primitive. In that case the spectral radius of W is 1 and there is exactly one eigenvalue on the unit disk. Let $\pi \in \mathbb{R}^{1\times N}$ be the left Perron vector of W corresponding to the eigenvalue of 1, i.e. $\pi W = \pi$, $\pi_i > 0$ and

$\sum_{i=1}^{N} \pi_i = 1$, we have

$$\lim_{k\to\infty} W^k = \mathbf{1}\pi, \tag{5–4}$$

Therefore, all the states of the N agents asymptotically converge to a steady state value $\bar{x}$ as $k \to \infty$,

$$\lim_{k\to\infty} x(k) = \mathbf{1}\pi x(0) = \mathbf{1}\bar{x}, \tag{5–5}$$

where $\bar{x} = \sum_{i=1}^{N} \pi_i x_i(0)$.

It is well known that for a primitive stochastic matrix, the rate of convergence R can be measured by the spectral gap $R = 1 - \rho(W)$, where $\rho(W)$ is the essential spectral radius of W, which is defined as

$$\rho(W) := \max\{|\lambda| : \lambda \in \sigma(W) \setminus \{1\}\}.$$

If the eigenvalues of W are real and they are ordered in a non-increasing fashion such that $1 = \lambda_1 \geq \lambda_2 \geq \cdots \geq \lambda_N$, then the convergence rate of W is given by

$$R = 1 - \rho(W) = \min\{1 - \lambda_2, 1 + \lambda_N\}. \tag{5–6}$$

In addition, from Gerschgorin circle theorem, we have that $\lambda_N \geq -1 + 2\max_i W_{ii}$. If $\max_i W_{ii} \neq 0$, then $1 + \lambda_N$ is a constant bounded away from 0. Therefore, the key to find a lower bound for the convergence rate of W is to find an upper bound on the second largest eigenvalue λ_2 of W. Equivalently, we can find a lower bound of the second smallest eigenvalue μ_2 of the associated Laplacian matrix L, since $\mu_2 = 1 - \lambda_2$.

Definition 5.1. *We say a graph* $\mathbf{G}$ *has* symmetric *weights if* $W_{i,j} = W_{j,i}$ *for each pair of neighboring agents* $(i, j) \in \mathbf{E}$. *Otherwise, the weights are called* asymmetric. □

If the weights are symmetric, the matrix W is doubly stochastic, meaning that each row and column sum is 1.

The following theorem summaries the results in [36] on the convergence rate of consensus with symmetric weights in a broad class of graphs that include lattices. A D-dimensional lattice, specifically a $N_1 \times N_2 \times \cdots \times N_D$ lattice, is a graph with $N = N_1 \times N_2 \times \cdots \times N_D$ nodes, in which the nodes are placed at the integer unit coordinate points of the D-dimensional Euclidean space and each node connects to other nodes that are exactly one unit away from it. A D-dimensional lattice is drawn in $\mathbb{R}^D$ with a Cartesian reference frame whose axes are denoted by $x_1, x_2, \cdots, x_D$. We call a graph is a *L-Z geometric graph* if it can be seen as a perturbation of regular lattice in D-dimensional space; each node connects other nodes within a certain range. The formal definition is given in [36].

Theorem 5.1 ([36]). *Let* $\mathbf{G}$ *be a* D*-dimensional connected L-Z geometric graph or lattice and let* W *be any doubly stochastic matrix compatible with* $\mathbf{G}$*. Then*

$$\frac{c_1}{N^{2/D}} \leq R \leq \frac{c_2}{N^{2/D}}, \tag{5–7}$$

where N *is the number of nodes in the graph* $\mathbf{G}$ *and* c_1, c_2 *are some constants independent of* N*.* □

The above theorem states that for any connected L-Z geometric/lattice graph $\mathbf{G}$, the convergence rate of consensus with symmetric weights cannot be bounded away from 0 uniformly with the size N of the graph. The convergence rate of the network becomes arbitrarily slow as N increases without bound. The loss of convergence rate with symmetric information graph has also been observed in vehicular formations; as discussed in Chapter 2 and Chapter 4. In fact, another important conclusion of the result above is that heterogeneity in weights among nodes, as long as W is symmetric, does not change the asymptotic scaling of the convergence rate. At best it can change the constant in front of the scaling formula (see [73] also). Therefore, even centralized weight optimization scheme proposed in [27, 29] - that constrain the weights to be symmetric in order to make the optimization problem convex - will suffer from the same issue as that of

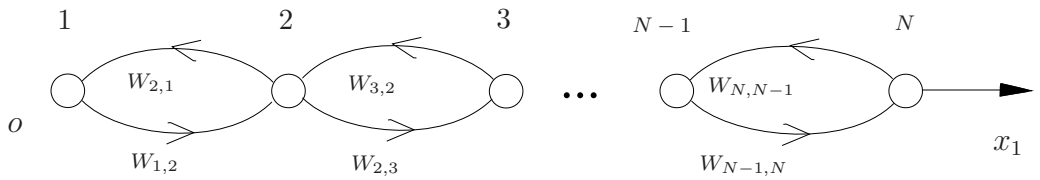

Figure 5-1. Information graph for a 1-D lattice of N agents.

un-optimized weights on the edges. Namely, the convergence rate will decay as $O(1/N^{2/D})$ in a D-dimensional lattice/L-Z geometric graph even with the optimized weights. In the rest of the chapter, we study the problem of speeding up the convergence rate by designing *asymmetric* weights.

5.2 Fast Consensus on D-dimensional Lattices

First we establish technical results on the spectrum and Perron vectors of D-dimensional lattices with possibly asymmetric weights on the edges. We then summarize their design implications at the end of section 5.2.1.

5.2.1 Asymmetric Weights in Lattices

We first consider distributed consensus on a 1-dimensional lattice. This will be useful in generalizing to D-dimensional lattices. Each agent interacts with its nearest neighbors in the lattice (one on each side). Its information graph is depicted in Figure 5-1. The updating law of agent i is given by

$$x_i(k+1) = W_{i,i}x_i(k) + W_{i,i-1}x_{i-1}(k) + W_{i,i+1}x_{i+1}(k).$$

where $i \in \{2, 3, \cdots, N-1\}$. The updating laws of the 1-st and N-th agents are slightly different from the above equation, since they only have one neighbor each.

The weight matrix $W^{(1)}$ for the 1-dimensional lattice is tridiagonal:

$$W^{(1)} = \begin{bmatrix} W_{1,1} & W_{1,2} & & & \\ W_{2,1} & W_{2,2} & W_{2,3} & & \\ & \ddots & \ddots & & \\ & W_{N-1,N-2} & W_{N-1,N-1} & W_{N-1,N} \\ & & W_{N,N-1} & W_{N,N} \end{bmatrix}.$$

The following lemma gives the spectrum and the left-hand Perron vector for the weight matrix $W^{(1)}$. The proof of the lemma is given in Section 5.5..

Lemma 5.1. *Let $W^{(1)}$ be the weight matrix associated with the 1-dimensional lattice with the weights given by $W_{i,i+1} = c, W_{i+1,i} = a$, where $a \neq c$ are positive constants and $a + c \leq 1$. Then the eigenvalues of $W^{(1)}$ are*

$$\lambda_1 = 1, \quad \lambda_\ell = 1 - a - c + 2\sqrt{ac}\cos\frac{(\ell-1)\pi}{N},$$

where $\ell \in \{2, \cdots, N\}$, and its left Perron vector is

$$\pi = \frac{1 - c/a}{1 - (c/a)^N}[1, c/a, (c/a)^2, \cdots, (c/a)^{N-1}]. \qquad \square$$

We next consider consensus on a D-dimensional lattice with the following weights

$$W_{i,i^{d+}} = c_d, \quad W_{i,i^{d-}} = a_d, \quad d \in \{1, \cdots, D\}, \tag{5–8}$$

where $a_d \neq c_d$ are positive constants and $\sum_{d=1}^{D} a_d + c_d \leq 1$. The notation i^{d+} denotes the neighbor on the positive x_d axis of node i and i^{d-} denotes the neighbor on the negative x_d axis of node i. For example, 2^{1+} and 2^{1-} in Figure 5-2 denote node 3 and node 1, respectively, and 2^{2+} is node 5.

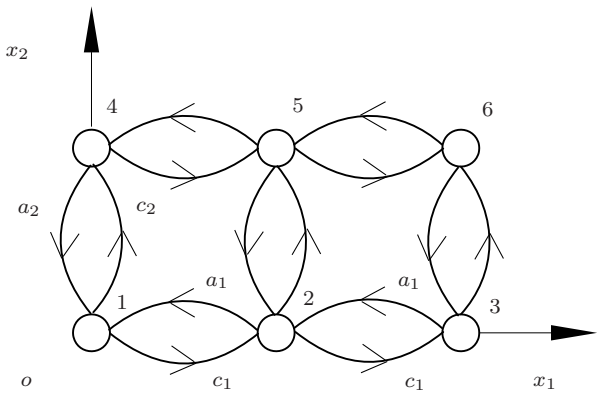

Figure 5-2. A pictorial representation of a 2-dimensional lattice information graph with the weights $W^{(2)}_{i,i^{d+}} = c_d, W^{(2)}_{i,i^{d-}} = a_d$, where $d = 1, 2$.

Lemma 5.2. *Let $W^{(D)}$ be the weight matrix associated with the D-dimensional lattice with the weights given in (5–8). Then its eigenvalues are given by*

$$\lambda_{\vec{\ell}}\,(W^{(D)}) = 1 - \sum_{d=1}^{D}(1 - \lambda_{\ell_d}(W_d^{(1)})),$$

where $\vec{\ell} = (\ell_1, \ell_2, \cdots, \ell_D)$, in which $\ell_d \in \{1, 2, \cdots, N_d\}$ and $W_d^{(1)}$ is the $N_d \times N_d$ weight matrix associated with a 1-dimensional lattice with the weights given by $W_d^{(1)}(i, i+1) = c_d, W_d^{(1)}(i+1, i) = a_d$ and $i \in \{1, \cdots, N_d - 1\}$. Its left Perron vector is $\pi = \pi_D^{(1)} \otimes \pi_{D-1}^{(1)} \otimes \cdots \otimes \pi_1^{(1)}$, where $\pi_d^{(1)}$ is the left Perron vector of $W_d^{(1)}$, and $\otimes$ denotes the Kronecker product. □

The proof of Lemma 5.2 is given in Section 5.5. The next theorem shows the implications of the preceding technical results on the convergence rate in D-dimensional lattices.

Theorem 5.2. *Let $\mathbf{G}$ be a D-dimensional lattice graph and let $W^{(D)}$ be an asymmetric stochastic matrix compatible with $\mathbf{G}$ with the weights given in (5–8). Then the convergence rate satisfies*

$$R \geq c_0, \tag{5–9}$$

where $c_0 \in (0, 1)$ is a constant independent of N. □

Proof of Theorem 5.2. According to Lemma 5.1, the eigenvalues of $W_d^{(1)}$ (defined in Lemma 5.2) are given by:

$$\lambda_1(W_d^{(1)}) = 1,$$
$$\lambda_\ell(W_d^{(1)}) = 1 - a_d - c_d + 2\sqrt{a_d c_d}\cos\frac{(\ell_d - 1)\pi}{N_d}.$$

From Lemma 5.2, the second largest eigenvalue $\lambda_2(W^{(D)})$ and the smallest eigenvalue $\lambda_N(W^{(D)})$ of $W^{(D)}$ are given by

$$\begin{aligned}
\lambda_2(W^{(D)}) &= 1 - \max_{d\in\{1,\cdots,D\}}(1 - \lambda_2(W_d^{(1)})) \\
&\le 1 - \max_{d\in\{1,\cdots,D\}}(a_d + c_d - 2\sqrt{a_d c_d}), \qquad (5\text{–}10) \\
\lambda_N(W^{(D)}) &= 1 - \sum_{d=1}^{D}(1 - \lambda_{N_d}(W_d^{(1)})) \\
&= 1 - \sum_{d=1}^{D}(a_d + c_d - 2\sqrt{a_d c_d}\cos\frac{(N_d - 1)\pi}{N_d}) \\
&\ge 1 - \sum_{d=1}^{D}(a_d + c_d - 2\sqrt{a_d c_d}). \qquad (5\text{–}11)
\end{aligned}$$

Recall that $R = \min\{1 - \lambda_2, 1 + \lambda_N\}$. In addition, a_d, c_d are fixed constants and satisfy $a_d \neq c_d$, $\sum_{d=1}^{D} a_d + c_d \le 1$, therefore the lower bounds of $1 - \lambda_2(W^{(D)})$ and $1 + \lambda_N(W^{(D)})$ are fixed positive constants. We then have that the convergence rate of $W^{(D)}$ satisfy $R = 1 - \rho(W^{(D)}) \ge c_0$, where c_0 is a constant independent of N. □ □

Remark 5.1. *Recall from Theorem 5.1, for any L-Z geometric or lattice graphs, as long as the weight matrix W is symmetric, no matter how do we design the weights $W_{i,j}$, the convergence rate becomes progressively smaller as the number of agents N increases, and it cannot be uniformly bounded away from 0. In contrast, Theorem 5.2 shows that for lattice graphs, asymmetry in the weights makes the convergence rate uniformly bounded away from 0. In fact, any amount of asymmetry along the coordinate axes of the lattice ($a_d \neq c_d$), will make this happen. Asymmetric weights thus make the linear distributed*

consensus law highly scalable. It eliminates the problem of degeneration of convergence rate with increasing N.

The second question is where do the node states converge to with asymmetric weights? Recall that the asymptotic steady state value of all agents is $\bar{x} = \sum_{i=1}^{N} \pi_i x_i(0)$. For a lattice graph, its Perron vector π is given in Lemma 5.1 and Lemma 5.2. Thus we can determine the steady state value $\bar{x}$ if the initial value $x(0)$ is given. This information is particularly useful to find the rendezvous position in multi-vehicle rendezvous problem. On the other hand, we see from Lemma 5.1 and Lemma 5.2 that if $a_d \neq c_d$, then $\pi_i \neq \frac{1}{N}$, which implies the steady-state value is not the average of the initial values. The asymmetric weight design is not applicable to distributed averaging problem. □

5.2.2 Numerical Comparison

In this section, we present the numerical comparison of the convergence rates of the distributed protocol (5–3) between asymmetric designed weights (Theorem 5.2) and symmetric optimal weights obtained from convex optimization [27, 29]. For simplicity, we take the 1-D lattice as an example. The asymmetric weights used are $W_{i,i+1} = c = 0.3, W_{i+1,i} = a = 0.2$. We see from Figure 5-3 that the convergence rate with asymmetric designed weights is much larger than that with symmetric optimal weights. In addition, given the asymmetric weight values $c = 0.3, a = 0.2$, we obtain from (5–10) and (5–11) that $\lambda_2 \leq 0.5 + 2\sqrt{0.06}, \lambda_N \geq 0.5 + 2\sqrt{0.06}$, which implies

$$R = \min\{1 - \lambda_2, 1 + \lambda_N\} \geq 0.5 - 2\sqrt{0.06} \approx 0.01. \tag{5–12}$$

We see from Figure 5-3 that the convergence rate R is indeed uniformly bounded below by (5–12).

5.3 Fast Consensus in More General Graphs

In this section, we study how to design the weight matrix W to increase the convergence rate of consensus in graphs that are more general than lattices. We use the idea of continuum approximation. Under some "niceness" properties, a graph can be thought

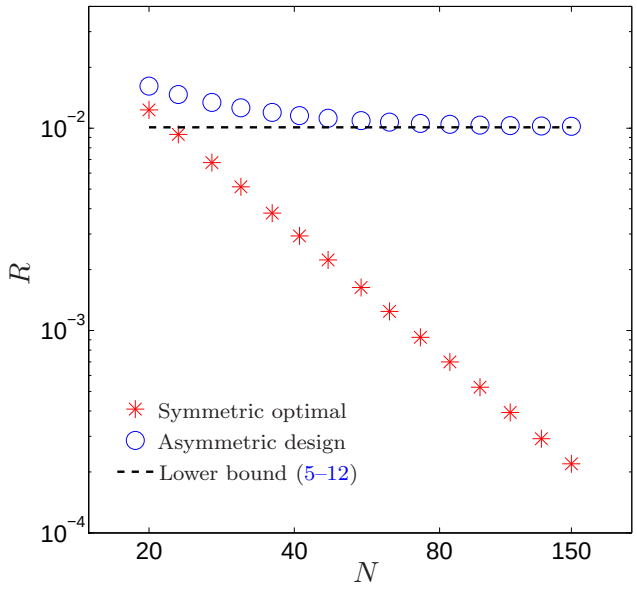

Figure 5-3. Comparison of convergence rate of 1-D lattice between asymmetric design and convex optimization (symmetric optimal).

of as approximation of a D-dimensional lattice, and by extension, of the Euclidean space corresponding to $\mathbb{R}^D$ [101]. These properties have to do with the graph not having arbitrarily large holes etc. Precise conditions under which a graph can be approximated by the D-dimensional lattice are explored in [102] (for infinite graphs) and in [36] (for finite graphs). The dimension D of the corresponding lattice/Euclidean space is also determined by these properties.

The key is to embed the discrete graph problem into a continuum-domain problem. We use a Sturm-Liouville operator to approximate the Laplacian matrix of a D-dimensional geometric graph. A D-dimensional geometric graph is simply a graph with a mapping of nodes to points in $\mathbb{R}^D$. Based on this approximation, we re-derive the asymmetric weights for lattices described in the previous section as values of continuous functions defined over $\mathbb{R}^D$ along the principal axes in $\mathbb{R}^D$. In a lattice, the neighbors of a node lie along the principal canonical axes of $\mathbb{R}^D$. For an arbitrary graph, the weights are now chosen as samples of the same functions, along directions in which the neighbors lie.

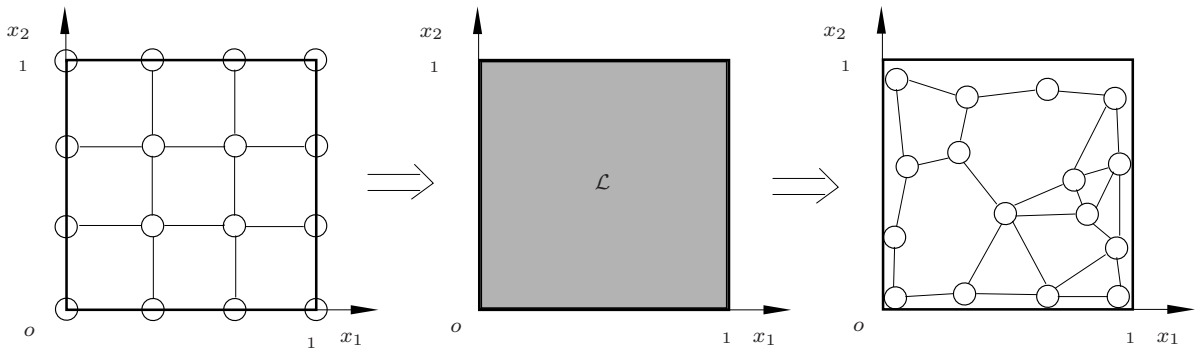

Figure 5-4. Continuum approximation of general graphs.

The method is applicable to arbitrary dimension, but we only consider the 2-D case in this chapter. Graphs with 2-D drawings are one of the most relevant classes of graphs for sensor networks where consensus is likely to find application.

5.3.1 Continuum Approximation

Recall that the convergence rate is intimately connected to the Laplacian matrix. We will show that the Laplacian matrix associated with a large 2-D lattice with certain weights can be approximated by a Sturm-Liouville operator defined on a 2-D plane. Thus it's reasonable to suppose that the Sturm-Liouville operator is also a good (continuum) approximation of the Laplacian matrix of large graphs with 2-D drawing. We start from 2-D lattice graph and derive a Sturm-Liouville operator. We then use this operator to approximate the graph Laplacian of more general graphs. The idea is illustrated in Figure 5-4.

For ease of description, we first consider a 1-D lattice, with the following asymmetric weights, which are inspired by the asymmetric control gains for vehicular platoons that was discussed in Chapter 2,

$$W_{i,i+1} = c = \frac{1+\varepsilon}{2}, \quad W_{i+1,i} = a = \frac{1-\varepsilon}{2}, \tag{5–13}$$

where $i \in \{1, 2, \cdots, N-1\}$ and $\varepsilon \in (0, 1)$ is a constant. The graph Laplacian corresponding to the weights given in (5–13) is given by

$$L^{(1)} = \begin{bmatrix} \frac{1+\varepsilon}{2} & \frac{-1-\varepsilon}{2} & & & \\ \frac{-1+\varepsilon}{2} & 1 & \frac{-1-\varepsilon}{2} & & \\ & \ddots & \ddots & \ddots & \\ & & \frac{-1+\varepsilon}{2} & 1 & \frac{-1-\varepsilon}{2} \\ & & & \frac{-1+\varepsilon}{2} & \frac{1-\varepsilon}{2} \end{bmatrix}. \tag{5–14}$$

Recall that to find a lower bound of the convergence rate of the weight matrix $W^{(1)}$, it's sufficient to find a lower bound of the second smallest eigenvalue of the associate Laplacian matrix $L^{(1)}$.

We now use a Sturm-Liouville operator to approximate the Laplacian matrix $L^{(1)}$. We first consider the finite-dimensional eigenvalue problem $L^{(1)}\phi = \mu\phi$. Expanding the equation, we have the following coupled difference equations

$$\frac{-1+\varepsilon}{2}\phi_{i-1} + \phi_i + \frac{-1-\varepsilon}{2}\phi_{i+1} = \mu\phi_i,$$

where $i \in \{1, 2, \cdots, N\}$ and $\phi_0 = \phi_1$, $\phi_{N+1} = \phi_N$. The above equation can be rewritten as

$$-\frac{1}{2N^2}\frac{\phi_{i-1} - 2\phi_i + \phi_{i+1}}{1/N^2} - \frac{\varepsilon}{N}\frac{\phi_{i+1} - \phi_{i-1}}{2/N} = \mu\phi_i.$$

The starting point for the continuum approximation is to consider a function $\phi(x) : [0, 1] \to \mathbb{R}$ that satisfies:

$$\phi_i = \phi(x)|_{x=i/(N+1)}, \tag{5–15}$$

such that a function that is defined at discrete points i will be approximated by a function that is defined everywhere in $[0, 1]$. The original function is thought of as samples of its continuous approximation. Under the assumption that N is large, using the following

finite difference approximation:

$$\left[\frac{\phi_{i-1}-2\phi_i+\phi_{i+1}}{1/N^2}\right]=\left[\frac{\partial^2\phi(x,t)}{\partial x^2}\right]_{x=i/(N+1)},$$
$$\left[\frac{\phi_{i+1}-\phi_{i-1}}{2/N}\right]=\left[\frac{\partial\phi(x,t)}{\partial x}\right]_{x=i/(N+1)},$$

the finite-dimensional eigenvalue problem can be approximated by the following Sturm-Liouville eigenvalue problem

$$\mathcal{L}^{(1)}\phi(x)=\mu\phi(x),\quad \text{where}\quad \mathcal{L}^{(1)}:=-\frac{1}{2N^2}\frac{d^2}{dx^2}-\frac{\varepsilon}{N}\frac{d}{dx}, \tag{5–16}$$

with Neumann boundary conditions:

$$\frac{d\phi(0)}{dx}=\frac{d\phi(1)}{dx}=0. \tag{5–17}$$

Lemma 5.3. *The eigenvalues of the Sturm-Liouville operator* $\mathcal{L}^{(1)}$ (5–16) *with boundary condition* (5–17) *for* $0<\varepsilon<1$ *are real and the first two smallest eigenvalues satisfy*

$$\mu_1(\mathcal{L}^{(1)})=0,\quad \mu_2(\mathcal{L}^{(1)})\geq\varepsilon^2/2. \qquad \square$$

We see from Lemma 5.3 that the second smallest eigenvalue of the Sturm-Liouville operator $\mathcal{L}^{(1)}$ is uniformly bounded away from zero. This result is not surprising, since it's a continuum counterpart of Lemma 5.1, which shows that the second smallest eigenvalue corresponding to the 1-D lattice with designed asymmetric weights is uniformly bounded below. The proof of Lemma 5.3 is given in Section 5.5.

We now consider the following weights for the consensus problem with D-dimensional lattice graph

$$W^{(D)}_{i,i^{d+}}=c_d=\frac{1+\varepsilon}{2D},\quad W^{(D)}_{i,i^{d-}}=a_d=\frac{1-\varepsilon}{2D}, \tag{5–18}$$

where $\varepsilon\in(0,1)$ is a constant.

The Laplacian matrix of a D-dimensional square lattice with the weights given in (5–18) is given by $L^{(D)} = I - W^{(D)}$. Following similar procedure of eigenvalue approximation for the 1-dimensional lattice, the second smallest eigenvalue of the Laplacian matrix $L^{(D)}$ can be approximated by that of the following Sturm-Liouville operator

$$\mathcal{L}^{(D)} = -\sum_{\ell=1}^{D}\left(\frac{1}{2DN_d^2}\frac{d^2}{dx_d^2} + \frac{\varepsilon}{DN_d}\frac{d}{dx_d}\right), \tag{5–19}$$

with the following Neumann boundary conditions

$$\frac{\partial\phi(\vec{x})}{\partial x_d}\Big|_{x_d=0 \text{ or } 1} = 0, \tag{5–20}$$

where $d = 1, 2, \cdots, D$ and $\vec{x} = [x_1, x_2, \cdots, x_D]^T$.

Continuum approximation has been used to study the stability margin of large vehicular platoons in Chapter 2, in which the continuum model gives more insight into the effect of asymmetry on the stability margin of the systems. In this chapter, we use the second smallest eigenvalue of the Sturm-Liouville operator $\mathcal{L}^{(D)}$ to approximate that of the Laplacian matrix $L^{(D)}$.

Theorem 5.3. *The second smallest eigenvalues $\mu_2(\mathcal{L}^{(D)})$ of the Sturm-Liouville operator $\mathcal{L}^{(D)}$ (5–19) with boundary condition (5–20) for $0 < \varepsilon < 1$ is real and satisfies*

$$\mu_2(\mathcal{L}^{(D)}) \geq \frac{\varepsilon^2}{2D}, \tag{5–21}$$

which is a positive constant independent of N. □

Proof of Theorem 5.3. By the method of separation of variables [77, 86], the eigenvalues of the Sturm-Liouville operator $\mathcal{L}^{(D)}$ is given by

$$\mu(\mathcal{L}^{(D)}) = \sum_{d=1}^{D}\mu(\mathcal{L}_d^{(1)}), \tag{5–22}$$

where $\mathcal{L}_d^{(1)}$ is the 1-dimensional Sturm-Liouville operator given by

$$\mathcal{L}_d^{(1)} = -\frac{1}{2DN_d^2}\frac{d^2}{dx_d^2} - \frac{\varepsilon}{DN_d}\frac{d}{dx_d},$$

with Neumann boundary conditions. Following Lemma 5.3, we have that the smallest eigenvalue of $\mathcal{L}_d^{(1)}$ is 0 and the second smallest eigenvalue of $\mathcal{L}_d^{(1)}$ is bounded below by $\mathcal{L}_d^{(1)} \geq \varepsilon^2/2D$. Therefore, we have from (5–22) that the second smallest eigenvalue is

$$\mu_2(\mathcal{L}^{(D)}) = \min_d\{\mu_2(\mathcal{L}^{(d)})\} \geq \frac{\varepsilon^2}{2D}.$$

□

5.3.2 Weight Design for General Graphs

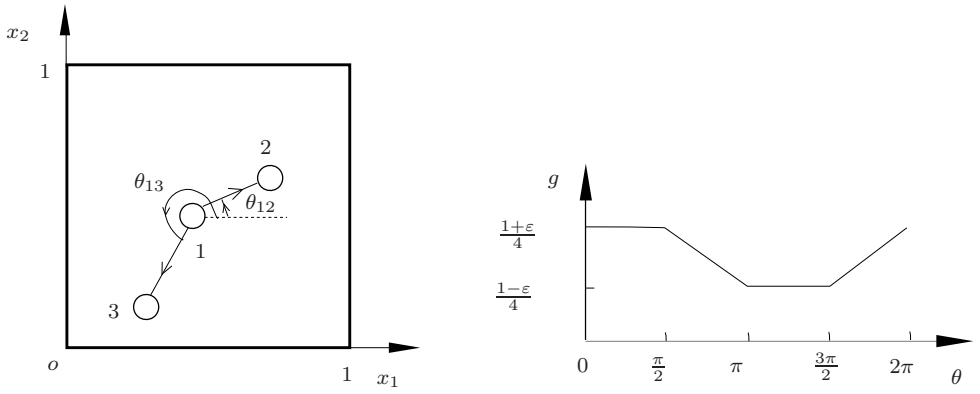

(a) Relative angle (b) Weight function

Figure 5-5. Weight design for general graphs.

The inspiration of the proposed method comes from the design for lattices. The 4 weights for each node i in a 2-D lattice can be re-expressed as samples of a continuous function $g : [0, 2\pi) \to [\frac{1-\epsilon}{4}, \frac{1+\epsilon}{4}]$:

$$W_{i,i^{1+}} = g(\theta_{i,i^{1+}}), \qquad W_{i,i^{2+}} = g(\theta_{i,i^{2+}}),$$
$$W_{i,i^{1-}} = g(\theta_{i,i^{1-}}), \qquad W_{i,i^{2-}} = g(\theta_{i,i^{2-}})$$

where $\theta_{i,j}$ is the relative angular position of j with respect to i. Given the angular positions of i's neighbors and the values of the weights, we know that the function g must satisfy:

$$g([0, \frac{\pi}{2}, \pi, \frac{3\pi}{2}]) = [\frac{1+\varepsilon}{4}, \frac{1+\varepsilon}{4}, \frac{1-\varepsilon}{4}, \frac{1-\varepsilon}{4}]. \tag{5–23}$$

Thus, we choose the function g as shown in Figure 5-5 (b).

For an arbitrary graph, we now choose the weights by sampling the function according to the angle associated with each edge (i, j):

$$W_{i,k} = \frac{g(\theta_{i,k})}{\sum_{j\in\mathbb{N}_i} g(\theta_{i,j})}, \tag{5–24}$$

where $g(\cdot)$ is the function described in Figure 5-5 (b). The above weight function (5–24) can be seen as a linear interpolation of (5–23). We see from (5–24) that the weight on each edge is computable in a distributed manner; a node only needs to know the angular position of its neighbors. This design method does not require any knowledge of the network topology or centralized computation.

5.3.3 Numerical Comparison

In this section, we present the numerical comparison of convergence rates among asymmetric design, symmetric optimal weights and weights chosen by the Metropolis-Hastings method. The symmetric optimal weights are obtained by using convex optimization method [29, 73]. The Metropolis-Hastings weights are picked by the following rule: $W_{i,j} = 1/|\mathbb{N}_i|$, where $\mathbb{N}_i$ denotes the number of neighbors of node i. The weights generated by this method are in general asymmetric. We plot the convergence rate R as a function of N, where N is the number of agents in the network. The amount of asymmetry used is $\varepsilon = 0.5$.

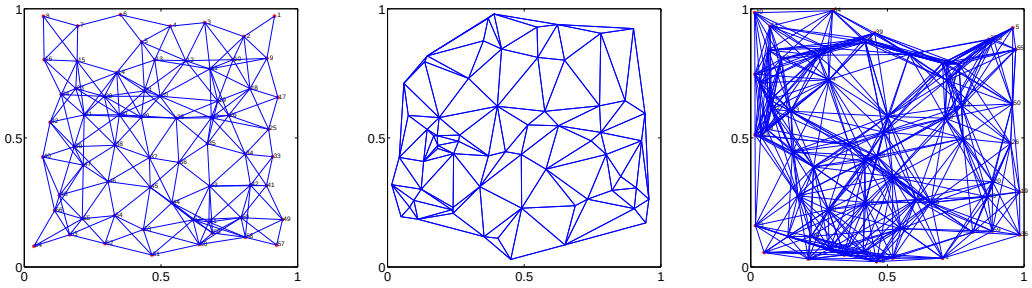

(a) L-Z geometric (b) Delaunay (c) Random geometric

Figure 5-6. Examples of 2-D L-Z geometric, Delaunay and random geometric graphs.

We first consider a L-Z geometric graph [36], which is generated by perturbing the node positions in a square 2-D lattice ($N_1 = N_2 = \sqrt{N}$) with Gaussian random noise (zero mean and $1/(4\sqrt{N})$ standard deviation) and connecting each node with other nodes that are within a $2/\sqrt{N}$ radius. Second, we consider a Delaunay graph [5], which is generated by placing N nodes on a 2-D unit square uniformly at random and connecting any two nodes if their corresponding Voronoi cells intersect, as long as their Euclidean distance is smaller than 1/3. Finally, we consider a random geometric graphs [103], which is generated by placing N nodes on a 2-D unit square uniformly at random and connecting pairs of nodes that are within a distance $3/\sqrt{N}$ of each other. Figure 5-6 gives examples of L-Z geometric graphs, Delaunay graphs and random geometric graphs.

Figure 5-7 shows the comparison of convergence rates among asymmetric design, symmetric optimal and Metropolis-Hastings weights. For each N, the convergence rate of 10 samples of the graphs are plotted. We see from Figure 5-7 that for almost every sample in each of the three classes, the convergence rate with the asymmetric design is an order of magnitude larger than the others, especially when N is large.

5.4 Summary

We studied the problem of how to design weights to increase the convergence rate of distributed consensus in networks with static topology. We proved that on lattice graphs, with proper choice of asymmetric weights, the convergence rate can be uniformly bounded away from zero. In addition, we proposed a distributed weight design algorithm for 2-dimensional geometric graphs to improve the convergence rate, by using a continuum approximation. Numerical calculations show that the resulting convergence rate is substantially larger than that optimal symmetric weights and Metropolis Hastings weights.

An important open question is a precise characterization of graphs for which theoretical guarantees on size-independent convergence rate can be provided with the proposed design. In addition, characterizing the asymptotic steady state value for more general graphs than lattices is also on-going work.

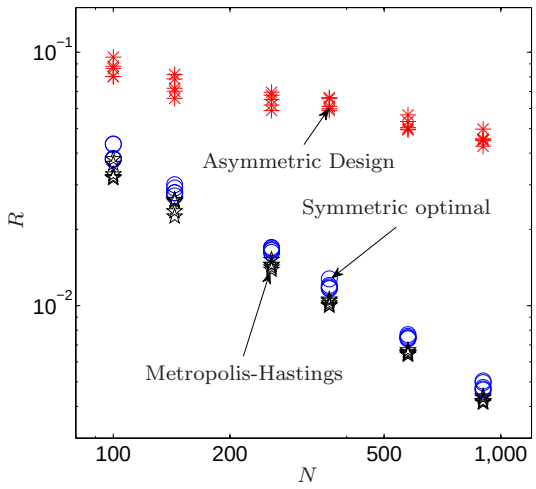

(a) L-Z geometric graphs

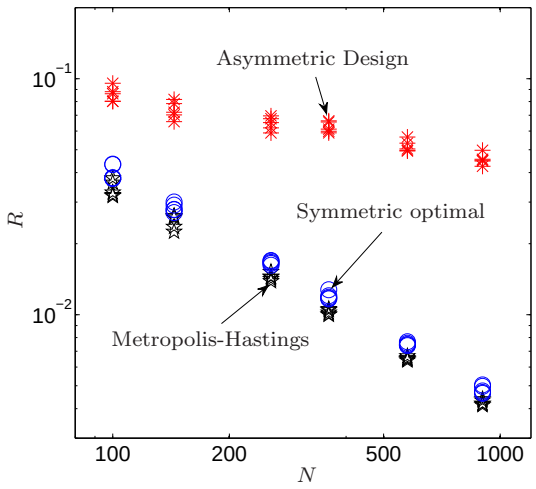

(b) Delaunay graphs

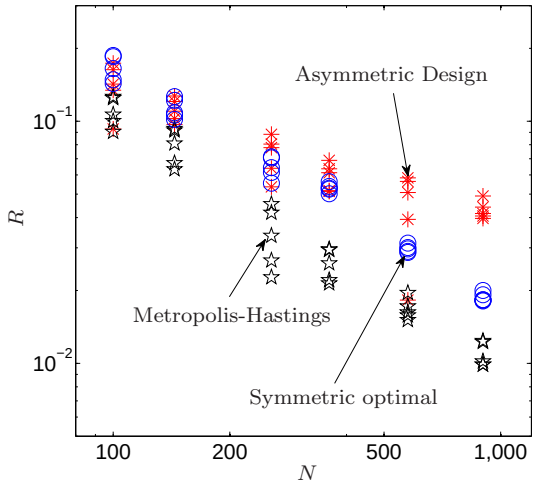

(c) Random geometric graphs

Figure 5-7. Comparison of convergence rates with proposed asymmetric weights, Metropolis-Hastings weights, and symmetric optimal. For each N, results from 5 sample graphs are plotted.

5.5 Technical Proofs

5.5.1 Proof of Lemma 5.1

The stochastic matrix $W^{(1)}$ has a simple eigenvalue $\lambda_1 = 1$. Following Theorem 3.1 of [104], the other eigenvalues of $W^{(1)}$ are given by

$$\lambda_\ell = 1 - a - c + 2\sqrt{ac}\cos\theta_\ell, \quad \ell \in \{2, \cdots, N\},$$

where θ_ℓ ($\theta \neq m\pi, m \in \mathbb{Z}$, $\mathbb{Z}$ being the set of integers) is the root of the following equation

$$2\sin(N\theta)cos(\theta) = (a+c)\sqrt{\frac{1}{ac}}\sin N\theta,$$

which implies

$$\sin(N\theta) = 0, \quad \text{or} \quad \cos\theta = \frac{(a+c)}{2}\sqrt{\frac{1}{ac}}.$$

Since $a > 0, c > 0$ and $a \neq c$, we have $\frac{(a+c)}{2}\sqrt{\frac{1}{ac}} > 1$, thus $\cos\theta \neq \frac{(a+c)}{2}\sqrt{\frac{1}{ac}}$. In addition, we have that $\theta \neq m\pi$, which yields

$$\theta_\ell = \frac{(\ell-1)\pi}{N}, \ \ell = \{2, \cdots, N\}. \tag{5–25}$$

We now obtain the eigenvalues of $W^{(1)}$, which is given by

$$\lambda_\ell = 1 - a - c + 2\sqrt{ac}\cos\frac{(\ell-1)\pi}{N}, \ \ell = \{2, \cdots, N\}.$$

Let $\pi = [\pi_1, \pi_2, \cdots, \pi_N]$ be the left Perron vector of $W^{(1)}$. From the definition of Perron vector, we have $\pi W^{(1)} = \pi$. Thanks to the special structure of the tridiagonal form of $W^{(1)}$, we can solve for π explicitly, which yields

$$\pi_i = (c/a)^{i-1}\pi_1, \tag{5–26}$$

where $i \in \{2, 3, \cdots, N\}$. In addition, we have $\pi_i > 0$ and $\sum_{i=1}^N \pi_i = 1$. Therefore,

$$1 = \sum_{i=1}^N \pi_i = \sum_{i=1}^N (c/a)^{i-1}\pi_1 \quad \Rightarrow \quad \pi_1 = \frac{1 - c/a}{1 - (c/a)^N}.$$

Substituting the above equation into (5–26), we complete the proof. □

5.5.2 Proof of Lemma 5.2

With the weights given in (5–8), it is straightforward - through a bit tedious - to show that the graph Laplacian $L^{(D)}$ associated with the D-dimensional lattice has the following form:

$$L^{(d)} = I_{N_d} \otimes L^{(d-1)} + L_d^{(1)} \otimes I_{N_1 N_2 \cdots N_{d-1}}, \quad 2 \leq d \leq D,$$

where $L^{(1)} = L_1^{(1)}$ and $L_d^{(1)} = 1 - W_d^{(1)}$ is the Laplacian matrix of dimension $N_d \times N_d$, which is given by

$$L_d^{(1)} = \begin{bmatrix} c_d & -c_d & & & \\ -a_d & a_d + c_d & -c_d & & \\ & \ddots & \ddots & \ddots & \\ & & -a_d & a_d + c_d & -c_d \\ & & & -a_d & a_d \end{bmatrix}. \tag{5–27}$$

Since a D-dimensional lattice is the Cartesian product graph of D 1-dimensional lattices, the eigenvalues of the graph Laplacian matrix $L^{(D)}$ are sum of the eigenvalues of the D 1-dimensional Laplacian matrix $L_d^{(1)}$. Thus, we have

$$\mu_{\ell_1,\ldots,\ell_D}(L^{(D)}) = \sum_{d=1}^{D} \mu_{\ell_d}(L_d^{(1)}).$$

In addition, we have that $W^{(D)} = I_N - L^{(D)}$ and $W_d^{(1)} = I_{N_d} - L_d^{(1)}$, thus the eigenvalues $\lambda_{\vec{\ell}}$ of $W^{(D)}$ are given by

$$\begin{aligned} \lambda_{\vec{\ell}}\,(W^{(D)}) &= 1 - \mu_{\vec{\ell}}\,(L^{(D)}) = 1 - \sum_{d=1}^{D} \mu_{\ell_d}(L_d^{(1)}) \\ &= 1 - \sum_{d=1}^{D} (1 - \lambda_{\ell_d}(W_d^{(1)})). \end{aligned}$$

To see $\pi = \pi_D^{(1)} \otimes \pi_{D-1}^{(1)} \otimes \cdots \otimes \pi_1^{(1)}$ is the left Perron vector of $W^{(D)}$, we first notice that

$$\pi_d^{(1)} W_d^{(1)} = \pi_d^{(1)}, \quad \pi_d^{(1)} L_d^{(1)} = 0,$$

where $d \in \{1, \cdots, D\}$. The rest of the proof follows by straightforward induction method, we omit the proof due to space limit. □

5.5.3 Proof of Lemma 5.3

Multiply both sides of (5–16) by $2N^2 e^{2\varepsilon N x}$, we obtain the standard Sturm-Liouville eigenvalue problem

$$\frac{d}{dx}\Big(e^{2\varepsilon N x}\frac{d\phi(x)}{dx}\Big) + 2N^2\mu e^{2\varepsilon N x}\phi(x) = 0. \tag{5–28}$$

According to Sturm-Liouville Theory, all the eigenvalues are real, see [77, 86]. To solve the Sturm-Liouville eigenvalue problem (5–16)-(5–17), we assume solution of the form, $\phi(x) = e^{rx}$, then we obtain the following equation

$$\begin{aligned} r^2 + 2\varepsilon N r + 2\mu N^2 &= 0, \\ \Rightarrow r &= N(-\varepsilon \pm \sqrt{\varepsilon^2 - 2\mu}). \end{aligned} \tag{5–29}$$

Depending on the discriminant in the above equation, there are three cases to analyze:

1. $\mu < \varepsilon^2/2$, then the eigenfunction $\phi(x)$ has the following form $\phi(x) = c_1 e^{N(-\varepsilon+\sqrt{\varepsilon^2-2\mu})x} + c_2 e^{N(-\varepsilon-\sqrt{\varepsilon^2-2\mu})x}$, where c_1, c_2 are some constants. Applying the boundary condition (5–17), it's straightforward to see that, for non-trivial eigenfunctions $\phi(x)$ to exit, the following equation must be satisfied

$$\frac{-\varepsilon + \sqrt{\varepsilon^2 - 2\mu}}{\varepsilon + \sqrt{\varepsilon^2 - 2\mu}} = e^{2N\sqrt{\varepsilon^2-2\mu}}\frac{-\varepsilon + \sqrt{\varepsilon^2 - 2\mu}}{\varepsilon + \sqrt{\varepsilon^2 - 2\mu}}.$$

   Thus, we have $\mu = 0$.

2. $\mu = \varepsilon^2/2$, then the eigenfunction $\phi(x)$ has the following form

$$\phi(x) = c_1 e^{-\varepsilon N x} + c_2 x e^{-\varepsilon N x}.$$

Applying the boundary condition (5–17) again, it's straightforward to see that there is no eigenvalue for this case.

3. $\mu > \varepsilon^2/2$, then the eigenfunction has the following form $\phi(x) = e^{-\varepsilon N x}(c_1 \cos(N\sqrt{2\mu - \varepsilon^2}x) + c_2 \sin(N\sqrt{2\mu - \varepsilon^2}x)$. Applying the boundary condition (5–17), for non-trivial eigenfunctions to exit, the eigenvalues μ must satisfy $\mu = \frac{\varepsilon^2}{2} + \frac{\ell^2\pi^2}{2N^2}$, where $\ell = 1, 2, \cdots$.

Combining the above three cases, the eigenvalues of the Sturm-Liouville operator are $\mu \in \{0, \frac{\varepsilon^2}{2} + \frac{\ell^2\pi^2}{2N^2}\}$, where $\ell \in \{1, 2, \cdots\}$. The second smallest eigenvalue $\mu_2(\mathcal{L})$ of the Strum-Liouville operator $\mathcal{L}$ is then given by

$$\mu_2(\mathcal{L}) = \frac{\varepsilon^2}{2} + \frac{\pi^2}{2N^2} \geq \frac{\varepsilon^2}{2},$$

which is a constant that is bounded away from 0. □

ontinuum approximation has been used to study the stability margin of large vehicular platoons [91, 105], in which the continuum model gives more insight on the effect of asymmetry on the stability margin of the systems. In this chapter, we use the second smallest eigenvalue of the Sturm-Liouville operator $\mathcal{L}^{(D)}$ to approximate that of the Laplacian matrix $L^{(D)}$.

CHAPTER 6
CONCLUSIONS AND FUTURE WORK

This chapter summarizes the contributions of this dissertation and discusses possible directions for future research.

6.1 Conclusions

This dissertation studied performance scaling of distributed control of multi-agent systems with respect to network size. We investigated two classes of distributed control problems that are relevant to vehicular formation control and distributed consensus. In the vehicular formation control problem, each vehicle is modeled by a double integrator, while the dynamics of each agent in distributed consensus are given a single integrator. Despite difference in agent dynamics, the two problems suffer from similar performance limitations. In particular, their performances degrade when the number of agents in the system increases with symmetric control, where symmetric control refers to, between each pair of neighboring agents, the information received from each other is given the same weight. One of the main contributions of this work is that we proposed an asymmetric control design method to ameliorate the performance scaling laws for both vehicular formation control and distributed consensus. Asymmetric design means between each pair of neighboring agents, the information received from each other is weighted differently, instead of equally in symmetric design. We showed the resulting performance scaling laws were improved considerably over those with symmetric control.

For the vehicular formation control problem, we described a novel framework for modeling, analysis and distributed control design. The key component of this framework is a PDE-based (partial differential equation) continuous approximation of the (spatially) discrete closed-loop dynamics of the controlled formation. Based on this PDE model, we derived exact quantitative scaling laws of the stability margin and robustness to external disturbances, with respect to the number of vehicles in the formation. The results showed that with symmetric control, the stability margin and robustness performances degraded

progressively when the number of vehicles in the team increased. The scaling laws of stability margin and robustness performances developed in this dissertation are helpful to understand the limitations of distributed control architecture.

Besides analysis of performance scalings, the PDE model is also convenient for distributed control design. By taking advantages of the well developed PDE and operator (such as Sturm-Liouville) theory as well as perturbation technique, we proposed an *asymmetric* design method, which improved the stability margin and robustness to disturbances considerably over symmetric control. Numerical experiments showed that the PDE model made an accurate approximation of the state-space model even for a small value of N, where N is the number of vehicles in the formation. Moreover, the resulting asymmetric control is simple to implement and therefore attractive for practical applications.

We next applied the asymmetric design method to another class of distributed control problem: distributed consensus. In distributed consensus, each agent in a network updates its state by using a weighted summation of it own state and the states of its neighbors. The goal is to make all the agents' states reach a common value. It was shown that with symmetric weight, the consensus rate became progressively smaller when the number of agents in the network increased, even when the weights were chosen in an optimal manner. We proposed a method to design *asymmetric* weights to speed up the convergence rate of distributed consensus in networks with static topology. We proved that on lattice graphs, with proper choice of asymmetric weights, the convergence rate could be uniformly bounded away from zero with respect to the number of agents in the network. In addition, we developed a distributed weight design algorithm for more general graphs than lattices to improve their convergence rates. Numerical calculations showed that the resulting convergence rate was substantially larger than that with optimal symmetric weights or Metropolis Hastings weights.

6.2 Future Work

There are several possible topics of future investigations that are summarize below.

The information graphs studied in Chapter 2-4 are limited to D-dimensional lattices. More complex graph structures should be explored in future work. We believe that the PDE approximation will be beneficial here, by allowing us to sample from the continuous gain functions defined over a continuous domain to assign gains to spatially discrete agents.

In Chapter 3, numerical simulations show that with *asymmetric velocity* feedback, the system's robustness to external disturbance can be improved significantly over symmetric control and the case with equal asymmetry in the position and velocity feedback. These results were summarized as a conjecture. Future research will focus on the theoretical analysis to verify such an improvement.

Additionally, regarding the distributed consensus problem in Chapter 5, an important open question is a precise characterization of graphs for which theoretical guarantees on size-independent convergence rate can be provided with the proposed design. Characterizing the asymptotic steady state value for more general graphs than lattices is valuable as well.

Last but not the least, we believe the asymmetric design will have a potential important impact on other applications of distributed control of large networked systems. Besides vehicular formations and distributed consensus, we believe the asymmetric design method can also be applied to improve mixing time of random walks and performance of distributed Kalman filter. Future work will look at these applications. In addition, the asymmetric design may also help answer the question of how to avoid actuator saturation in large-scale multi-agent system which results from large transient errors and/or high gain controller, as evidenced in [95, 106, 107].

REFERENCES

[1] A. Jadbabaie, J. Lin, and A. Morse, "Coordination of groups of mobile autonomous agents using nearest neighbor rules," *IEEE Transactions on Automatic Control*, vol. 48, no. 6, pp. 988–1001, 2003.

[2] M. Egerstedt and X. Hu, "Formation control with virtual leaders and reduced communications," *IEEE Trans. on Robotics and Automation*, vol. 17, no. 6, pp. 947–951, 2001.

[3] S. Darbha and P. R. Pagilla, "Limitations of employing undirected information flow graphs for the maintenance of rigid formations for heterogeneous vehicles," *International journal of engineering science*, vol. 48, no. 11, pp. 1164–1178, 2010.

[4] H. Tanner, G. Pappas, and V. Kumar, "Leader-to-formation stability," *Robotics and Automation, IEEE Transactions on*, vol. 20, no. 3, pp. 443–455, 2004.

[5] S. Martinez, J. Cortes, and F. Bullo, "Motion coordination with distributed information," *Control Systems Magazine, IEEE*, vol. 27, no. 4, pp. 75–88, 2007.

[6] H. Yin, P. G. Mehta, S. P. Meyn, and U. V. Shanbhag, "Synchronization of coupled oscillators is a game," in *Proc. of 2010 American Control Conference*, Baltimore, MD, 2010, pp. 1783–1790.

[7] F. Dorfler and F. Bullo, "Synchronization and transient stability in power networks and non-uniform kuramoto oscillators," in *American Control Conference (ACC), 2010*, 2010, pp. 930–937.

[8] R. Sepulchre, D. Paley, and N. Leonard, "Collective motion and oscillator synchronization," *Cooperative control*, pp. 466–469, 2004.

[9] J. Tsitsiklis, "Problems in decentralized decision making and computation." Ph.D. dissertation, Massachusetts Institute of Technology, 1984.

[10] R. Olfati-Saber, J. Fax, and R. Murray, "Consensus and cooperation in networked multi-agent systems," *Proceedings of the IEEE*, vol. 95, no. 1, pp. 215–233, 2007.

[11] W. Ren and R. Beard, *Distributed consensus in multi-vehicle cooperative control: theory and applications*. Springer Verlag, 2008.

[12] C. Reynolds, "Flocks, herds and schools: A distributed behavioral model," in *ACM SIGGRAPH Computer Graphics*, vol. 21, no. 4. ACM, 1987, pp. 25–34.

[13] A. Okubo, "Dynamical aspects of animal grouping: swarms, schools, flocks, and herds," *Advances in Biophysics*, vol. 22, pp. 1–94, 1986.

[14] J. Toner and Y. Tu, "Flocks, herds, and schools: A quantitative theory of flocking," *Physical Review E*, vol. 58, no. 4, p. 4828, 1998.

[15] H. Tanner and D. Christodoulakis, "Decentralized cooperative control of heterogeneous vehicle groups," *Robotics and autonomous systems*, vol. 55, no. 11, pp. 811–823, 2007.

[16] P. J. Seiler, "Coordinated control of unmanned aerial vehicles," Ph.D. dissertation, University of California, 2001.

[17] E. Wagner, D. Jacques, W. Blake, and M. Pachter, "Flight test results of close formation flight for fuel savings," in *AIAA Atmospheric Flight Mechanics Conference and Exhibit*, 2002, AIAA-2002-4490.

[18] F. Bullo, J. Cortés, and S. Martinez, *Distributed control of robotic networks*. Princeton University Press Princeton, NJ, 2009.

[19] P. M. Ludwig, "Formation control for multi-vehicle robotic minesweeping," Master's thesis, Naval postgraduate school, 2000.

[20] A. J. Fax and R. M. Murray, "Information flow and cooperative control of vehicle formations," *IEEE Transactions on Automatic Control*, vol. 49, pp. 1465–1476, September 2004.

[21] P. Barooah and J. P. Hespanha, "Graph effective resistances and distributed control: Spectral properties and applications," in *Proc. of the 45th IEEE Conference on Decision and Control*, December 2006, pp. 3479–3485.

[22] G. Lafferriere, A. Williams, J. Caughman, and J. Veerman, "Decentralized control of vehicle formations," *Systems & control letters*, vol. 54, no. 9, pp. 899–910, 2005.

[23] A. Lewis and M. Overton, "Eigenvalue optimization," *Acta numerica*, vol. 5, no. 149-190, p. 4, 1996.

[24] M. Overton, "Large-scale optimization of eigenvalues," *SIAM J. Optim.*, vol. 2, pp. 88–120, 1992.

[25] M. Overton and R. Womersley, "On minimizing the spectral radius of a nonsymmetric matrix function: Optimality conditions and duality theory," *SIAM J. Matrix ANAL. APPL.*, vol. 9, no. 4, pp. 473–498, 1988.

[26] ——, "Optimality conditions and duality theory for minimizing sums of the largest eigenvalues of symmetric matrices," *Mathematical Programming*, vol. 62, no. 1, pp. 321–357, 1993.

[27] S. Boyd, "Convex optimization of graph Laplacian eigenvalues," in *Proceedings of the International Congress of Mathematicians*, vol. 3. Citeseer, 2006, pp. 1311–1319.

[28] M. Rotkowitz and S. Lall, "A characterization of convex problems in decentralized control," *Automatic Control, IEEE Transactions on*, vol. 51, no. 2, pp. 274–286, 2006.

[29] L. Xiao and S. Boyd, "Fast linear iterations for distributed averaging," *Systems & Control Letters*, vol. 53, no. 1, pp. 65–78, 2004.

[30] S. Boyd and L. Vandenberghe, *Convex optimization*. Cambridge Univ Pr, 2004.

[31] P. Seiler, A. Pant, and J. K. Hedrick, "Disturbance propagation in vehicle strings," *IEEE Transactions on Automatic Control*, vol. 49, pp. 1835–1841, October 2004.

[32] B. Bamieh, M. R. Jovanović, P. Mitra, and S. Patterson, "Effect of topological dimension on rigidity of vehicle formations: fundamental limitations of local feedback," in *Proceedings of the 47th IEEE Conference on Decision and Control*, Cancun, Mexico, 2008, pp. 369–374.

[33] J. Veerman, "Stability of large flocks: an example," July 2009, arXiv:1002.0768.

[34] M. R. Jovanović and B. Bamieh, "On the ill-posedness of certain vehicular platoon control problems," *IEEE Trans. Automatic Control*, vol. 50, no. 9, pp. 1307–1321, September 2005.

[35] J. Veerman, B. Stošić, and F. Tangerman, "Automated traffic and the finite size resonance," *Journal of Statistical Physics*, vol. 137, no. 1, pp. 189–203, October 2009.

[36] E. Lovisari and S. Zampieri, "Performance metrics in the average consensus problem: a tutorial," February 2012, annual Reviews in Control.

[37] H. Hao, P. Barooah, and J. Veerman, "Effect of network structure on the stability margin of large vehicle formation with distributed control," in *Proceedings of the 49th IEEE conference on Decision and Control*, December 2010.

[38] J. K. Hedrick, M. Tomizuka, and P. Varaiya, "Control issues in automated highway systems," *IEEE Control Systems Magazine*, vol. 14, pp. 21 – 32, December 1994.

[39] S. Darbha, J. Hedrick, C. Chien, and P. Ioannou, "A comparison of spacing and headway control laws for automatically controlled vehicles," *Vehicle System Dynamics*, vol. 23, no. 8, pp. 597–625, 1994.

[40] E. Chan, P. Gilhead, P. Jelinek, and P. Krejci, "SARTRE cooperative control of fully automated platoon vehicles," in *18th World Congress on Intelligent Transport Systems*, October 2011.

[41] "Safe road trains for the environment." [Online]. Available: http://www.sartre-project.eu/

[42] "The grand cooperative driving challenge." [Online]. Available: http://www.gcdc.net/

[43] S. M. Melzer and B. C. Kuo, "A closed-form solution for the optimal error regulation of a string of moving vehicles," *IEEE Transactions on Automatic Control*, vol. AC-16, no. 1, pp. 50–52, February 1971.

[44] Y. Zhang, B. Kosmatopoulos, P. Ioannou, and C. Chien, "Using front and back information for tight vehicle following maneuvers," *IEEE Transactions on Vehicular Technology*, vol. 48, no. 1, pp. 319–328, 1999.

[45] K. Chu, "Decentralized control of high-speed vehicular strings," *Transportation Science*, vol. 8, no. 4, p. 361, 1974.

[46] L. Peppard, "String stability of relative-motion PID vehicle control systems," *Automatic Control, IEEE Transactions on*, vol. 19, no. 5, pp. 579–581, 1974.

[47] M. R. Jovanović and B. Bamieh, "On the ill-posedness of certain vehicular platoon control problems," *IEEE Transactions on Automatic Control*, vol. 50, no. 9, pp. 1307 – 1321, September 2005.

[48] P. Barooah, P. G. Mehta, and J. P. Hespanha, "Mistuning-based decentralized control of vehicular platoons for improved closed loop stability," *IEEE Transactions on Automatic Control*, vol. 54, no. 9, pp. 2100–2113, September 2009.

[49] S. Stankovic, M. Stanojevic, and D. Siljak, "Decentralized overlapping control of a platoon of vehicles," *Control Systems Technology, IEEE Transactions on*, vol. 8, no. 5, pp. 816–832, 2000.

[50] S. S. Stankovic, M. J. Stanojevic, and D. D. Siljak, "Decentralized overlapping control of a platoon of vehicles," *IEEE Transactions on Control Systems Technology*, vol. 8, pp. 816–832, September 2000.

[51] Y. Zhang, E. B. Kosmatopoulos, P. A. Ioannou, and C. C. Chien, "Autonomous intelligent cruise control using front and back information for tight vehicle following maneuvers," *IEEE Transactions on Vehicular Technology*, vol. 48, pp. 319–328, January 1999.

[52] P. Barooah and J. Hespanha, "Error amplification and disturbance propagation in vehicle strings with decentralized linear control," in *44th IEEE Conference on Decision and Control*. IEEE, 2005, pp. 4964 – 4969.

[53] S. K. Yadlapalli, S. Darbha, and K. R. Rajagopal, "Information flow and its relation to stability of the motion of vehicles in a rigid formation," *IEEE Transactions on Automatic Control*, vol. 51, no. 8, August 2006.

[54] P. Hughes and P. Carlisle, *Spacecraft attitude dynamics*. J. Wiley, 1986.

[55] S. LaValle, *Planning algorithms*. Cambridge Univ Pr, 2006.

[56] S. Bhat and D. Bernstein, "Continuous finite-time stabilization of the translational and rotational double integrators," *Automatic Control, IEEE Transactions on*, vol. 43, no. 5, pp. 678–682, 1998.

[57] V. Rao and D. Bernstein, "Naive control of the double integrator," *Control Systems Magazine, IEEE*, vol. 21, no. 5, pp. 86–97, 2001.

[58] D. Kirk, *Optimal control theory: an introduction*. Dover Publications, 2004.

[59] W. Ren, "On consensus algorithms for double-integrator dynamics," *Automatic Control, IEEE Transactions on*, vol. 53, no. 6, pp. 1503–1509, 2008.

[60] S. Sheikholeslam and C. A. Desoer, "Control of interconnected nonlinear dynamical systems: the platoon problem," *IEEE Transactions on Automatic Control*, vol. 37, no. 6, pp. 806–810, June 1992.

[61] P. A. Cook, "Stable control of vehicle convoys for safety and comfort," *IEEE Transactions on Automatic Control*, vol. 52, no. 3, pp. 526–531, March 2007.

[62] R. Middleton and J. Braslavsky, "String instability in classes of linear time invariant formation control with limited communication range," *IEEE Transactions on Automatic Control*, vol. 55, no. 7, pp. 1519–1530, 2010.

[63] M. E. Khatir and E. J. Davison, "Decentralized control of a large platoon of vehicles using non-identical controllers," in *Proceedings of the 2004 American Control Conference*, 2004, pp. 2769–2776.

[64] X. Liu, A. Goldsmith, S. Mahal, and J. Hedrick, "Effects of communication delay on string stability in vehicle platoons," in *Intelligent Transportation Systems, 2001. Proceedings. 2001 IEEE*. IEEE, 2001, pp. 625–630.

[65] X. Liu, S. S. Mahal, A. Goldsmith, and J. K. Hedrick, "Effects of communication delay on string stability in vehicle platoons," in *IEEE International Conference on Intelligent Transportation Systems (ITSC)*, August 2001, pp. 625–630.

[66] S. Klinge and R. Middleton, "Time headway requirements for string stability of homogeneous linear unidirectionally connected systems," in *Proceedings of the 48th IEEE Conference on Decision and Control*. IEEE, 2009, pp. 1992–1997.

[67] I. Lestas and G. Vinnicombe, "Scalability in heterogeneous vehicle platoons," in *American Control Conference*, 2007, pp. 4678–4683.

[68] F. Tangerman and J. Veerman, "Asymmetric Decentralized Flocks," *accepted to IEEE Transactions on Automatic Control*, 2011. [Online]. Available: http://www.mth.pdx.edu/~veerman/publ04.html

[69] A. Pant, P. Seiler, , and K. Hedrick, "Mesh stability of look-ahead interconnected systems," *IEEE Transactions on Automatic Control*, vol. 47, pp. 403–407, February 2002.

[70] A. Olshevsky and J. N. Tsitsiklis, "Convergence speed in distributed consensus and averaging," *SIAM J. Control and Optimization*, vol. 48, no. 1, pp. 33–55, 2009.

[71] T. Chan and L. Ning, "Fast convergence for consensus in dynamic networks," *Automata, Languages and Programming*, pp. 514–525, 2011.

[72] M. Cao, D. Spielman, and A. Morse, "A lower bound on convergence of a distributed network consensus algorithm," in *the 44th IEEE Conference on Decision and Control*. IEEE, 2005, pp. 2356–2361.

[73] S. Boyd, P. Diaconis, and L. Xiao, "Fastest mixing markov chain on a graph," *SIAM review*, pp. 667–689, 2004.

[74] R. Olfati-Saber, "Ultrafast consensus in small-world networks," in *Proceedings of the 2005 American Control Conference*, 2005, pp. 2371–2378.

[75] L. Wang and F. Xiao, "Finite-time consensus problems for networks of dynamic agents," *Automatic Control, IEEE Transactions on*, vol. 55, no. 4, pp. 950–955, 2010.

[76] S. Sundaram and C. Hadjicostis, "Finite-time distributed consensus in graphs with time-invariant topologies," in *American Control Conference, 2007.*, 2007, pp. 711–716.

[77] R. Haberman, *Elementary applied partial differential equations: with Fourier series and boundary value problems*. Prentice-Hall, 2003.

[78] M. Parashar, J. Thorp, and C. Seyler, "Continuum modeling of electromechanical dynamics in large-scale power systems," *Circuits and Systems I: Regular Papers, IEEE Transactions on*, vol. 51, no. 9, pp. 1848–1858, 2004.

[79] A. Sarlette and R. Sepulchre, "A pde viewpoint on basic properties of coordination algorithms with symmetries," in *Proceedings of the 48th IEEE Conference on Decision and Control*, Shanghai, China, 2009, pp. 5139–5144.

[80] E. W. Justh and P. S. Krishnaprasad, "Steering laws and continuum models for planar formations," in *42nd IEEE Conference on Decision and Control*, December 2003, pp. 3609 – 3614.

[81] P. Frihauf and M. Krstic, "Leader-enabled deployment into planar curves: A pde-based approach," *Automatic Control, IEEE Transactions on*, no. 99, pp. 1–16, 2010.

[82] D. Helbing, "Traffic and related self-driven many-particle systems," *Review of Modern Physics*, vol. 73, pp. 1067–1141, 2001.

[83] G. F. Trecate, A. Buffa, and M. Gati, "Analysis of coordination in multi-agent systems through partial difference equations," *IEEE Transactions on Automatic Control*, vol. 61, no. 6, pp. 1058–1063, June 2006.

[84] H. Hao and P. Barooah, "Control of large 1d networks of double integrator agents: role of heterogeneity and asymmetry on stability margin," in *Proceedings of the 49th IEEE conference on Decision and Control*, December 2010.

[85] H. Khalil, *Nonlinear Systems 3rd.* Prentice hall Englewood Cliffs, NJ, 2002.

[86] L. Evans, *Partial Differential Equations: Second Edition (Graduate Studies in Mathematics).* American Mathematical Society, 2010.

[87] G. Balas and A. Packard, "The structured singular value (μ) framework," *The Control Handbook*, pp. 671–687, 1996.

[88] H. Hao and P. Barooah, "Decentralized control of large vehicular formations: stability margin and sensitivity to external disturbances," *Arxiv preprint arXiv:1108.1409*, 2011. [Online]. Available: http://arxiv.org/abs/1108.1409

[89] ——, "Control of large 1D networks of double integrator agents: role of heterogeneity and asymmetry on stability margin," in *IEEE Conference on Decision and Control*, December 2010, pp. 7395 – 7400, expanded version: arXiv:1011.0791.

[90] B. Bamieh, M. Jovanovic, P. Mitra, and S. Patterson, "Coherence in large-scale networks: Dimension dependent limitations of local feedback," *IEEE Transactions on Automatic Control, in press,*, 2012. [Online]. Available: http://arxiv.org/abs/1112.4011v1

[91] H. Hao, P. Barooah, and P. G. Mehta, "Stability margin scaling of distributed formation control as a function of network structure," *IEEE Transactions on Automatic Control*, vol. 56, no. 4, pp. 923–929, April 2011.

[92] H. Hao, P. Barooah, and P. Mehta, "Distributed control of two dimensional vehicular formations: stability margin improvement by mistuning," in *ASME Dynamic Systems and Control Conference*, October 2009.

[93] R. Diestel, *Graph Theory*, 3rd ed., ser. Graduate Texts in Mathematics. Springer-Verlag, Heidelberg, 2005, vol. 173.

[94] R. Curtain and H. Zwart, *An introduction to infinite-dimensional linear systems theory.* Springer, 1995.

[95] H. Hao and P. Barooah, "Stability and robustness of large platoons of vehicles with double-integrator models and nearest neighbor interaction," *International Journal of Robust and Nonlinear Control*, October 2012.

[96] M. DeGroot, "Reaching a consensus," *Journal of the American Statistical Association*, vol. 69, no. 345, pp. 118–121, 1974.

[97] T. Vicsek, A. Czirok, E. Ben-Jacob, I. Cohen, and O. Shochet, "Novel type of phase transition in a system of self-driven particles," *Physical Review Letters*, vol. 75, no. 6, pp. 1226–1229, 1995.

[98] V. Borkar and P. Varaiya, "Asymptotic agreement in distributed estimation," *Automatic Control, IEEE Transactions on*, vol. 27, no. 3, pp. 650–655, 1982.

[99] Y. Chen, R. Tron, A. Terzis, and R. Vidal, "Accelerated corrective consensus: Converge to the exact average at a faster rate," in *American Control Conference (ACC), 2011.* IEEE, 2011, pp. 3417–3422.

[100] K. Cai and H. Ishii, "Convergence time analysis of quantized gossip consensus on digraphs," *Automatica*, 2012.

[101] P. G. Doyle and J. L. Snell, "Random walks and electric networks," Math. Assoc. of America, 1984.

[102] P. Barooah and J. P. Hespanha, "Error scaling laws for optimal estimation from relative measurements," *IEEE Transactions on Information Theory*, vol. 55, pp. 5661 – 5673, December 2009.

[103] S. Boyd, A. Ghosh, B. Prabhakar, and D. Shah, "Randomized gossip algorithms," *IEEE Transactions on Information Theory*, vol. 52, no. 6, pp. 2508–2530, 2006.

[104] W. Yueh and S. Cheng, "Explicit eigenvalues and inverses of tridiagonal toeplitz matrices with four perturbed corners," *The Australian & New Zealand Industrial and Applied Mathematics (Anziam) Journal*, vol. 49, no. 3, pp. 361–388, 2008.

[105] H. Hao and P. Barooah, "Asymmetric control achieves size-independent stability margin in 1-d flocks," in *Proceedings of the 50th IEEE conference on Decision and Control*, 2011.

[106] G. Hu, "Robust consensus tracking for an integrator-type multi-agent system with disturbances and unmodelled dynamics," *International Journal of Control*, vol. 84, no. 1, pp. 1–8, 2011.

[107] ——, "Robust consensus tracking of a class of second-order multi-agent dynamic systems," *Systems & Control Letters*, vol. 61, no. 1, pp. 134–142, 2012.

BIOGRAPHICAL SKETCH

He Hao was born in March, 1984 in Haicheng, China. He received his Bachelor of Science degree in mechanical engineering and automation in 2006 from Northeastern University, Shenyang, China, and a master's degree in mechanical engineering in 2008 from Zhejiang University, Hangzhou, China. He then joined the Distributed Control Systems Laboratory at the University of Florida to pursue his doctoral degree under the advisement of Dr. Prabir Barooah.